`

Single-cell and spatial multi-omics identify innate and stromal modules targeted by anti-integrin therapy in ulcerative colitis

Running Title: anti-integrin therapy affects multiple subsets in UC

Elvira Mennillo[1], Yang Joon Kim[2], Iulia Rusu[1], Gyehyun Lee[1], Leah C. Dorman[2], Faviola Bernard-Vazquez[1], Jared L. Bain[1], Ravi Patel[1,3], Christopher Andersen[1,3], Arjun Rao[1,3], Stanley Tamaki[3], Jessica Tsui[1,3,4], Alan Shen[1,3,4], Mohammad Naser[5], Walter Eckalbar[3], Soo-jin Cho[4], Kendall Beck[1], Najwa El-Nachef[1], Sara Lewin[1], Daniel R Selvig[1], Jonathan P Terdiman[1], Uma Mahadevan[1], David Y. Oh[1,6], Gabriela K. Fragiadakis[1,3], Angela Pisco[2], Alexis J. Combes[1,3,4], Michael G. Kattah[1#]

1. Department of Medicine, University of California San Francisco, San Francisco, CA, USA
2. Chan Zuckerberg Biohub, San Francisco, CA, USA
3. CoLabs, University of California, San Francisco, CA, USA
4. Department of Pathology, University of California, San Francisco, San Francisco, CA 94143, USA
5. Biological Imaging Development CoLab, University of California San Francisco, San Francisco, CA, USA
6. Division of Hematology/Oncology, Department of Medicine, University of California, San Francisco, San Francisco, CA, USA

To whom correspondence should be addressed:

Michael G. Kattah, 513 Parnassus Ave, S-357G Medical Science Building, San Francisco, CA 94143-0451.

Phone: 415-502-5717 Email: michael.kattah@ucsf.edu

ABSTRACT

Ulcerative colitis (UC) is an inflammatory intestinal disorder driven by mucosal immune and stromal subsets, culminating in epithelial injury. Vedolizumab (VDZ) is an anti-integrin monoclonal antibody that is effective for treating UC. VDZ is thought to primarily inhibit lymphocyte trafficking to the intestine, but its effect on other cell subsets is less well characterized. To identify the inflammatory cells that contribute to colitis and respond to VDZ, we performed a single-cell transcriptomic and proteomic analysis of peripheral blood and colonic biopsies in healthy controls (HC) and patients with UC on either aminosalicylates or VDZ. We identified mononuclear phagocytes (MNPs) as a primary target of VDZ, with comparatively modest effects on lymphocytes. Spatial proteomics and transcriptomics demonstrated increased density and proximity of MNP and fibroblast subsets in UC biopsies when compared to HC, with inhibition by VDZ. VDZ non-responders were enriched for activated fibroblast and MNP signatures in a validation cohort.

INTRODUCTION

Ulcerative colitis (UC) is a chronic inflammatory disorder of the intestine characterized by abnormal immune, stromal, and epithelial responses to microbial stimuli in genetically susceptible individuals, culminating in mucosal inflammation and epithelial injury. Vedolizumab (VDZ) is a monoclonal antibody against $\alpha_4\beta_7$ integrin that prevents binding to gut endothelial mucosal addressin-cell adhesion molecule 1(MAdCAM-1), blocking the trafficking of leukocytes to the intestine. The cellular and genetic factors that mediate VDZ response and non-response are incompletely characterized[1–3]. There are conflicting data regarding which inflammatory intestinal cell subsets are the most affected[4]. Many studies emphasize the effects of VDZ on B and T lymphocytes and regulatory T cells (Tregs)[3–8], while others suggest an impact on innate immune myeloid populations[9,10]. Understanding the cellular targets of VDZ is critical to stratify patients as potential responders or non-responders prior to treatment, and for identifying alternative treatment strategies for non-responders.

Tissue multi-omics studies in inflammatory bowel disease (IBD) have revealed important roles for stromal, epithelial, and immune compartments in driving disease and mediating treatment response and non-response[11–16]. To generate an unbiased, global assessment of the effects of colitis and the mechanism of action of VDZ, we performed a comprehensive single-cell multi-omics analysis that included single-cell RNA sequencing (scRNA-seq), cellular indexing of transcriptomes and epitopes by sequencing (CITE-seq, a modality that includes single-cell RNAseq in addition to an extensive antibody-based proteomic panel), and mass cytometry (CyTOF) of peripheral leukocytes and colonic biopsies in healthy controls (HC) and patients with UC on aminosalicylates (UC) or VDZ (UC-VDZ). To further investigate the spatial heterogeneity and proximity of intestinal tissue subsets, we performed multiplex ion beam imaging (MIBI), co-detection by indexing (CODEX), and highly multiplexed RNA *in situ hybridization* (RNA-ISH) on formalin-fixed, paraffin-embedded (FFPE) colonic biopsies, with both unsupervised and supervised analytic methods.

RESULTS

scRNA-seq of cryopreserved intestinal biopsies has high fidelity to fresh processing

To characterize the effects of VDZ in the peripheral blood and colon of UC patients, we employed a cross-sectional, case-control study design consisting of healthy controls without IBD (HC, n=4), patients with UC on

5-aminosalicylates (5-ASA) (UC, n=4), and patients with UC on VDZ (UC-VDZ, n=4) (**Fig. 1a, Supplementary Table 1**). To improve internal validity and cross-validate multi-omics signatures in a small number of patients, we analyzed the same patient samples using a variety of single-cell and spatial transcriptomic and proteomic methods, including scRNA-seq[17], CITE-seq[18], cytometry by time of flight (CyTOF)[19], multiplex RNA-ISH[20], MIBI[21], and CODEX[22] (**Fig. 1a, Supplementary Table 2**). Recent methods for cryopreserving undigested, intact intestinal mucosal biopsies revolutionized multi-omics pipelines because this approach streamlines sample collection and allows for banking and subsequent batch processing[15,23,24]. Batch processing of samples for scRNA-seq reduces cost and facilitates inter-sample comparison by removing batch effects[17]. To compare the performance of cryopreserved and non-frozen intestinal biopsies in scRNA-seq, we compared scRNA-seq of biopsies from two donors that were frozen briefly in cryopreservation media (Cryopreserved) to samples that were stored briefly on ice (Fresh) (**Fig. 1b**). Fresh and Cryopreserved colon biopsies yielded similar cell distribution in uniform manifold approximation and projection (UMAP) (**Fig. 1c**), with the expected coarse cell clusters (**Fig. 1d**), and no statistically significant differences in immune, epithelial, and stromal cell subset frequencies (**Fig. 1e**). scRNA-seq pseudobulk analysis of differentially expressed (DE) genes identified up-regulation of heat-shock proteins (*HSPA1A, HSPA1B, HSPE1,* and *HSPD1*) in Fresh biopsies, likely due to storage at 4°C prior to warming to 37°C[25], as well as up-regulation of *FOSB* in Cryopreserved biopsies (**Fig. 1f**). The high degree of concordance between freshly processed and cryopreserved intestinal biopsies, combined with the logistic, financial, and batch processing benefits of cryopreserved biopsies, favors cryopreservation.

VDZ is associated with modest transcriptional changes in peripheral leukocyte subsets

We hypothesized that patients on VDZ would exhibit increased circulating inflammatory lymphocytes due to inhibition of intestinal trafficking. To test this, we performed scRNA-seq on peripheral blood leukocytes (PBLs) from HC, UC, and UC-VDZ patients (**Fig. 2a**). Cryopreserved PBLs were thawed, pooled, run in a single batch, and deconvoluted with freemuxlet/demuxlet[17], minimizing batch effects. The anticipated coarse (**Extended Data Fig. 1a**) and fine leukocyte subsets (**Fig. 2b**) were identified based on landmark genes expressed for each cluster (**Extended Data Fig. 1b-e**), in agreement with previously described gene sets[26,27]. Granulocytes were not observed, likely due to poor viability after freezing and thawing. Cells from each

patient were mostly distributed across coarse and fine clusters (**Fig. 2c**), as well as disease and treatment status (**Fig. 2d**), suggesting minimal batch-effect. HS12 had an expanded circulating cytotoxic lymphocyte population, but this was not observed in the other UC-VDZ patients (**Fig. 2b,c).** When we compared the cell frequency for each fine leukocyte cell subset across conditions, we did not observe any statistically significant differences among patients (**Fig. 2d,e**). scRNA-seq pseudobulk analysis revealed up-regulation of *IFITM3* in UC patients compared to HC, and down-regulation of *IFITM2* in UC-VDZ patients compared to UC patients (**Fig. 2f**). DE gene analysis of individual leukocyte subsets identified a small number of differences in lymphocyte and monocyte subsets (**Fig 2g, Extended Data Fig. 2a,b**). Notable changes were up-regulation of *ERAP2* and *IFITM2* in MAIT cells, *GZMH* in CD8 and γδ T cells, and *CD52* in $CD14^+$ monocytes in UC as compared to HC (**Extended Data Fig. 2a**)**.** VDZ was associated with reductions in *GZMK, GZMM,* and *DUSP2*, and an increase in *ITGB1* in CD8 T cells, which is consistent with a therapeutic reduction in CD8 cytotoxicity and tissue trafficking (**Extended Data Fig. 2b**). VDZ was also associated with significant increases in *TMEM176A* and *TMEM176B* in $CD14^+$ monocytes of UC-VDZ patients (**Extended Data Fig. 2b**). *TMEM176B* has been suggested to inhibit the inflammasome and dendritic cell maturation[28–30]. To further identify pathways that were potentially pathogenic in UC, and targeted or reversed by VDZ, we then filtered for DE genes that were up-regulated in UC vs HC, and reciprocally down-regulated in UC-VDZ vs UC, and vice versa (**Fig. 2h**). This analysis highlighted up-regulation of *CCL4L2* in CD8 T cells, as well as up-regulation of *CD52 and HLA-DQB1* in $CD14^+$ monocytes in UC as compared to HC, all with reciprocal down-regulation in UC-VDZ patients**.** Although scRNA-seq identified some global and cell subset specific transcriptomic associations with UC and VDZ therapy, in general circulating leukocyte subset frequencies were relatively stable with modest transcriptional differences.

Tissue CITE-seq identify effects of VDZ on immune and non-immune subsets

To examine the tissue effects associated with UC and VDZ therapy, we performed CITE-seq on colonic mucosal biopsies from the same patients (**Fig. 3a, Supplementary Table 2**). Cryopreserved biopsies were thawed, digested, pooled, run in a single batch, and deconvoluted with freemuxlet/demuxlet[17], minimizing batch effects. The anticipated coarse (**Extended Data Fig. 3a**) and fine colonic mucosal subsets (**Fig. 3b**) were identified using landmark genes associated with each cluster (**Extended Data Fig. 3b** and **Extended**

Data Fig. 4,5). The subsets identified using cryopreserved biopsies were similar to those previously described for fresh biopsies[11,12,14,31]. The CITE-seq panel provided a human intestinal cell surface proteome in HC, UC, and UC-VDZ patients, and highlighted for example CD103 (αE integrin) expression by CD8 tissue resident memory T cells (Trm) (**Fig. 3c**, **Extended Data Fig. 4h**). Sets of surface proteins associated with each intestinal cell subset were identified by CITE-seq (**Extended Data Fig. 3-5**). Cells from each patient were distributed across intestinal cell clusters (**Fig. 3d**). Biopsies were categorized as HC (gray), mild-to-moderate endoscopic disease activity (UC 0-1, purple), or moderate-to-severe endoscopic disease activity (UC 2-3, orange), or as coming from HC (gray), UC (blue), or UC-VDZ (red) patients (**Fig 3e-h, Extended data Fig 6**). After correcting for multiple comparisons, there were significant increases in Tregs, activated and S2 fibroblasts, and endothelial cell subsets, with reductions in innate lymphoid cells (ILCs), IgM-secreting plasma cells, S1 fibroblasts, activated and memory $CD4^+$ T cells, and CD8 Trms in more severely inflamed segments (**Fig. 3g**, **Extended Data Fig. 6a,b**). The relative frequencies of activated and memory $CD4^+$ and $CD8^+$ T lymphocyte subsets vary among studies depending on inflammatory status and disease activity[14,32], but increases in Tregs have been consistently reported[33–37]. Reductions in ILC3s[38], and a shift from IgM/IgA to IgG-secreting plasma cells[14,31] have been previously described in IBD scRNA-seq. The relative increase in goblet cells we observed was likely due to low goblet cell counts, and a relative reduction in absorptive colonocytes and intestinal stem cells (ISCs) (**Extended Data Fig. 6a,b**). We observed a global expansion of both venous and arterial endothelial cells in more severely inflamed UC biopsies (**Fig. 3g, Extended Data Fig. 6a,b**). Stromal cell subsets in IBD have been previously described[11], and here CITE-seq highlighted a significant shift from S1/3/4 stromal fibroblasts to increased S2 and activated fibroblasts in more severely inflamed UC biopsies. The activated fibroblasts in our dataset expressed high levels of *TIMP1, MMP1, MMP3, AREG, TMEM158, TNFRSF11B* and surface CD10, while the S2 fibroblasts expressed high levels of *F3*, *POSTN, CXCL14, ENHO, PDGRFA, SOX6*, and surface CD10, CD146, and CD49a (**Extended Data Fig. 5c,d**), sharing some features with the *IL13RA2*$^+$*IL11*$^+$*TNFRSF11B*$^+$ inflammatory fibroblasts associated with anti-TNF resistance[14]. Interestingly, VDZ was not associated with significant reductions in lymphocyte subsets compared to UC biopsies. However, VDZ was associated with a statistically significant reduction in myeloid dendritic cells (mDCs), which were high in *CD1C* gene expression, as well as surface CD1c, CD11c, and FcεR1α (**Fig. 3h**, **Extended Data Fig. 4j**). VDZ also correlated with trends toward fewer activated

fibroblasts, inflammatory macrophages, and mast cells (**Fig 3h, Extended Data Fig. 6d**). In the epithelial compartment, VDZ was associated with a statistically significant increase in epithelial cells generally, with a trend toward fewer deep crypt secretory (DCS) cells (**Fig. 3h**), consistent with mucosal healing. Although VDZ did not appear to significantly alter lymphocyte populations in colonic biopsies by CITE-seq, subsets of inflammatory MNPs and stromal cells were lower in UC-VDZ patients, with a concomitant expansion of undifferentiated epithelial cells.

Analysis of gene expression in tissue CITE-seq revealed significant transcriptomic changes associated with HC, UC, and UC-VDZ patients. scRNA-seq pseudobulk analysis revealed an increase of *TIMP1* and *CD74* in UC as compared to UC-VDZ, and UC-VDZ samples were associated with increased *CCL4* and *CCL5* (**Extended Data Fig. 7a**). Both *TIMP1* and *CD74* were increased in a meta-analysis of UC colonic biopsy bulk gene-expression[39], and both were expressed at high levels in endothelial, stromal, and MNP subsets in our dataset. CCL4 and CCL5 bind CCR5 and promote intestinal trafficking and inflammation in murine colitis models, suggesting a potential compensatory mechanism for intestinal trafficking in UC-VDZ[40]. More DE genes were observed in biopsy cell subsets compared to peripheral blood (**Fig 2g, Extended Data Fig. 2a,b**). Stromal fibroblasts and endothelial cells exhibited the highest number of DE genes among the study subjects, as well as MNPs, mast cells, and cycling cells (**Extended Data Fig. 7b**). Although VDZ is frequently discussed in terms of its effect on lymphocyte trafficking, non-lymphoid subsets generally exhibited more dynamic DE genes than lymphocyte subsets (**Extended Data Fig. 7c,d**). MNPs from UC patients expressed higher levels of *TIMP1*, *SOD2*, and *TYMP*, *C15orf48,* and *CD63*, compared to HC, all of which were reciprocally decreased in UC-VDZ patients (**Extended Data Fig. 7c,d**). Mast cells expressed multiple inflammatory genes at higher levels in UC-derived as compared to HC-derived biopsies, but VDZ did not appear to antagonize these signatures (**Extended Data Fig. 7c,d**). Stromal fibroblasts in UC patients expressed higher levels of *MMP3, TIMP1, TMEM158*, *COL6A3,* all of which were previously reported to be increased in bulk UC biopsies[39] (**Extended Data Fig. 5c; Extended Data Fig. 7c**). This activated signature was reciprocally downregulated by VDZ (**Extended Data Fig. 7c,d**). Endothelial cells expressed significantly higher levels of *TIMP1*, *MGP, S100A6*, *TPM4, TM4SF1, CD59, PRKCDBP*, and lower levels of *TXNIP* and *FABP5* in UC vs HC samples (**Extended Data Fig. 7c,d**). These endothelial cell DE genes were consistent

with trends observed in bulk UC biopsies[39], and all were reversed by VDZ (**Extended Data Fig. 7c,d**). Finally, epithelial cells from UC patients expressed higher levels of *LCN2* and lower *FABP1*, correlating with a relative reduction of absorptive colonocytes in UC compared to HC and reversed by VDZ, consistent with recovery of absorptive colonocytes (**Extended Data Fig. 5s and 7c**). Taken together, DE gene analysis identified relatively few transcriptional differences in lymphocyte subsets among HC, UC, and UC-VDZ patients, with more dynamic transcriptional changes in MNPs, stromal fibroblasts, and endothelial cells. The colonic mucosal biopsy CITE-seq data suggests a model where VDZ significantly inhibits intestinal MNP trafficking and differentiation, indicating a reduced activation of inflammatory fibroblasts and endothelial cells, with recovery of intestinal epithelial cells.

Unsupervised and supervised CyTOF analysis confirms effects of VDZ on multiple epithelial and innate immune subsets

To further explore the effects of VDZ on different cell populations, and to validate scRNA-seq and CITE-seq data with an orthogonal multi-omics technique, we performed CyTOF on paired PBLs and colon biopsies collected and processed in parallel from HC, UC and UC-VDZ patients (**Fig. 4a, Supplementary Table 2**). This complementary multi-omic assay was performed on the same starting cell preparations as CITE-seq, with the exception that CyTOF biopsy samples did not undergo Annexin-V-based dead cell depletion, and right (R) and left (L) colon biopsies were combined for each patient to yield more cells. We performed an initial unsupervised analysis for unsupervised UMAP calculation, clustering, and visualization. Based on marker intensity we annotated 21 unsupervised clusters in PBLs and colon biopsies, and then combined clusters with highly similar phenotypes (**Fig 4b, Extended Data Fig. 8**). For unsupervised analysis of PBL CyTOF data, UMAP stratified by condition showed a homogenous distribution among the three different groups and all patients were represented in each cell cluster (**Extended Data Fig. 8c,d**). Granulocytes were identified in PBLs by CyTOF, representing less than 2% of the total cells after freezing and thawing. After adjusting for multiple comparisons, there were no statistically significant alterations in circulating PBL subsets among HC, UC, and UC-VDZ patients by unsupervised CyTOF analysis (**Extended Data Fig. 8e).** In the unsupervised analysis of colon biopsy CyTOF data, patient samples were distributed across cell clusters (**Extended Data Fig. 8g**), with some clusters enriched for HC, UC, or UC-VDZ derived cells (**Fig 4c**). The

percent of epithelial cells was higher in CyTOF than CITE-seq. Multiple epithelial subsets emerged from the unsupervised clustering, including epithelial clusters 2/3_EpCAM$^+$CD15^{hi}, 5/6/8_EpCAM$^+$ICOS^{hi}, and 9/12_EpCAM$^+$HLA-DR$^+$ (**Fig. 4 d-f,** and **Extended Data Fig. 8i**), in addition to the expected non-epithelial clusters. Unsupervised clusters were analyzed for changes among HC, UC, and UC-VDZ patients. Cross-referencing complementary CITE-seq data suggested CD15^{hi} epithelial cells are enriched in secretory and transit amplifying epithelial subsets (**Extended Data Fig. 5b**). CD15^{hi} epithelial cells were significantly reduced in UC compared to HC and increased in UC-VDZ biopsies in the unsupervised analysis (**Fig 4d**). ICOS^{hi} epithelial cells were also a distinct cluster of IECs in the unsupervised analysis (**Fig 4b,e**), but no consistent trend in ICOS^{hi} IECs was observed by CITE-seq or downstream supervised CyTOF analysis. EpCAM$^+$HLA-DR$^+$ were increased in both UC and UC-VDZ as compared to HC, although these trends were not statistically significant after correcting for multiple comparisons (**Fig. 4f**). Increased expression of HLA-DR on IECs in IBD patients has been previously described and has been demonstrated in IEC-T cell co-culture experiments that HLA-DR significantly mediates the interaction of IECs with CD4$^+$ T cells [41,42]. In the non-epithelial compartments, cluster 18 consisted of mDCs and macrophages, and 20/21 containing plasma cells were both increased in UC patients as compared to HC and reduced in UC-VDZ compared UC patients (**Fig. 4g,h**). In summary, unsupervised CyTOF analysis did not identify any significant alterations in PBLs, but a surprising reduction of CD15^{hi} secretory IECs in UC, which was reversed in UC-VDZ patients. The trend of increased tissue MNP populations in UC as compared to HC, and reduction by VDZ, noted in CITE-seq was corroborated by unsupervised CyTOF analysis.

Following unsupervised clustering and analysis, we then performed a supervised gating strategy including the unique epithelial subsets identified by the unsupervised analysis (**Extended Data 9, 10**). Supervised analysis did not reveal any statistically significant changes in circulating PBLs by CyTOF (**Extended Data Fig. 10a**). Supervised analysis of biopsy CyTOF data confirmed a statistically significant increase in HLA-DR$^+$ IECs in UC and UC-VDZ samples compared to HC, and a trend toward reduced CD15^{hi} IECs in UC with re-expansion by VDZ (**Fig. 4i-k**). IECs were also broadly expanded in UC-VDZ compared to UC, consistent with CITE-seq data (**Fig. 3h)**. In agreement with the unsupervised CyTOF analysis and CITE-seq data, MNP subsets exhibited a trend toward reduction in UC-VDZ patients, including mDCs (cDC1, cDC2, cDC2b), classical

monocytes, and macrophages (**Fig. 4l-n, Extended Data Fig. 10b**). We observed minimal effects on the frequencies of lymphocyte subsets in biopsies of UC-VDZ patients by supervised analysis of biopsy CyTOF data (**Extended Data Fig. 10b**). Since VDZ selectively binds to the integrin $\alpha_4\beta_7$, blocking its interaction with MAdCAM-1, we then looked at the ratio of $\alpha_4\beta_7^+$ cells in the biopsies relative to the blood for each subset, and found that VDZ significantly decreased $\alpha_4\beta_7^+$ cells in colon biopsies in the majority (16 of 22) cell subsets (**Fig 4o-q, Extended Data Fig. 10c**). This pattern was prominent in a hierarchically clustered heatmap, showing unsupervised clustering of UC-VDZ patients HS9-12 based on a lower abundance for all the defined $\alpha_4\beta_7^+$ cell populations in biopsies relative to blood (**Fig. 4o**). Therefore, VDZ does broadly interfere to some extent with intestinal trafficking for many cell types, even if absolute frequencies of MNP subsets were more significantly affected than lymphocyte subsets. To understand this process further, we evaluated the percent of each $\alpha_4\beta_7^+$ subset in the peripheral blood and tissue samples (**Fig.4 p,q**). Overall, $\alpha_4\beta_7^+$ dendritic cells (cDC1, cDC2, and cDC2b) were among the most significantly increased in the circulation of UC-VDZ patients, with >20% of the DCs in circulation expressing $\alpha_4\beta_7$ (**Fig 4p**). This corresponded to a significant reduction in $\alpha_4\beta_7^+$ cDC1 cells in UC-VDZ patient biopsies compared to HC, consistent with significant inhibition of intestinal trafficking by VDZ for these cells (**Fig. 4q**). $\alpha_4\beta_7^+$ CD8 T central memory (CD8+ T_{CM}) were reduced in UC-VDZ biopsies as compared to HC and UC patient biopsies (**Fig 4q**), but there was no overall reduction in the frequency of CD4 or CD8 T cell subsets in UC-VDZ patient biopsies (**Extended Data Fig 10b**). This together with the trend observed on macrophages suggest that VDZ significantly affects the MNP compartment, in particular $\alpha_4\beta_7^+$ mDCs, with secondary effects on multiple IEC subsets.

Spatial proximity of MNP and fibroblast subsets vary by disease and VDZ treatment

We used a variety of spatial transcriptomic and proteomic methods with single-cell resolution to evaluate the colonic tissue micro-environment across disease and treatment status in FFPE samples[43–45]. 12-plex RNA-ISH exhibited adequate sensitivity and specificity for some high-expressing cell lineage markers, but we could not measure low-expressing genes, including *ITGA4, ITGB7*, *MADCAM1,* and *FLT3* (**Extended Data Fig 11a,b, Supplementary Table 3**). 39-plex MIBI on the same tissue microarray (TMA) identified 20 phenotypes with high signal-to-noise ratio (SNR), but the need to balance resolution and field-of-view (FOV) with longer acquisition times ultimately yielded fewer cells than RNA-ISH (**Fig. 5a-d, Supplementary Table 3)**. Despite

limited cell counts with MIBI, tissue MNPs and fibroblasts were associated with a trend toward reduction in UC-VDZ compared to UC (**Fig. 5d; Extended Data Fig. 11c**). We then performed 28-plex CODEX and unsupervised clustering, visualization, and annotation, mirroring the CyTOF analysis (**Fig. 5e**; **Extended Data Fig. 11d**; **Supplementary Tables 3,4**). Unsupervised analysis generated 24 clusters, and highly similar clusters were subsequently grouped to yield 11 clusters (**Fig. 5f**). Pearson correlation heatmap showed positive and negative correlation among different markers (**Fig. 5g**). The UMAP, Pearson correlation and heatmap, along with visual inspection of each channel, identified specific and nonspecific markers for the supervised cell phenotype analysis of 18 subsets (**Fig. 5h**; **Extended Data Fig. 11d, Supplementary Table 4**). After correcting for multiple comparisons, memory $CD8^+$ T cells were increased in UC compared to HC and decreased in UC-VDZ (**Extended Data Fig. 11e**). CD68+ epithelial cells identified in unsupervised analysis of CODEX correlated with a subset of absorptive colonocytes in CITE-seq, although these were not significantly altered by disease or treatment status (**Extend Data Fig 11f).** Although the CODEX panel was not specific enough to quantitate mDCs, we could reliably detect and quantify macrophages, which were increased in UC compared to HC and reduced in UC-VDZ patients, although this was not statistically significant after correcting multiple comparisons (**Fig. 5i**). Correlating surface marker expression between CODEX and tissue CITE-seq in the stromal compartment, were further annotated as $CD44^+$ and $PDPN^+$ activated/inflammatory fibroblasts. $CD44^+$ activated fibroblasts showed a trend toward increase in UC and reduction by VDZ (**Fig. 5j**), similar to CITE-seq. Intestinal fibroblasts elicit essential functions in maintaining organ integrity and regulating structural fitness and repair[46], and it has been reported in transcriptomic studies their association with MNPs during inflammation in IBD[14,46,47]. MNPs and fibroblasts exhibited reduced distance in UC compared to HC and UC-VDZ by nearest neighbor (NN) analysis of MIBI images (**Fig. 6a)**. NN analysis of CODEX images confirmed proximity of macrophages and activated fibroblasts in UC compared to HC and UC-VDZ patients (**Fig. 6b).** Collectively, these observations were consistent with CITE-seq data showing an effect of VDZ on trafficking and abundance of tissue MNP subsets and their interaction with activated fibroblasts.

To further evaluate the colonic tissue microenvironment in health and disease, we then performed 960-plex RNA-ISH (CosMx from Nanostring) on our FFPE TMA at subcellular resolution, as recently described (**Fig.**

6c)[48]. After, cell segmentation and mapping of transcript location (**Fig. 6d**), the resulting gene expression matrix was processed as if it were single-cell gene expression data. Cells with low <10 unique genes or <50 transcripts per cell were excluded, and negative control probes confirmed low non-specific transcript detection (**Extended Data Fig 11g,h**). A UMAP plot clustering cells with similar gene expression profiles (**Fig 6e**) and corresponding spatial scatter plots (**Fig 6f**) were used to manually annotate cell types. Landmark genes for each subset correlated well with CITE-seq (**Extended Data Fig. 11i**). Activated fibroblasts (*TIMP1, IL1R1, CXCL14*, *CD44*) and activated inflammatory MNPs (*S100A4, TIMP1, S100A9, CD80, ITGAX, LYZ, IL1B*), which contained a mixture of inflammatory macrophages and mDCs were more likely to be in spatial proximity in UC biopsies as compared to HC, but not in UC-VDZ patients (**Fig. 6g,h**). 960-plex RNA-ISH supported a model where inflammatory MNP subsets and inflammatory fibroblasts were increased in density and proximity in actively inflamed colonic tissue, and this module was inhibited by VDZ.

Activated MNP, fibroblast, and endothelial signatures are associated with VDZ non-response

To determine if our model of MNP inhibition by VDZ was supported by other datasets, and to assess if this mechanism of action was associated with treatment response and non-response, we performed gene set enrichment analysis (GSEA)[49,50] of a longitudinal, publicly available, bulk transcriptomic dataset of UC patients using landmark genes for subsets that varied by disease and treatment status in our multi-omics analysis (**Supplementary Table 5**). Neutrophils were not present in our biopsy CITE-seq data, but a gene set signature was generated from canonical landmark genes. Neutrophils, cytotoxic lymphocyte (containing primarily CD8 T- and NK-specific genes), B, CD4 T, and plasma cell gene signatures were also included to compare with MNP and stromal signatures. Not surprisingly, VDZ responders (n=9) exhibited broad reduction in immune and activated stromal Net Enrichment Scores (NES), with an expansion of epithelial gene set enrichment, consistent with reduced inflammation and mucosal healing (**Fig. 6i**). In contrast, VDZ non-responders (n=5) exhibited a high initial pre-treatment cytotoxic lymphocyte signature, persistent activated and S2 fibroblast gene signatures post-treatment, without significant epithelial enrichment post-treatment, consistent with a model where high initial cytotoxic lymphocyte injury and persistent stromal tissue inflammation prevents mucosal healing (**Fig. 6i**). Interestingly, the reduction in immune subsets in VDZ non-responders was smaller and not statistically significant compared to VDZ responders, which could explain the

persistent activate stromal signature and reduced epithelial healing. VDZ non-responders (n=9) could be differentiated from responders (n=11) by pre-treatment enrichment for endothelial, activated fibroblast, neutrophil, macrophage, and monocyte signatures (**Fig. 6j**). Gene signatures investigated were clearly distinguished by leading edge analysis (**Fig. 6k**). These data suggest that VDZ non-responders have higher pre-treatment tissue innate immune and activated stromal subset inflammation, and that these cell subsets likely drive inflammatory cell trafficking via $\alpha_4\beta_7$-independent pathways.

DISCUSSION

To identify and validate the transcriptomic, proteomic, and cellular signatures associated with UC and VDZ treatment, we optimized a multi-omics pipeline that involves batch processing of cryopreserved biopsies for simultaneous multiplexed CITE-seq and CyTOF, coupled with spatial analysis of FFPE biopsies. VDZ was associated with small effects in peripheral leukocytes, while colonic tissue profiling demonstrated a significant reduction in MNPs, expansion of epithelial subsets, and a trend toward fewer activated fibroblasts by CITE-seq. Among immune subsets analyzed by CyTOF, mDCs exhibited the highest shift of $\alpha_4\beta_7^+$ cells from the tissue to the peripheral blood. Spatial proteomics and transcriptomics of FFPE colonic biopsies using MIBI, CODEX, and highly multiplexed RNA-ISH demonstrated increased density and proximity of MNP and fibroblast subsets in UC as compared to HC, with inhibition by VDZ. Using longitudinal, publicly available transcriptomic data, VDZ responders were characterized by a reduction in tissue MNP and other immune gene signatures over time, along with reduced stromal inflammatory gene signatures and epithelial healing. In contrast, VDZ non-responders exhibited persistent stromal activation over time, and relatively increased activated stromal, endothelial, MNP, and neutrophil activation signatures at baseline.

There are conflicting data regarding the primary mechanism of action of VDZ. VDZ has been reported to bind to CD4 T, CD8 T, B, NK, and granulocytes in the peripheral blood[51,52]. Here we confirm that VDZ shifts $\alpha_4\beta_7^+$ cells from the colon to the circulation for most cell types, but this results in a small net change in tissue cell frequency for most cell subsets, apart from MNPs. Multiple studies have investigated the effect of VDZ on T cell subsets, in general supporting models where pathogenic effector T cell subsets are excluded more efficiently than regulatory T cell subsets[6–8,53]. Our data do not exclude any of these observations, but rather add that a primary mechanism of action for VDZ is binding and inhibition of intestinal MNP trafficking, which

reduces tissue inflammation. One recent study demonstrated that VDZ did not consistently alter the phenotype, activation, or repertoire of lamina propria T cells by flow cytometry and TCR sequencing, but bulk transcriptomic data was consistent with a shift in MNP gene signatures[10]. The impact of VDZ on intestinal MNP populations likely affects the recruitment and activation of adaptive immune subsets.

This study has important therapeutic implications. Our CyTOF analysis demonstrates that mDCs are highly dependent on $\alpha_4\beta_7$ for intestinal trafficking, consistent with MAdCAM-1-deficient and β7 integrin-deficient mice[9]. Our data suggest that T cells are better able to exploit $\alpha_4\beta_7$-independent intestinal trafficking pathways than mDCs. These pathways could include $\alpha_4\beta_1$:VCAM1, GPR15:C10ORF99, or CCR6:CCL20[54]. Interestingly, *GPR15* and *CCR6* are expressed by lymphocytes, but not mDCs or monocytes, which could partially explain the greater impact of VDZ on tissue MNPs. Since MNPs are targeted by VDZ, refractory patients may benefit from additional combination therapies that target lymphocytes or activated stromal cell subsets, as is done sometimes in clinical practice for refractory IBD patients[55]. Recently, inflammatory fibroblasts have been reported to secrete neutrophil-tropic CXCR1 and CXCR2 ligands in response to IL-1β[47]. Our study was not optimized to analyze neutrophils, but we do show that VDZ non-responders exhibit increased activated fibroblast signatures at baseline and after therapy. The observation that inflammatory MNPs and fibroblasts share similar cellular neighborhoods further supports a rationale for IL-1β neutralization in refractory colitis.

A secondary objective of this study was to evaluate various multi-omics platforms on cryopreserved biopsies and FFPE tissue. CyTOF quantitated the most cells per patient, MIBI the fewest, while CITE-seq, CODEX, and RNA-ISH methods yielded comparable numbers of cells per patient (**Extended Data Fig 12a**). Comparing across tissue compartments, CITE-seq over-sampled the immune compartment and under-sampled the epithelial compartment when compared to other multi-omics methods (**Extended Data Fig 12b, Supplementary Table 6**). Given the ubiquity of FFPE tissue, preservation of spatial relationships, and more accurate representation of *in situ* cell frequencies and gene expression, FFPE-compatible spatial multi-omic technologies provide a powerful complementary method for analyzing patient-derived biospecimens.

There are several limitations of this study, including a small sample size and case-control approach for the primary analysis. We chose to perform in-depth multi-omic analysis in the same patients to maximize phenotypic data from each patient, followed by validation in bulk transcriptomic data from a longitudinal cohort of patients before and after VDZ therapy. In the future, longitudinal single-cell and spatial multi-omic data from more patients could permit intra-individual normalization and detect more subtle changes in differential gene and protein expression. Another limitation of this study is that we focused exclusively on host factors, but microbial determinants and metabolomics have also been shown to contribute to therapeutic response in IBD[56,57]. Incorporating additional multi-omic modalities in future studies could enhance our understanding of treatment response and non-response in UC.

In summary, we performed comprehensive single-cell and spatial tissue transcriptomic and proteomic phenotyping to establish MNPs as a key target of anti-integrin therapy in UC, with associated changes in stromal and epithelial populations. This study highlights important cellular networks involving MNPs and fibroblasts in colitis. Building on innovative work that first described cryopreserved mucosal biopsies for multi-omics analysis[15,16], we showed here that cryopreserved biopsy scRNA-seq has high fidelity to fresh samples, which significantly reduces cost, facilitates inter-sample comparison, and minimizes batch effects. The combination of CITE-seq and CyTOF on the same sets of biopsies establishes a surface protein cell atlas for the colon in health, disease, and during treatment. We also describe a spatial atlas for colitis with single-cell resolution using MIBI, CODEX, and highly multiplexed RNA-ISH on FFPE samples, allowing comprehensive cell subset quantitation, differential expression, and proximity analysis. Ultimately, precision medicine implies approaching each patient as an n-of-1, and here we show that multiple orthogonal multi-omics analyses enhance internal validity for immunophenotyping, even with small sample sizes. Implementing single-cell and spatial multi-omics methods simultaneously in individual patients will provide deep immunophenotyping and lead to more precise treatment algorithms.

METHODS

Study approval

The study was conducted according to Declaration of Helsinki principles and was approved by the Institutional Review Board of the University of California, San Francisco (19-27302). Written informed consent was received from participants prior to inclusion in the study.

Study participants and biospecimen collection

Patients undergoing colonoscopy or sigmoidoscopy for standard of care indications were screened for study eligibility. All patients gave written informed consent and approval. Peripheral blood and cold forceps biopsy samples were obtained from patients with UC, and individuals without IBD as “healthy controls” (HC). Baseline demographic and clinical data for the study participants are provided in **Supplementary Table 1**. Demographic options were defined by the investigators and participants chose their classifications. HC patients were patients without known or suspected IBD undergoing elective colonoscopy or sigmoidoscopy for various indications (e.g., colorectal cancer screening). Biopsy samples were categorized as coming from an area that was endoscopically noninflamed (score=0), mildly inflamed (score=1), moderately inflamed (score=2), or severely inflamed (score=3). Samples were assigned unique identifiers before biobanking.

Sample collection and storage

Colon biopsies were obtained with standard cold endoscopic biopsy forceps from two different regions of the colon (R=right/proximal and L=left/distal) with separate vials for different downstream applications. Two biopsies were collected in 10% formalin in 5 mL tubes for 24h, then washed with PBS twice and stored in 70% ethanol for paraffin embedding; two biopsies were collected in 4mL RNAlater in 5 mL tubes stored overnight at 4°C for, then solution was aspirated, and biopsies were stored at -70°C until further analysis. Six biopsies were collected in a conical tube with Basal Media (Advanced DMEM/F12 with NEAA and Sodium Pyruvate, Thermo cat. No. 12634-010; 2mM Glutamax, Thermo cat. No. 35050061; 10 mM HEPES (Corning); Penicillin-Streptomycin-Neomycin (PSN) Antibiotic Mixture, Thermo cat. No. 15640055; Normocin 100 µg/mL, Invivogen cat. No. ant-nr-2; 1 mM N-acetylcysteine, Sigma-Aldrich, A9165) with 10 µM Y-27632 (MedChem Express) at 4°C. Samples were immediately placed on ice and transported to the laboratory for processing as previously described[58]. Biopsies were transferred into cryovials containing freezing media (90% (v/v) FCS, 10% (v/v) DMSO and 10 µM Y-27632) and immediately placed into a freezing container (Mr. Frosty or Coolcell) and stored at -70°C for up to 4 weeks before transferring to liquid nitrogen cryostorage until further processing. A PAXgene RNA tube (Qiagen) for peripheral blood was collected, stored, and

processed according to the manufacturer's instruction. For peripheral blood leukocyte (PBL) isolation, peripheral blood was collected into EDTA tubes (BD, 366643). 2 mL aliquots of peripheral blood were treated with 30mL of RBC lysis buffer (Roche) for 5-8 minutes at room temperature with gentle mixing. Cells were re-suspended in CryoStor CS10 (at 4°C) freezing medium, aliquoted in cryovials, transferred to a freezing container (Mr. Frosty or Coolcell), and stored at -70°C for up to 4 weeks before transferring to liquid nitrogen cryostorage until further processing.

Preparation of colon and peripheral blood single-cell suspensions

Colon biopsies were thawed for 2min with gentle agitation in a 37°C water bath, transferred to a gentleMACS C Tube (Miltenyi Biotec), washed twice with basal media containing 10 μM Y-27632, and then incubated in 5 mL digestion buffer (basal media, 10 μM Y-27632, 600 U/mL Collagenase IV (Worthington cat. No. LS004189), 0.1 mg/mL DNAse I (Sigma-Aldrich, D4513)) and digested for 20 min at 37°C in a shaking incubator set at 225 rpm. Subsequently, samples were placed in the gentleMACS dissociator and run the gentleMACS program m_intestine_01 followed by 15 min incubation at 37°C in a shaking incubator set at 225 rpm. The suspension was then strained through a 100 μm strainer (Miltenyi) and centrifuged at 450g for 5 min at RT. Two additional washes were performed in Hanks' Balanced Salt Solution (HBSS) (Corning), containing 0.1 mg/mL DNAse I (Sigma-Aldrich, D4513). $1x10^6$ total cells were set aside for CyTOF. For the remaining cells, dead cells were removed with the Dead Cell Removal Kit (Miltenyi) according to the manufacturer's instructions. Cell suspensions were counted using a TC20 Automated Cell Counter (Bio-Rad) with 0.4% Trypan Blue Solution (Thermo Fisher Scientific). Live-cell enriched colon single-cell suspensions were used for CITE-seq, with a final pooled viability was >75%. PBLs were thawed for 2min with gentle agitation in a 37°C water bath and then washed twice with complete DMEM (Thermo Fisher) supplemented with nonessential amino acids (Thermo Fisher Scientific), sodium pyruvate (Thermo Fisher Scientific), HEPES (10 mM; Corning), Glutamax (2 mM; Thermo Fisher Scientific), Normocin (100 μg/mL; Invivogen, ant-nr-2), penicillin-streptomycin (Thermo Fisher Scientific) and 10% Fetal Bovine Serum (VWR). Cells were incubated with ACK lysis buffer (Quality Biological) for 5min at room-temperature, washed twice with complete DMEM, treated with HBSS (Corning) containing 0.1 mg/mL DNAse I (Sigma-Aldrich, D4513) for 5 min, and then strained through a 20um pre-separation filter (Miltenyi). Cells were counted using a TC20 Automated Cell Counter (Bio-Rad) with 0.4% Trypan Blue Solution (Thermo Fisher Scientific). Peripheral

blood leukocytes (PBLs) from each donor were used for scRNA-seq and CyTOF, with a final pooled viability of >85%.

Bulk RNA-seq sample and computational processing

RNA was extracted from blood or biopsies following manufacturer's protocol using PAXgene kit and Qiagen Rneasy Mini kit (Qiagen), respectively. RNA quality and integrity were measured with the Agilent RNA 6000 Nano Kit on the Agilent 2100 Bioanalyzer, according to manufacturer's instructions. Ribosomal and hemoglobin depleted total RNA-sequencing libraries were created using FastSelect (Qiagen cat#: 335377) and Tecan Universal Plus mRNA-Seq (0520-A01) with adaptations for automation of a Beckmen BioMek FXp system. Libraries were subsequently normalized and pooled for Illumina sequencing using a Labcyte Echo 525 system available at the Center for Advanced Technology at UCSF. The pooled libraries were sequenced on an Illumina NovaSeq S4 flow cell lane with paired end 150bp reads. Computation processing for genotyping was performed as previously described[27,59]. Briefly, sequencing reads were aligned to the human reference genome and Ensembl annotation (GRCh38 genome build, Ensembl annotation version 95) using STAR v2.7.5c (PMID: 23104886) with the following parameter— --outFilterType BySJout –outFilterMismatchNoverLmax 0.04 – outFilterMismatchNmax 999 –alignSJDBoverhangMin 1 –outFilterMultimapNmax 1 – alignIntronMin 20 –alignIntronMax 1000000 –alignMatesGapMax 1000000. Duplicate reads were removed and read groups were assigned by individual for variant calling using Picard Tools v2.23.3 (http://broadinstitute.github.io/picard/). Nucleotide variants were identified from the resulting bam files using the Genome Analysis Tool Kit (GATK, v4.0.11.0) following the best practices for RNA-seq variant calling[60]. This includes splitting spliced reads, calling variants with HaplotypeCaller (added parameters: --don't-use-soft-clipped-bases -standcall-conf 20.0), and filtering variants with VariantFiltration (added parameters: -window 35 – cluster 3 –filter-name FS -filter FS > 30.0 –filter-name QD -filter QD < 2.0). Variants were further filtered to include a list of high quality SNPs for identification of the subject of origin of individual cells by removing all novel variants, maintaining only biallelic variants with MAF greater than 5%, a mix missing of one individual with a missing variant call at a specific site and requiring a minimum depth of two (parameters: --max-missing 1.0 –min-alleles 2 –max-alleles 2 –removeindels –snps snp.list.txt –min-meanDP 2 –maf 0.05 –recode –recode-INFO-all –out).

scRNA-seq and CITE-seq sample loading and sequencing

PBL or colon single-cell suspensions from each patient were pooled with equivalent number of live cells and resuspended at 1-2.5x10^3 cells/µl in 0.04%BSA/PBS, with the addition of 10 µM Y-27632 (MedChem Express) for colon samples. Samples from unique individuals were pooled, and samples from the proximal (Right,R) or distal (Left,L) colon of the same individual were placed in separate pools, so each sample could later be uniquely identified using demuxlet[17]. For the primary biopsy UC and VDZ analysis, the two pools were loaded into four wells each of a Chromium Single Cell 3′ v2 Reagent Kit (10X Genomics), with a total of 8 wells (**Supplementary Table 2**). 1x10^6 cells of both single-cell colon suspension pools were stained with a custom TotalSeq-A panel, (BioLegend) (**Supplementary Table 3**) according to the manufacturer's instructions and loaded into two wells. For all experiments, 60,000 cells were loaded per well and processed for single-cell encapsulation and cDNA library generation using the Chromium Single Cell 3′ v2 Reagent Kits (10X Genomics). TotalSeq-A library generation was performed according to manufacturer's instructions (BioLegend). Libraries were sequenced on an Illumina NovaSeq6000 in order to obtain 25,000 reads per cell for the gene expression libraries and 10,000 reads per cell for the TotalSeq libraries.

scRNA-seq and CITE-seq data pre-processing, inter-sample doublet detection, and demuxlet

10x Genomics Chromium scRNA-seq data were processed as previously described[27,59]. Briefly, sequencer-obtained bcl files were demultiplexed into individual library fastq trios using the mkfastq program from the Cellranger 3.0.2 suite of tools (https://support.10xgenomics.com). Feature-barcode matrices were obtained for each sample by aligning the raw fastqs to GRCh38 reference genome (annotated with Ensembl v85) using the Cellranger count. Raw feature-barcode matrices were loaded into Seurat 3.1.5[61] and low-quality cells (with fewer than 100 features), and features in 3 or fewer cells were dropped from the dataset. The remaining events were assessed for inter-sample doublet detection (generated due to libraries containing samples pooled prior to loading) using Freemuxlet (https://github.com/statgen/popscle), the genotype-free version of Demuxlet[17]. Clusters of cells belonging to the same patient were identified via SNP concordance to a "truth set" generated by bulk RNASeq. Briefly, the aligned reads from Cellranger were filtered to retain reads overlapping a high-quality list of SNPs obtained from the 1000 Genomes Consortium (1KG)[62]. Freemuxlet was run on this filtered bam using the 1KG vcf file as a reference, the input number of samples/pool as a guideline for clustering groups of cells by SNP concordance, and all other default parameters. Cells are classified as singlets (arising from a single library), doublets (arising from two or more

libraries), or as ambiguous (cells that cannot be accurately assigned to any existing cluster due to a lack of sufficient genetic information). Clusters of cells belonging to a unique sample were mapped to patients using their individual Freemuxlet-generated genotype, and ground truth genotypes per patient identified via bulk RNA-seq. The pairwise discordance between inferred and ground-truth genotypes was assessed using the bcftools gtcheck command[63]. The feature-barcode Matrices were further filtered to remove cells with greater than 50% percent mitochondrial content or ribosomal content, and cells assigned as doublets or ambiguous by Freemuxlet. Visual outliers in the feature-vs-UMIs plots were filtered uniformly across all libraries. The cell cycle state of each cell was assessed using a published set of genes associated with various stages of human mitosis[64].

scRNA-seq and CITE-seq quality control, normalization, and intra-sample heterotypic doublet detection

The filtered count matrices were normalized, and variance stabilized using negative binomial regression via the scTransform method offered by Seurat[65]. The effects of mitochondrial content, ribosomal content, and cell cycle state were regressed out of the normalized data to prevent any confounding signal. The normalized matrices were reduced to a lower dimension using Principal Component Analyses (PCA) and the first 30 principal coordinates per sample were subjected to a non-linear dimensionality reduction using Uniform Manifold Approximation and Projection (UMAP). Clusters of cells sharing similar transcriptomic signals were initially identified using the Louvain algorithm, and clustering resolutions varied between 0. 6 and 1.2 based on the number and variety of cells obtained in the datasets. All libraries were further processed to identify intra-sample heterotypic doublets arising from the 10X sample loading. Processed and annotated Seurat objects were processed using the DoubletFinder package[66]. The prior doublet rate per library was approximated using the information provided in the 10x knowledgebase (https://kb.10xgenomics.com/hc/en-us/articles/360001378811) and this was corrected to account for inter-sample doublets identified by freemuxlet, and for homotypic doublets using the per-cluster numbers in each dataset. Heterotypic doublets were removed. The raw and log-normalized counts per library were then pruned to retain only genes shared by all libraries. Pruned counts matrices were merged into a single Seurat object and the batch (or library) of origin was stored in the metadata of the object. The log-normalized counts were reduced to a lower dimension using PCA and the individual libraries were aligned in the shared PCA space in a batch-aware

manner (Each individual library was considered a batch) using the Harmony algorithm[67]. ADT counts were centered log-ratio (CLR) normalized. The resulting Harmony components were used to generate batch corrected UMAP visualizations and cell clustering.

scRNA-seq and CITE-seq cell annotation and differential expression

For both blood and biopsy scRNAseq and CITEseq, we generated h5ad files with the UMAP, Louvain clusters, and metadata. We then refined the "coarse" and "fine" cell-type annotations in a semi-supervised manner using exploratory CZ CELLxGENE (ExCellxGene) (https://pypi.org/project/excellxgene/), a restructured version of CZ CELLxGENE[68]. Expression of cell-type specific markers were used to assign identities to "coarse" and "fine" clusters, guided by previously described gene sets[11,12,14,31,69]. Cells that were unable to be further categorized by fine annotations were labeled as the coarse parental population-not otherwise specified (NOS). The "Mito Hi immune" cluster consisting of cells with high mitochondrial gene expression were generally not considered in downstream analysis. scRNA-seq and CITE-seq data analysis and visualization were then performed in Jupyter notebooks using Scanpy[70]. To compute differentially express (DE) genes between two conditions, we first subsetted our datasets with a pair of conditions (HC vs UC, UC vs VDZ, and HC vs VDZ). Then, we used the MAST R package v1.20 which implements a negative-binomial model using the zlm method and corrects for differences in sequencing depth across samples[71]. Briefly, for a subsetted dataset of two conditions, we subsetted again for each cell-type (coarse annotation for biopsies, and fine annotation for blood) to identify DE genes for each cell-type between the two conditions. We also corrected for the number of detected genes as a potential confounding variable[71]. P-values were corrected using the Bonferroni correction. Platelets and erythrocytes were excluded from blood DE gene analysis.

Fresh versus cryopreserved biopsy scRNA-seq comparison

For the fresh versus cryopreserved comparison, twelve colon biopsies were divided into two vials, each containing six biopsies, for two donors. The fresh biopsies were stored in Basal Media on ice for 80 min, while the cryopreserved biopsies were transferred into cryovials containing freezing media (90% (v/v) FCS, 10% (v/v) DMSO and 10 μM Y-27632) and immediately placed into a freezing container (Mr Frosty or Coolcell) and stored at -70°C for 80min. The cryopreserved biopsies were then thawed, and both the fresh and cryopreserved biopsies were digested as above. Half of the fresh biopsies from each donor were labeled

with TotalSeq-A0251 barcode sequence GTCAACTCTTTAGCG (Biolegend 394601), and the other half of the fresh biopsy sample was labeled with MULTI-seq lipid-tag barcode sequence CCTTGGCACCCGAGAATTCCAGGAGAAGA[21]. Half of the cryopreserved biopsies from each donor were labeled with TotalSeq-A0252 barcode sequence TGATGGCCTATTGGG (Biolegend 394603), and the other half of the cryopreserved biopsy sample was labeled with MULTI-seq lipid-tag barcode sequence CCTTGGCACCCGAGAATTCCACCACAATG[21]. The MULTI-seq labeled samples were combined into one pool, and the TotalSeq Hasthag samples were combined in a second pool. The two pools were loaded separately into one well each of a Chromium Single Cell 3′ v2 Reagent Kit (10X Genomics). 60,000 cells were loaded per well and processed for single-cell encapsulation and cDNA library generation as described above. Representative UMAPs comparing cryopreserved and fresh biopsies and coarse cell subset annotations (**Fig. 1c, d**), as well as the scRNA-seq pseudobulk DE genes (**Fig. 1f**), were generated from the MULTI-seq labeled samples as described above. Quantitation of cell subset frequency was performed on both MULTI-seq and TotalSeq barcoded samples (**Fig. 1e**).

Mass Cytometry (CyTOF) sample staining and acquisition.

A 37-parameter CyTOF panel was designed (**Supplementary Table 3**). All mass cytometry antibodies were conjugated in-house to their corresponding metal isotope. Metals were conjugated according to the manufacturer's instructions (Fluidigm, South San Francisco, CA, USA). In brief, this process consisted of loading the metal to a polymer for 1h at RT. The unconjugated antibody is transferred into a 50 kDA Amicon Ultra 500 V-bottom filter (Fisher Scientific, Hampton, NH, USA) and reduced for 30 min at 37°C with 1:125 dilution of Tris (2-carboxyethyl) phosphine hydrochloride (TCEP) (ThermoFisher, Waltham, MA, USA). Subsequently, the column was washed twice with C-buffer (Fluidigm) and the metal-loaded polymer was suspended in 200 µL of C-buffer in the 3 kDA Amicon Ultra 500 mLV-bottom filter. The suspension was transferred to the 50 kDA filter containing the antibody and incubated for 1.5h at 37°C. After incubation, antibodies were washed three times with W-buffer (Fluidigm) and quantified for protein content using Nanodrop. Once the concentration was determined the antibodies were resuspended at a concentration of 0.2 mg/mL with Antibody Stabilizer (Boca Scientific, Dedham, Ma, USA) and stored at 4°C. Optimal concentrations for all antibodies were determined by different rounds of titrations. The staining protocol was optimized to use each antibody in aliquots of 6 million cells as previously described[72].

CyTOF Panel Design, Staining, and Acquisition.

CyTOF was performed on paired peripheral blood and colon biopsies obtained from the twelve patients. Single-cell suspensions of colon biopsies from the right and left colon were pooled to ensure sufficient cell counts per donor. Dead cells were labeled with Cisplatin (Fluidigm) according to the manufacturer's instructions, washed in FACS buffer, and then stored at -80°C until staining. Samples were then thawed and washed with FACS buffer. Prior to staining with the antibody panel (**Supplementary Table 3**), cells from each patient were barcoded using a unique set of metals, enabling sample identification as previously described[73,74]. The barcode staining was performed following the manufacturer's instructions (Fluidigm, South San Francisco, CA, USA). Briefly, each sample was incubated for 15 min at RT on a shaker (200rpm) with a barcoding solution containing 10 µL of barcode in 1x Perm Buffer solution (Fluidigm, Cat#201057) diluted in cell staining media (CSM, Fluidgim, Cat#201068). Samples were then washed, centrifuged, and resuspended in CSM. Subsequently, extracellular staining was performed for 30 min at 4°C. After incubation, the samples were washed with CSM and centrifuged before resuspending in 1x Permeabilization Buffer (eBioscience™ Permeabilization Buffer Cat# 00-8333-56) for 10min at 4°C. The samples were then washed and incubated with Ir-intercalator (Biolegend CNS, San Diego, CA, USA) diluted 1:500 in 4% fresh PFA for 20 min at RT. After incubation, samples were washed and kept at 4°C overnight in EQ^{TM} bead solution (Fluidigm Cat#201078) diluted in MaxPar Water (Fluidigm Cat# 201069) at 1.2x10^{6} cells/mL. Samples were analyzed on the CyTOF®2 instrument (Fluidigm).

CyTOF data analysis

After acquisition, the .fcs files obtained were concatenated, normalized to the EQ^{TM} calibration beads, and de-barcoded using CyTOF software (Fluidigm). FlowJo software was used for confirming the elimination of the EQ^{TM} calibration beads, concatenating, and manually gating the files. Singlets were gated by Event Length and DNA. Live cells were identified as cisplatin-negative. The unsupervised analysis was performed using an R-based Cytometry Clustering Optimization aNd Evaluation (Cyclone) pipeline developed by the UCSF Data Science CoLab (https://github.com/UCSF-DSCOLAB/cyclone)[75]. Specifically, the data were preprocessed, arcsinh transformed (cofactor 5) and then clustered using FlowSOM[76]. We used default values for FlowSOM parameters except for the grid size. A grid size of "3x7" was chosen based on a local minimum of Davies-Bouldin Index (DBI). The clustering was visualized using UMAP, which was calculated using uwot

package in R. The pre-cluster median expression levels of each of the 37 antibodies panel for each cluster were used to annotate clusters. This was plotted as a heatmap. In parallel, supervised analysis was performed on the same dataset defining cell subsets based on canonical markers and followed the scheme illustrated in **Extended Data Fig. 9** and **Supplementary Table 4**. Additionally, the supervised analysis was used to further define cell subsets expressing $\alpha_4\beta_7$. Finally, specific populations and markers of the focused panel were manually gated to validate and extend the results from the unsupervised analysis.

Histology FFPE Tissue Microarray (TMA) construction

Colon biopsies from patients were fixed in 10% neutral-buffered formalin (Millipore Sigma) for 16-24 hours, washed in PBS three times, then placed in 70% ethanol and stored at RT until paraffin-embedding by the Biospecimen Resource Program (BIOS) at UCSF. Sectioning, hematoxylin and eosin (H&E), and high-resolution (40X) scanning were performed according to standard protocols. H&E histologic severity quantification was performed using the Geboes scoring system[77]. Tissue microarrays were constructed with 2 mm tissue cores from all twelve patients. The recipient TMA block was sectioned with a clearance angle of 10° and a thickness of 4 µm or 5 µm along the width of the block and used for H&E staining and multiplexed RNA-ISH. The TMA block was stored at -20 °C in order to reduce sample degradation and preserve RNA detection in the transcriptomic assays[78]. Indeed, freshly cut TMA slides were prepared before each experiment accordingly to the type of spatial assay performed.

CODEX multiplexed tissue staining, imaging and data analysis

Colon biopsies from the FFPE TMA block were mounted on coverslips provided by Akoya Biosciences and prepared according to the CODEX® User Manual. Briefly, FFPE TMAs were sectioned onto poly-L-lysine-coated coverslips with a thickness of 5 µm. TMA coverslips were stored individually at 4 °C to avoid tissue damage until the experiment run. Conjugation of DNA oligonucleotides to purified antibodies, antibody validation and titration, and CODEX multicycle reactions were optimized and performed by Akoya Biosciences according to the protocol previously described[22]. TMA coverslips were pretreated on a hot plate at 55°C with tissue facing up for 20-25 minutes, then positioned on a rack at RT for 5min to allow the tissues to cool down. Subsequently, deparaffinization and hydration steps were performed. Next, the TMA coverslips were submerged in a beaker containing antigen retrieval solution (1x Tris/EDTA buffer, pH 9) and placed in a pressure cooker for 20 min. After incubation, samples were cooled at RT for 10 min, washed in distilled water

for 2 min (2x), incubated in a hydration buffer for 2 min (2x), and then equilibrated in a staining buffer for 20-30 min before antibody staining. A customized CODEX panel of 28 antibodies was used and each CODEX®-tagged antibody had a barcode that was complementary to a specific reporter; all related details are summarized in **Supplementary Table 3**. A single staining step with the antibody cocktail solution containing blocking buffer and the panel of antibodies was performed on the tissues for 3 hours at RT in a humidity chamber. After incubation, the TMA coverslips were washed with the staining buffer for 2 min (2x) then the coverslips were incubated with post staining fixing solution (2% PFA) for 10 min at RT. Subsequently, TMA coverslips were washed in 1x PBS (3x), placed in ice-cold methanol for 5 min and transferred rapidly in 1x PBS for three consecutive washes. After the washing steps, TMA coverslips were placed on a tray and tissues were incubated with a final fixative solution for 20 min in a humidity chamber. After incubation, TMA coverslips were rinsed with 1x PBS (3x) and were ready for the CODEX® multicycle experiment. Images were collected using a Keyence BZ-X800 Fluorescent microscope configured with fluorescent channels (ATTO550, Cy5, AF647 and AF750) and equipped with a cooled CCD camera. The resolution was 0.25 μm per pixel. Images for the 28 DNA-conjugated antibodies were acquired over 13 cycles of staining. In each cycle, the reporters revealed up to three markers of interest (and DAPI) simultaneously. After each cycle of imaging, the reporters were removed from the tissue by a gentle isothermal wash. Each core was imaged with a 20x objective. Images were processed, stitched with background subtraction and deconvolution, and aligned into a 28-color overlay figure for the selected markers. Cell segmentation was performed using HALO 3.4 image analysis software (Indica Labs), DAPI was used as the reference nuclear dye. Nuclear contrast threshold, minimum nuclear intensity, and nuclear size were determined using the pre-trained Nuclear Segmentation algorithm “AI default” and kept constant for the entire analysis. Membrane segmentation was done considering a cytoplasm radius of 6μm based on average cell sizes determined using reference H&E images. After cell segmentation, comma-separated value (.csv) files containing signal intensity at single-cell level were generated from each core and used for unsupervised analysis. Data were imported into R and the unsupervised analysis was performed using the Cyclone pipeline as described above[75]. The number of clusters was defined using the FlowSOM clustering (grid size “4x6”) and then visualized using UMAPs. The median level of expression of each of the 28 antibodies panel for each cluster was used to annotate the clusters. This was plotted as a Heatmap. Subsequently, based on the unsupervised clusters, a supervised

analysis in HALO was performed defining 18 phenotypes based on positive and/or negative channel selection criteria using the HiPlex FL v 4.1.3 module. Cell frequency for each phenotype was exported as a percentage of positive cells over the total number of cells defined. To define cell interactions, spatial plots were generated for each core using the Spatial Analysis module in HALO. Nearest Neighbor Analysis was conducted on the object data from each suitable core in order to determine the average distance between two cells or object populations. For this experiment, a total of 20 cores were imaged and 15 of them were selected for further analysis based on the quality of the core. Low-quality cores were excluded if they were grossly damaged or detached during processing, or if they had poor nuclei staining that precluded cell segmentation. For Nearest Neighbor Analysis 12 cores were considered, all the cores containing less than 5 unique cells per phenotypes of interest were excluded from the analysis.

MIBI staining, data acquisition and analysis

Slide preparation, staining, antibody optimization, and imaging were performed by the MIBI Core at UCSF. Antibodies were conjugated to metal-loaded MIBItags (Ionpath) according to the manufacturer's instructions. Initial imaging QC was performed on the conjugated antibodies and compared to already established positive controls of FFPE spleen and tonsil tissue. The final 39-plex antibody panel for MIBI-TOF is reported in **Supplementary Table 3**. TMA slides containing 20 cores of colon tissues were sectioned (5 µm section thickness) from paraffin tissue blocks on gold and tantalum-sputtered microscope slides. Slides were baked at 70°C overnight, followed by deparaffinization and rehydration with washes in xylene (3x), 100% ethanol (2x), 95% ethanol (2x), 80% ethanol (1x), 70% ethanol (1x) and distilled water (1x). Next, tissues underwent antigen retrieval by submerging the slides in 1X Target Retrieval Solution (pH 9, DAKO Agilent) and incubating at 97 °C for 40 min in a Lab Vision PT Module (Thermo Fisher Scientific). After cooling to RT for 30 min, slides were washed in 1X TBS-T pH7.6 (IONpath). Subsequently, all tissues underwent two rounds of blocking, the first to block endogenous biotin and avidin with an Avidin/Biotin Blocking Kit (BioLegend). Tissues were then washed with wash buffer and blocked for 11 hours at RT with 1X TBS with 5% (v/v) normal donkey serum (Sigma-Aldrich). The first antibody cocktail was prepared in 1X TBS-T 5% (v/v) normal donkey serum (Sigma-Aldrich) and filtered through a 0.1µm centrifugal filter (Millipore) prior to incubation with tissue overnight at 4 °C in a humidity chamber. Following the overnight incubation, slides were washed twice for 5 min in 1X TBS-T pH7.6. The second day, an antibody cocktail was prepared as described and incubated

with the tissues for 1h at 4 °C in a humidity chamber. Following staining, slides were washed twice for 5 min in wash buffer and fixed in a solution of 2% glutaraldehyde (Electron Microscopy Sciences) solution in low-barium PBS for 5 min. Slides were washed in PBS (1x), 0.1 M Tris at pH 8.5 (3x) and distilled water (2x) and then dehydrated by washing in 70% ethanol (1x), 80% ethanol (1x), 95% ethanol (2x) and 100% ethanol (2x). Slides were dried under vacuum prior to imaging. Imaging was performed using a MIBIscope (IonPath) with a Hyperion ion source. Xe+ primary ions were used to sequentially sputter pixels for a given field of view (FOV). The following imaging parameters were used: acquisition setting, 80 kHz; field size, 400 µm x 400 µm at 1,024 ×1,024 pixels; dwell time, 24 ms; median gun current on tissue, 1.45 nA Xe+; ion dose, and 3.75 nAmp h per mm2 (450 µm2 FOVs). Mass correction was done using MIBI/O (IONpath) with their standard JSON file.

FOV images were analyzed using the HALO software and the HiPlex FL v 4.1.3 module was used. Cellular segmentation was performed using the Histone H3 nuclear DNA marker as the reference nuclear dye. Nuclear contrast threshold, Minimum nuclear intensity, and nuclear size were determined using the traditional segmentation method and kept constant throughout the entire image analysis. Membrane segmentation was done using EpCAM as the reference dye, and a cytoplasm radius of 6 µm was set based on average cell sizes determined using reference H&E images. 20 phenotypes each corresponding to a major cell type were created based on positive and or negative channel selection criteria. To define cell interactions, spatial plots were generated for each suitable FOV using the Spatial Analysis module. Nearest Neighbor Analysis was conducted on the object data in order to determine the average distance between two cells or object populations. A total of 37 FOV images were acquired and 32 of them were used for phenotype identification and quantification. FOVs that contained exclusively lymphoid aggregates, with no mucosal or submucosal cellular compartments, were excluded. Among the 32 FOVs analyzed, 29 were selected for Nearest Neighbor Analysis based on the number of cells per phenotype. FOVs containing less than 5 unique cells per phenotype of interest were excluded from the analysis.

Multiplexed (12-plex) RNA *In Situ* Hybridization (RNA-ISH)

FFPE TMA slides containing colon biopsies from our study cohort were used for multiplexed RNA-ISH. The assay was performed following the manufacturer's instructions (HiPlex RNAscope, ACDBio). Briefly, FFPE TMA slides were deparaffinized sequentially with xylene (2x, 5 min) and 100% ethanol (2x, 2 min). After

deparaffinization, a retrieval step of 15 min at 99°C was performed. Slides were permeabilized with Protease III for 30 min at 40°C. The 12 probes were hybridized for 2 hours at 40°C and amplified (3 amplification steps, 30 min each at 40 °C) using the HybEZ hybridization system. Probes were designed for genes identified as cell type markers and based on transcript levels obtained from the scRNA-seq data. Probes are listed in **Supplementary Table 3**. After probe hybridization and amplification steps, slides were hybridized with the first round of fluorophores for 15 min at 40°C then washed, counterstained with DAPI, and mounted with ProLong Gold Antifade Mountant. The first round of imaging was performed by scanning each full core using the automated Zeiss Axioscanner Z1 with a 20X objective on Orca Flash 4.0 v2 (Hamamatsu) camera in fluorescence channels (DAPI, FITC/GFP, Cy3/Atto550, and Cy5). The image scanner was controlled using ZEN 3.1 software. After each round of imaging, the coverslip was removed by soaking in 4x SSC buffer for 30 min and fluorophores were cleaved using manufacturer cleaving solution. Then the slides were washed and prepared for the second round of fluorophores hybridization and imaging, these last steps were repeated for a total of four rounds. All images were acquired at the UCSF HDFCCC Histology and Biomarker Core. A total of 21 core images were obtained and 19 of them were used for further analysis. Low-quality cores were excluded if they were grossly damaged or detached during processing. Images obtained from the four rounds of staining were then registered, fused, and analyzed using HALO 3.1 image analysis software (Indica Labs). For this analysis, we used the following modules: TMA and FISH v3.1.3. Cell detection was based on Nuclei staining (DAPI) with traditional nuclei segmentation type, nuclear contrast threshold was set at 0.5 with an intensity of 0.015 and aggressiveness of 0.6. The nuclear size was ranging from 5 to 150 (μm), the minimum roundness of segmentation was set at 0.05 and the cytoplasm radius was set at 1.5. For the analysis, the FISH score was set at 2+ minimum copies/cell, and phenotypes were defined by exclusive channels and according to the round of imaging. Data were expressed as the percentage of positive cells among the total number of cells detected.

Highly multiplexed (960-plex) CosMx RNA-ISH tissue processing, staining, imaging and data analysis

FFPE TMA processing, staining, imaging, and cell segmentation were performed as previously described[48]. Briefly, 5μm fresh sections were cut from a FFPE TMA block on the back of a VWR Superfrost Plus Micro Slide (Cat# 48311-703) using a microtome, placed in a heated water bath and adhered. Slides were then dried at 37 °C overnight and stored at 4 °C. Manual FFPE tissue preparation, ISH hybridization, coverslip

application, and cyclic RNA readout on the SMI were performed as previously described[61]. After all cycles were completed, additional visualization markers for morphology and cell segmentation were added including pan-cytokeratin, and CD45, CD3, and CD298/B2M, and DAPI. Twenty-two 0.985mm × 0.657 mm FOV were selected, five were ultimately eliminated due to poor tissue adherence or low gene count per cell. The SMI optical system has an epifluorescent configuration based on a custom water objective (13X/0.82 NA). The SMI uses widefield illumination, with a mix of lasers and light-emitting diodes (130 W cm–2 at 488 nm, 69 W cm–2 at 530 nm, 26 W cm–2 at 590 nm, 81 W cm–2 at 647 nm) that allow imaging of Alexa Fluor-488, Atto 532, Dyomics Dy-605 and Alexa Fluor-647, as well as cleaving of photolabile dye components. The camera was a FLIR BFS-U3_200S6M-C based on the IMX183 Sony industrial CMOS sensor, and sampling at the image plane was 180 nm per pixel. A 3D multichannel image stack was obtained at each FOV location, with the step size of 0.8μm. Registration, feature detection, localization, determination of the presence individual transcripts, and cell segmentation were performed as previously described[48]. The final segmentation mapped each transcript location in the registered image to the corresponding cell, as well as to the cell compartment (nuclei, cytoplasm, membrane), where the transcript is located. Other features/properties generated included shape (area, aspect ratio) and fluorescence intensity statistics (minimum, maximum, average) per cell. Single-cell spatial RNA-ISH results were analyzed using scanpy[70] and squidpy[79]. Low-quality cores were excluded if they were extensively damaged or detached during processing, or if they had poor nuclei staining that precluded cell segmentation. Cells with <10 unique genes per cell or <50 counts per cell were filtered out, and the data were further normalized to a total count of 10,000 transcripts per cell, log-transformed, and scaled such that each gene possessed zero mean and unit variance across cells as previously described[80]. For cell type identification and annotation of CosMx results alone, principal components were first computed using scanpy's tl.pca() function with default settings. UMAP plots and leiden clustering were calculated using tl.umap() and tl.leiden(). To annotate the computed clusters, we examined the top differentially expressed genes in each cluster using the tl.rank_genes_groups() function and compared with known marker genes for the various cell types. We then refined the "coarse" and "fine" cell-type annotations in a semi-supervised manner using exploratory CZ CELLxGENE (ExCellxGene)[68]. Neighborhood enrichment analysis was performed using squidpy's sq.gr.nhood_enrichment() function.

Antibodies and reagents

Antibodies and reagents for all experiments are listed in **Supplementary Table 3.**

Gene Set Enrichment Analysis (GSEA) on a validation cohort

The bulk transcriptomic study (GSE73661)[1] performed on colonic biopsies obtained from UC patients before and after VDZ treatment was downloaded from GEO database and used for GSEA analysis[49]. Samples were divided into pre- and post-VDZ treatment and responders (R, responding at week 52, n=9) or non-responders (NR, not responding at week 52). Three comparisons were made: 1-pre- vs post-VDZ treatment for responders, 2-pre- vs post-VDZ treatment for non-responders, and 3-responders (at either week 6,12 or 52) vs non-responders (at either week 12 or 52) pre-VDZ treatment (n=11 for R and n=9 for NR). Data were normalized and expressed as Z-scores before reading into the GSEA program (version 4.3.2). Based on our gene expression data we defined 14 cell type gene signatures with ≥10 genes (**Supplemental Table 5)**. GSEA analysis was performed for each gene signature. The number of permutations was set at 1000, no collapse dataset, chip Affymetrix Human Gene 1.0 ST Array Affymetrix Human Gene 1.0 ST Array, t-test. For each analysis and gene set, a Normalized Enrichment Score (NES) was calculated and only NES with a p-value <0.5 and adjusted q-value (FDR) <0.1 were considered significant. A leading edge analysis was performed to display overlaps between all cell subsets and to elucidate key genes that contributed the most to the enrichment signal of a specified gene sets.

Statistics

Non-parametric comparisons were performed using one-way ANOVA Kruskal-Wallis test for multiple groups or Mann-Whitney test for two groups, followed by a two-stage linear step-up procedure of Benjamini, Krieger and Yekutieli to correct for multiple comparisons by controlling the false discovery rate (FDR). Parametric comparisons for multiple groups were performed using two-way ANOVA if comparing multiple variables per group or one-way ANOVA if comparing one variable per group, followed by FDR correction. The q-value is the FDR-adjusted p-value, and q<0.1 was used as the threshold for discovery, unless otherwise indicated. Adjusted p<0.05, after correcting for multiple comparisons, was used as the threshold for statistical significance. Categorical variables were analyzed by Chi-square test as indicated. For MAST DE gene analysis, p-values were corrected using Bonferroni correction, and corrected p-value of <0.05 was used as the threshold for statistical significance. Additional analyses were performed using GraphPad PRISM 9. Hierarchically clustered heatmaps and correlation heatmap were generated with the Morpheus software

(https://software.broadinstitute.org/morpheus/) using a metric of Euclidean distance and the average linkage method in both rows and columns.

Code and data availability

All code used in this study including R markdowns and Jupyter notebooks are available on the Ulcerative Colitis project GitHub repository **(**https://github.com/mkattah/UC_VDZ**).** Processed and annotated objects are saved in AnnData (h5ad) format[81]. These AnnData objects are accessible in Figshare (fresh versus cryopreserved scRNA-seq 10.6084/m9.figshare.21936240; blood scRNA-seq 10.6084/m9.figshare.21900948; biopsy scRNA-seq 10.6084/m9.figshare.21919425; biopsy CITE-seq 10.6084/m9.figshare.21919356; PBL CyTOF 10.6084/m9.figshare.21977834; biopsy CyTOF 10.6084/m9.figshare.21977798; CosMx 960-plex RNA-ISH,10.6084/m9.figshare.21919338). Publicly available microarray data (GSE73661) were downloaded from the NCBI gene expression omnibus.

AUTHOR CONTRIBUTIONS

Conceptualization: MGK; patient recruitment and sample collection: FBV, JLB, KB, NE, SL, DRS, JPT, UM, MGK; sample processing (scRNA-seq/CITE-seq, CyTOF): EM, IR, GL, JT, AS, WE, DYO, AJC, MGK scRNA-seq/CITE-seq analysis: YJK, CA, AR, GF, AP, MGK; CyTOF analysis: EM, IR, RP, JT, AS, GF, AJC, MGK; MIBI and CODEX processing and analysis: EM, IR, GL, FBV, JLB, AR, ST, MN, SJC, GF, MGK; RNA-ISH: EM, YJK, IR, GL, LD, FBV, JLB, RP, MN, SJC, GF, AP, MGK; data curation: EM, YJK, LD, MGK; GSEA: EM; supervision: GF, AP, AJC, MGK; funding acquisition: MGK; all authors contributed to manuscript preparation.

ACKNOWLEDGEMENTS

MGK was supported by a Career Development Award from the Crohn's and Colitis Foundation and NIH K08 DK123202. Michael George Kattah, M.D., Ph.D., holds a Career Award for Medical Scientists from the Burroughs Wellcome Fund. This work was also supported by funding from UCSF ImmunoX. Schematics created with BioRender.com. This work was also supported by RRID:SCR_018206, DRC Center Grant NIH P30 DK063720, NIH S10 1S10OD018040-01 (CyTOF), and NIH S10 1S10OD025187-01 (MIBI). We would like to acknowledge Nanostring CosMx™ SMI Technology Access Program, Akoya Biosciences Spatial Tissue Exploration Program (STEP), ACDBio, and the Indica Labs HALO team. We thank James Lord for helpful discussion. We also acknowledge the Research Core of the UCSF Division of Hospital Medicine.

COMPETING FINANCIAL INTERESTS

S. Lewin has received research support from Takeda. N. El-Nachef is a consultant for Ferring, Federation Bio Grant and receives funding from Finch Therapeutics, Seres, Freenome, and Assembly Biosciences. U. Mahadevan serves as a consultant for Abbvie, BMS, Boeringher Ingelheim, Gilead, Janssen, Lilly, Pfizer, Prometheus biosciences, Protagonist, Rani Therapeutics, Surrozen, and Takeda. D. Oh has received research support from Merck, PACT Pharma, the Parker Institute for Cancer Immunotherapy, Poseida Therapeutics, TCR2 Therapeutics, Roche/Genentech, and Nutcracker Therapeutics, and travel/accommodations from Roche/Genentech. The Combes lab has received research support from Eli Lilly and Genentech and A. Combes consults for Foundery Innovations. The Kattah lab receives research support from Eli Lilly. M. Kattah is a consultant for Sonoma Biotherapeutics.

Supplementary material

Supplementary Table 1. Baseline demographic and clinical data for study participants. Categorical variables were analyzed by Chi-square test and continuous variables were compared using one-way ANOVA with FDR correction or Mann-Whitney test where appropriate. ns, not significant; n/a, not applicable.

Supplementary Table 2. Biospecimens analyzed by each multi-omics method. R, right colon; L, left colon; 5-ASA, 5-aminosalicylate; CLR1, right colon biopsy 1; CLL1, left colon biopsy; Y, yes; N/A, not applicable. FOV-field of view.

Supplementary Table 3. Antibodies and reagents.

Supplementary Table 4. Cell subset phenotypes for supervised and unsupervised analyses for each multi-omics method.

Supplementary Table 5. Cell subset-specific gene signatures used for Gene Set Enrichment Analysis (GSEA). Numeric ID, Affymetrix numeric probe identifier corresponding to each gene.

Supplementary Table 6. Cell counts and percentages of hematopoietic, stromal and endothelial, and intestinal epithelial cell (IEC) subsets for each patient biospecimen and multi-omic method.

REFERENCES

1. Arijs, I. *et al.* Effect of vedolizumab (anti-α4β7-integrin) therapy on histological healing and mucosal gene expression in patients with UC. *Gut* **67**, 43–52 (2018).

2. Verstockt, B. *et al.* Expression Levels of 4 Genes in Colon Tissue Might Be Used to Predict Which Patients Will Enter Endoscopic Remission After Vedolizumab Therapy for Inflammatory Bowel Diseases. *Clin. Gastroenterol. Hepatol.* **18**, 1142-1151.e10 (2020).
3. Feagan, B. G. *et al.* Vedolizumab as Induction and Maintenance Therapy for Ulcerative Colitis. *N. Engl. J. Med.* **369**, 699–710 (2013).
4. Luzentales-Simpson, M., Pang, Y. C. F., Zhang, A., Sousa, J. A. & Sly, L. M. Vedolizumab: Potential Mechanisms of Action for Reducing Pathological Inflammation in Inflammatory Bowel Diseases. *Front. Cell Dev. Biol.* **9**, 612830 (2021).
5. Soler, D. *et al.* The Binding Specificity and Selective Antagonism of Vedolizumab, an Anti-$\alpha_4\beta_7$ Integrin Therapeutic Antibody in Development for Inflammatory Bowel Diseases. *J. Pharmacol. Exp. Ther.* **330**, 864–875 (2009).
6. Abreu, M. T. *et al.* Transcriptional Behavior of Regulatory T Cells Predicts IBD Patient Responses to Vedolizumab Therapy. *Inflamm. Bowel Dis.* izac151 (2022) doi:10.1093/ibd/izac151.
7. Becker, E. *et al.* Residual homing of α4β7-expressing $\beta1^+$ $PI16^+$ regulatory T cells with potent suppressive activity correlates with exposure-efficacy of vedolizumab. *Gut* **71**, 1551–1566 (2022).
8. Rath, T. *et al.* Effects of Anti-Integrin Treatment With Vedolizumab on Immune Pathways and Cytokines in Inflammatory Bowel Diseases. *Front. Immunol.* **9**, 1700 (2018).
9. Clahsen, T., Pabst, O., Tenbrock, K., Schippers, A. & Wagner, N. Localization of dendritic cells in the gut epithelium requires MAdCAM-1. *Clin. Immunol.* **156**, 74–84 (2015).
10. Zeissig, S. *et al.* Vedolizumab is associated with changes in innate rather than adaptive immunity in patients with inflammatory bowel disease. *Gut* **68**, 25–39 (2019).
11. Kinchen, J. *et al.* Structural Remodeling of the Human Colonic Mesenchyme in Inflammatory Bowel Disease. *Cell* **175**, 372-386.e17 (2018).
12. Parikh, K. *et al.* Colonic epithelial cell diversity in health and inflammatory bowel disease. *Nature* **567**, 49–55 (2019).
13. Boland, B. S. *et al.* Heterogeneity and clonal relationships of adaptive immune cells in ulcerative colitis revealed by single-cell analyses. *Sci. Immunol.* **5**, eabb4432 (2020).

14. Smillie, C. S. *et al.* Intra- and Inter-cellular Rewiring of the Human Colon during Ulcerative Colitis. *Cell* **178**, 714-730.e22 (2019).
15. Konnikova, L. *et al.* High-dimensional immune phenotyping and transcriptional analyses reveal robust recovery of viable human immune and epithelial cells from frozen gastrointestinal tissue. *Mucosal Immunol.* **11**, 1684–1693 (2018).
16. Mitsialis, V. *et al.* Single-Cell Analyses of Colon and Blood Reveal Distinct Immune Cell Signatures of Ulcerative Colitis and Crohn's Disease. *Gastroenterology* (2020) doi:10.1053/j.gastro.2020.04.074.
17. Kang, H. M. *et al.* Multiplexed droplet single-cell RNA-sequencing using natural genetic variation. *Nat. Biotechnol.* **36**, 89–94 (2018).
18. Stoeckius, M. *et al.* Simultaneous epitope and transcriptome measurement in single cells. *Nat. Methods* **14**, 865–868 (2017).
19. Spitzer, M. H. & Nolan, G. P. Mass Cytometry: Single Cells, Many Features. *Cell* **165**, 780–791 (2016).
20. Solé-Boldo, L. *et al.* Single-cell transcriptomes of the human skin reveal age-related loss of fibroblast priming. *Commun. Biol.* **3**, 188 (2020).
21. Kondo, A. *et al.* Highly Multiplexed Image Analysis of Intestinal Tissue Sections in Patients With Inflammatory Bowel Disease. *Gastroenterology* **161**, 1940–1952 (2021).
22. Black, S. *et al.* CODEX multiplexed tissue imaging with DNA-conjugated antibodies. *Nat. Protoc.* **16**, 3802–3835 (2021).
23. Hughes, S. M. *et al.* Cryopreservation of human mucosal tissues. *PLOS ONE* **13**, e0200653 (2018).
24. Keren, L. *et al.* MIBI-TOF: A multiplexed imaging platform relates cellular phenotypes and tissue structure. *Sci. Adv.* **5**, eaax5851 (2019).
25. Liu, A. Y., Bian, H., Huang, L. E. & Lee, Y. K. Transient cold shock induces the heat shock response upon recovery at 37 degrees C in human cells. *J. Biol. Chem.* **269**, 14768–14775 (1994).
26. Hao, Y. *et al.* Integrated analysis of multimodal single-cell data. *Cell* **184**, 3573-3587.e29 (2021).
27. Combes, A. J. *et al.* Global absence and targeting of protective immune states in severe COVID-19. *Nature* **591**, 124–130 (2021).

28. Picotto, G., Morse, L. R., Nguyen, N., Saltzman, J. & Battaglino, R. TMEM176A and TMEM176B Are Candidate Regulators of Inhibition of Dendritic Cell Maturation and Function after Chronic Spinal Cord Injury. *J. Neurotrauma* **37**, 528–533 (2020).
29. Mattiola, I., Mantovani, A. & Locati, M. The tetraspan MS4A family in homeostasis, immunity, and disease. *Trends Immunol.* **42**, 764–781 (2021).
30. Duhalde Vega, M. *et al.* PD-1/PD-L1 blockade abrogates a dysfunctional innate-adaptive immune axis in critical β-coronavirus disease. *Sci. Adv.* **8**, eabn6545 (2022).
31. Martin, J. C. *et al.* Single-Cell Analysis of Crohn's Disease Lesions Identifies a Pathogenic Cellular Module Associated with Resistance to Anti-TNF Therapy. *Cell* **178**, 1493-1508.e20 (2019).
32. Smids, C. *et al.* Intestinal T Cell Profiling in Inflammatory Bowel Disease: Linking T Cell Subsets to Disease Activity and Disease Course. *J. Crohns Colitis* **12**, 465–475 (2018).
33. Maul, J. *et al.* Peripheral and intestinal regulatory CD4+ CD25(high) T cells in inflammatory bowel disease. *Gastroenterology* **128**, 1868–1878 (2005).
34. Holmén, N. *et al.* Functional CD4+CD25high regulatory T cells are enriched in the colonic mucosa of patients with active ulcerative colitis and increase with disease activity. *Inflamm. Bowel Dis.* **12**, 447–456 (2006).
35. Yu, Q. T. *et al.* Expression and functional characterization of FOXP3+ CD4+ regulatory T cells in ulcerative colitis. *Inflamm. Bowel Dis.* **13**, 191–199 (2007).
36. Lord, J. D., Valliant-Saunders, K., Hahn, H., Thirlby, R. C. & Ziegler, S. F. Paradoxically increased FOXP3+ T cells in IBD do not preferentially express the isoform of FOXP3 lacking exon 2. *Dig. Dis. Sci.* **57**, 2846–2855 (2012).
37. Lord, J. D. Promises and paradoxes of regulatory T cells in inflammatory bowel disease. *World J. Gastroenterol.* **21**, 11236–11245 (2015).
38. Lyu, M. *et al.* ILC3s select microbiota-specific regulatory T cells to establish tolerance in the gut. *Nature* **610**, 744–751 (2022).
39. Linggi, B. *et al.* Meta-analysis of gene expression disease signatures in colonic biopsy tissue from patients with ulcerative colitis. *Sci. Rep.* **11**, 18243 (2021).

40. Mencarelli, A. *et al.* Highly specific blockade of CCR5 inhibits leukocyte trafficking and reduces mucosal inflammation in murine colitis. *Sci. Rep.* **6**, 30802 (2016).
41. Dotan, I. *et al.* Intestinal epithelial cells from inflammatory bowel disease patients preferentially stimulate CD4+ T cells to proliferate and secrete interferon-γ. *Am. J. Physiol.-Gastrointest. Liver Physiol.* **292**, G1630–G1640 (2007).
42. Wosen, J. E., Mukhopadhyay, D., Macaubas, C. & Mellins, E. D. Epithelial MHC Class II Expression and Its Role in Antigen Presentation in the Gastrointestinal and Respiratory Tracts. *Front. Immunol.* **9**, 2144 (2018).
43. Rao, A., Barkley, D., França, G. S. & Yanai, I. Exploring tissue architecture using spatial transcriptomics. *Nature* **596**, 211–220 (2021).
44. Christopher, J. A. *et al.* Subcellular proteomics. *Nat. Rev. Methods Primer* **1**, 32 (2021).
45. Goltsev, Y. *et al.* Deep Profiling of Mouse Splenic Architecture with CODEX Multiplexed Imaging. *Cell* **174**, 968-981.e15 (2018).
46. Huang, B. *et al.* Mucosal Profiling of Pediatric-Onset Colitis and IBD Reveals Common Pathogenics and Therapeutic Pathways. *Cell* **179**, 1160-1176.e24 (2019).
47. Friedrich, M. *et al.* IL-1-driven stromal–neutrophil interactions define a subset of patients with inflammatory bowel disease that does not respond to therapies. *Nat. Med.* **27**, 1970–1981 (2021).
48. He, S. *et al.* High-plex imaging of RNA and proteins at subcellular resolution in fixed tissue by spatial molecular imaging. *Nat. Biotechnol.* (2022) doi:10.1038/s41587-022-01483-z.
49. Subramanian, A. *et al.* Gene set enrichment analysis: A knowledge-based approach for interpreting genome-wide expression profiles. *Proc. Natl. Acad. Sci.* **102**, 15545–15550 (2005).
50. Mootha, V. K. *et al.* PGC-1α-responsive genes involved in oxidative phosphorylation are coordinately downregulated in human diabetes. *Nat. Genet.* **34**, 267–273 (2003).
51. Soler, D. *et al.* The Binding Specificity and Selective Antagonism of Vedolizumab, an Anti- 4 7 Integrin Therapeutic Antibody in Development for Inflammatory Bowel Diseases. *J. Pharmacol. Exp. Ther.* **330**, 864–875 (2009).
52. Becker, E. *et al.* Limited Dose-Dependent Effects of Vedolizumab on Various Leukocyte Subsets. *Clin. Transl. Gastroenterol.* **13**, e00494 (2022).

53. Lord, J. D. *et al.* Circulating integrin alpha4/beta7+ lymphocytes targeted by vedolizumab have a pro-inflammatory phenotype. *Clin. Immunol.* **193**, 24–32 (2018).
54. Habtezion, A., Nguyen, L. P., Hadeiba, H. & Butcher, E. C. Leukocyte Trafficking to the Small Intestine and Colon. *Gastroenterology* **150**, 340–354 (2016).
55. Alayo, Q. A. *et al.* Systematic Review With Meta-analysis: Safety and Effectiveness of Combining Biologics and Small Molecules in Inflammatory Bowel Disease. *Crohns Colitis 360* **4**, otac002 (2022).
56. Ananthakrishnan, A. N. *et al.* Gut Microbiome Function Predicts Response to Anti-integrin Biologic Therapy in Inflammatory Bowel Diseases. *Cell Host Microbe* **21**, 603-610.e3 (2017).
57. Lee, J. W. J. *et al.* Multi-omics reveal microbial determinants impacting responses to biologic therapies in inflammatory bowel disease. *Cell Host Microbe* **29**, 1294-1304.e4 (2021).
58. Rusu, I. *et al.* Microbial signals, MyD88, and lymphotoxin drive TNF-independent intestinal epithelial tissue damage. *J. Clin. Invest.* **132**, e154993 (2022).
59. Combes, A. J. *et al.* Discovering dominant tumor immune archetypes in a pan-cancer census. *Cell* **185**, 184-203.e19 (2022).
60. Auwera, G. A. *et al.* From FastQ Data to High-Confidence Variant Calls: The Genome Analysis Toolkit Best Practices Pipeline. *Curr. Protoc. Bioinforma.* **43**, (2013).
61. Stuart, T. *et al.* Comprehensive Integration of Single-Cell Data. *Cell* **177**, 1888-1902.e21 (2019).
62. The 1000 Genomes Project Consortium *et al.* A global reference for human genetic variation. *Nature* **526**, 68–74 (2015).
63. Li, H. A statistical framework for SNP calling, mutation discovery, association mapping and population genetical parameter estimation from sequencing data. *Bioinformatics* **27**, 2987–2993 (2011).
64. Dominguez, D. *et al.* A high-resolution transcriptome map of cell cycle reveals novel connections between periodic genes and cancer. *Cell Res.* **26**, 946–962 (2016).
65. Hafemeister, C. & Satija, R. Normalization and variance stabilization of single-cell RNA-seq data using regularized negative binomial regression. *Genome Biol.* **20**, 296 (2019).
66. McGinnis, C. S., Murrow, L. M. & Gartner, Z. J. DoubletFinder: Doublet Detection in Single-Cell RNA Sequencing Data Using Artificial Nearest Neighbors. *Cell Syst.* **8**, 329-337.e4 (2019).

67. Korsunsky, I. *et al.* Fast, sensitive and accurate integration of single-cell data with Harmony. *Nat. Methods* **16**, 1289–1296 (2019).
68. The Tabula Sapiens Consortium & Quake, S. R. *The Tabula Sapiens: a multiple organ single cell transcriptomic atlas of humans*. http://biorxiv.org/lookup/doi/10.1101/2021.07.19.452956 (2021) doi:10.1101/2021.07.19.452956.
69. Fawkner-Corbett, D. *et al.* Spatiotemporal analysis of human intestinal development at single-cell resolution. *Cell* (2021) doi:10.1016/j.cell.2020.12.016.
70. Wolf, F. A., Angerer, P. & Theis, F. J. SCANPY: large-scale single-cell gene expression data analysis. *Genome Biol.* **19**, 15 (2018).
71. Finak, G. *et al.* MAST: a flexible statistical framework for assessing transcriptional changes and characterizing heterogeneity in single-cell RNA sequencing data. *Genome Biol.* **16**, 278 (2015).
72. Ma, T. *et al.* HIV efficiently infects T cells from the endometrium and remodels them to promote systemic viral spread. *eLife* **9**, e55487 (2020).
73. Bodenmiller, B. *et al.* Multiplexed mass cytometry profiling of cellular states perturbed by small-molecule regulators. *Nat. Biotechnol.* **30**, 858–867 (2012).
74. Zunder, E. R. *et al.* Palladium-based mass tag cell barcoding with a doublet-filtering scheme and single-cell deconvolution algorithm. *Nat. Protoc.* **10**, 316–333 (2015).
75. Patel, R. K. *et al.* Cyclone: an accessible pipeline to analyze, evaluate and optimize multiparametric cytometry data. 2023.03.08.531782 Preprint at https://doi.org/10.1101/2023.03.08.531782 (2023).
76. Van Gassen, S. *et al.* FlowSOM: Using self-organizing maps for visualization and interpretation of cytometry data: FlowSOM. *Cytometry A* **87**, 636–645 (2015).
77. Geboes, K. A reproducible grading scale for histological assessment of inflammation in ulcerative colitis. *Gut* **47**, 404–409 (2000).
78. Baena-Del Valle, J. A. *et al.* Rapid Loss of RNA Detection by In Situ Hybridization in Stored Tissue Blocks and Preservation by Cold Storage of Unstained Slides. *Am. J. Clin. Pathol.* **148**, 398–415 (2017).
79. Palla, G. *et al.* Squidpy: a scalable framework for spatial omics analysis. *Nat. Methods* **19**, 171–178 (2022).

80. Liu, J. *et al.* Concordance of MERFISH Spatial Transcriptomics with Bulk and Single-cell RNA Sequencing. *bioRxiv* 2022.03.04.483068 (2022) doi:10.1101/2022.03.04.483068.

81. Virshup, I., Rybakov, S., Theis, F. J., Angerer, P. & Wolf, F. A. anndata: Annotated data. *bioRxiv* 2021.12.16.473007 (2021) doi:10.1101/2021.12.16.473007.

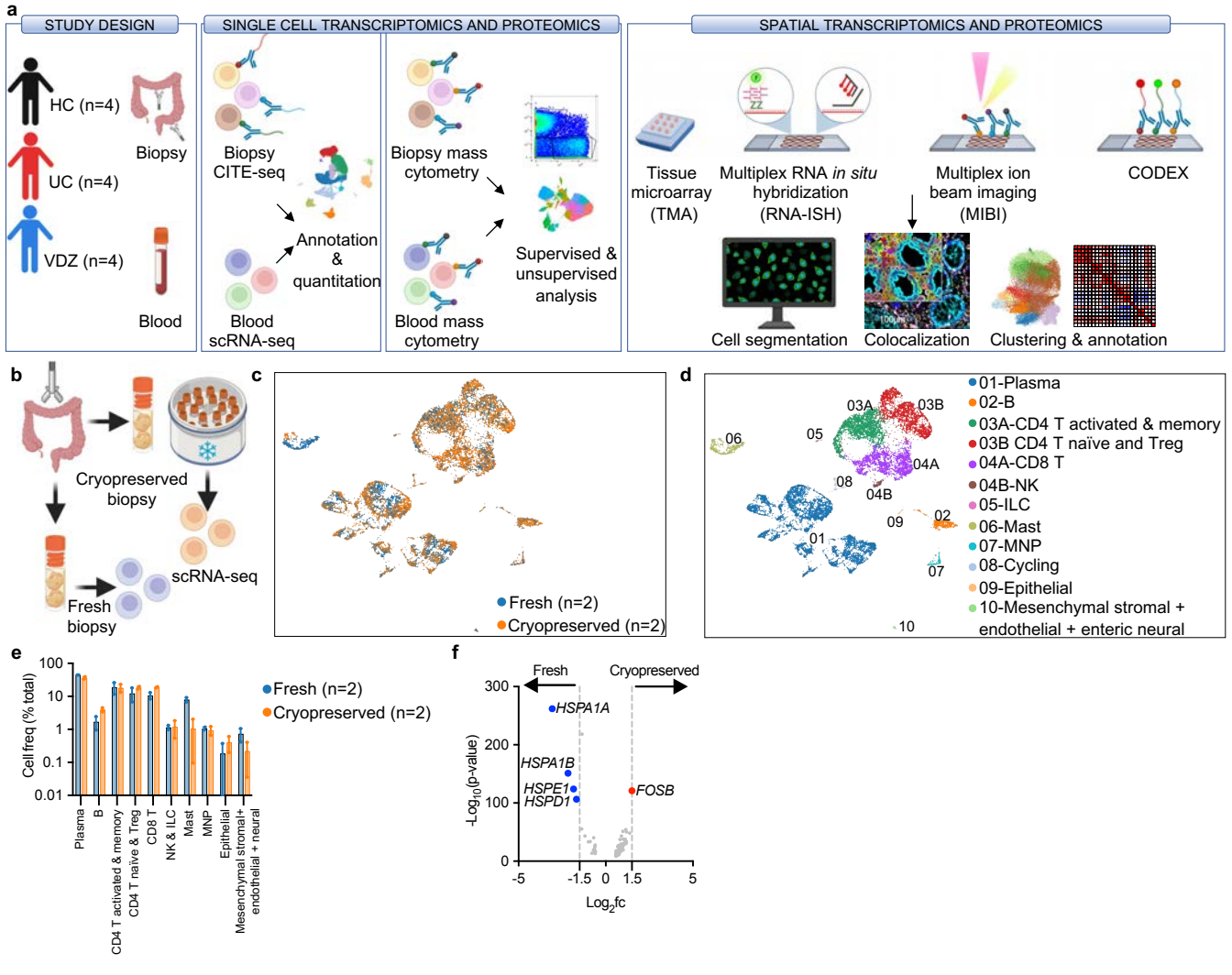

Fig. 1| Schematic of study design and fidelity of cryopreserved compared to fresh biopsy processing for scRNA-seq. a, Schematic of study design. **b,** Schematic of Cryopreserved versus Fresh biopsy processing comparison. **c,d,** Representative UMAP visualization of 10,648 cells for two donors comparing (**c**) Cryopreserved versus Fresh biopsies and (**d**) coarse cell subset annotations. **e**, Cell frequency as a percent of total for coarse cell subsets for two donors comparing Cryopreserved versus Fresh biopsies (mean ± standard error of the mean (SEM); n=number of patients; each dot represents one patient sample; multiple Mann-Whitney tests with FDR correction; q<0.1 threshold for discovery, only significant differences are indicated). **f,** scRNA-seq pseudobulk differentially expressed (DE) genes identified by MAST with $\log_2$ fold-change ($\log_2$fc) >1.5 or <-1.5 in Cryopreserved versus Fresh biopsies (displayed p-values are Bonferroni corrected)**.** Only significant differences are shown. MNP-mononuclear phagocyte.

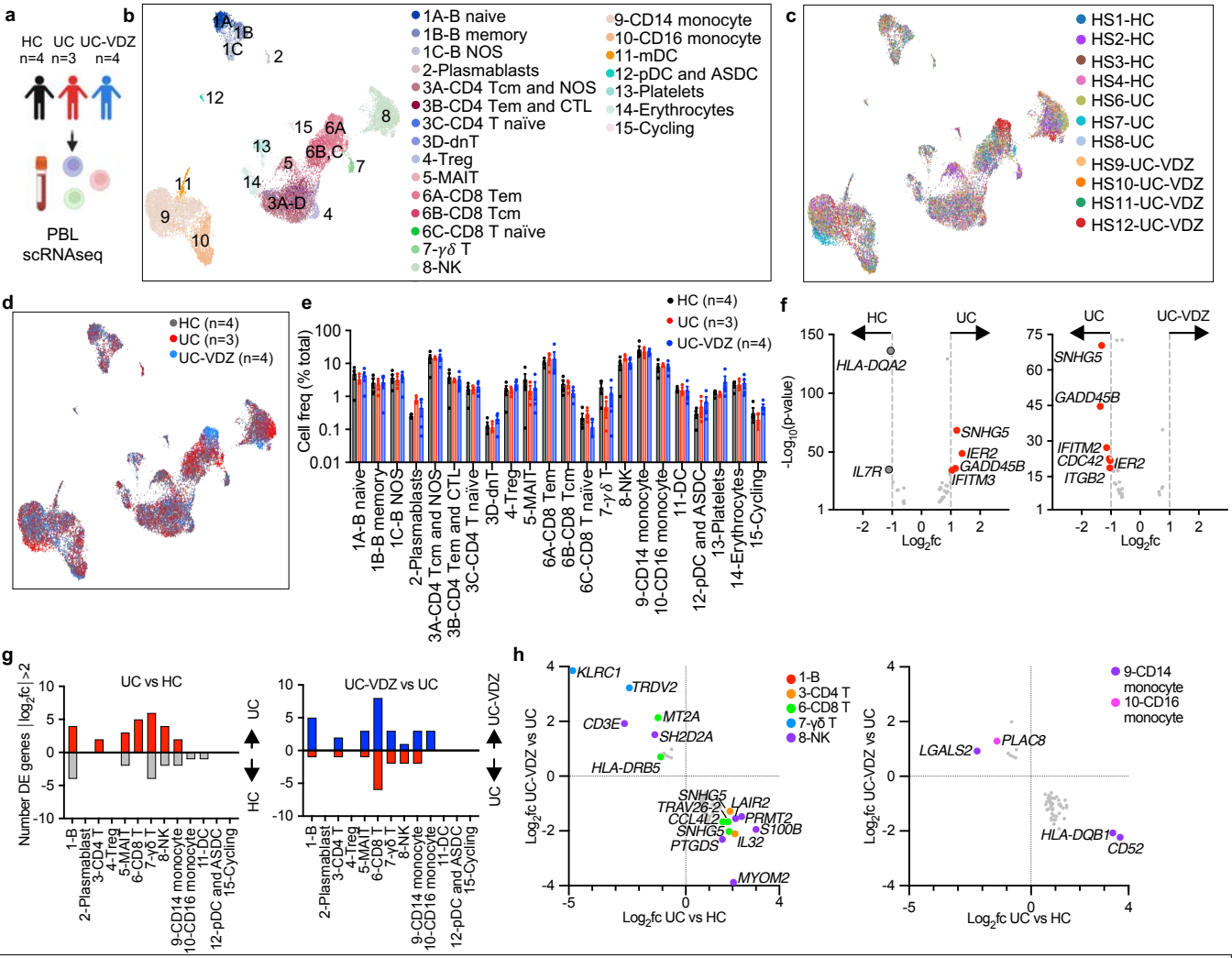

Fig. 2| scRNA-seq of peripheral blood leukocytes (PBLs) reveals correlation of VDZ with DE genes, but not circulating leukocyte subset frequency. a, Schematic of PBL scRNA-seq. **b-d,** UMAP visualization of pooled multiplex scRNA-seq for 20,130 PBLs from HC (n=4), UC (n=3), and UC-VDZ (n=4) patients highlighting (**b**) fine cell annotations, (**c**) patient sample, and (**d**) disease and treatment status. **e,** Cell frequency as a percent of total cells per study subject stratified by disease and treatment status (mean ± SEM; n=number of patients; each dot represents one patient sample; multiple one-way ANOVA Kruskal-Wallis test with FDR correction; q<0.1 threshold for discovery, only significant differences are indicated). **f,** scRNA-seq pseudobulk DE genes in PBLs with $\log_2$fc >1 or <-1 in UC versus HC and UC-VDZ versus UC. **g,** Number of scRNA-seq DE genes in PBL coarse cell annotation subsets identified by MAST with $\log_2$fc >2 or <-2 in UC versus HC and UC-VDZ versus UC. **h,** scRNA-seq DE genes in PBL coarse cell annotation subsets identified by MAST with $\log_2$fc >1.5 or <-1 in UC versus HC and opposing direction $\log_2$fc for UC-VDZ versus UC $\log_2$fc <-0.5 or >0.5, respectively. For panels **f**,**h**, p-values are Bonferroni corrected; ribosomal and mitochondrial genes are not displayed. NOS-not otherwise specified; ASDC-AXL$^+$ SIGLEC6$^+$ myeloid DC; pDC-plasmacytoid DC.

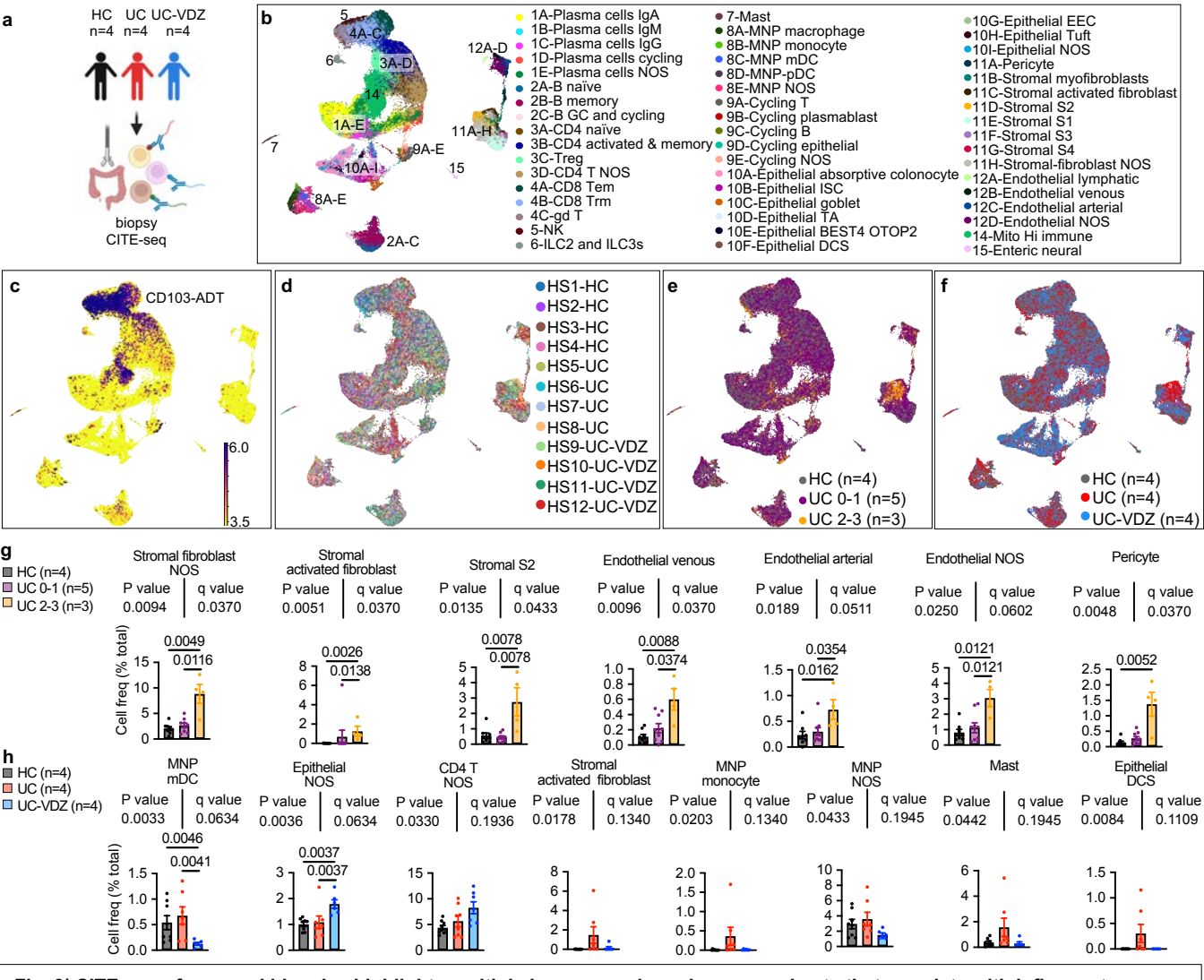

Fig. 3| CITE-seq of mucosal biopsies highlights multiple immune and non-immune subsets that correlate with inflammatory severity, disease status, and VDZ treatment. a, Schematic of CITE-seq of mucosal biopsies. **b-f,** UMAP visualization of CITE-seq for 93,900 cells from HC (n=4), UC (n=4), and UC-VDZ (n=4) patients highlighting (**b**) fine cell subset annotations (**c**) representative CITE-seq antibody-derived tag (ADT) highlighting CD103, (**d**) patient identity, (**e**) endoscopic severity scores, and (**f**) disease and treatment status. **g,h,** Cell frequency for the indicated fine cell subset, expressed as a percent of total cells per study subject, stratified by (**g**) endoscopic severity and (**h**) disease and treatment status (mean ± SEM; n=number of patients; each dot represents one patient sample; multiple one-way ANOVA Kruskal-Wallis tests with FDR correction; q<0.1 threshold for discovery; select subsets are shown with exact p-value and q-value; individual inter-column q-values are displayed only for cell subsets with overall q<0.1). NOS-not otherwise specified.

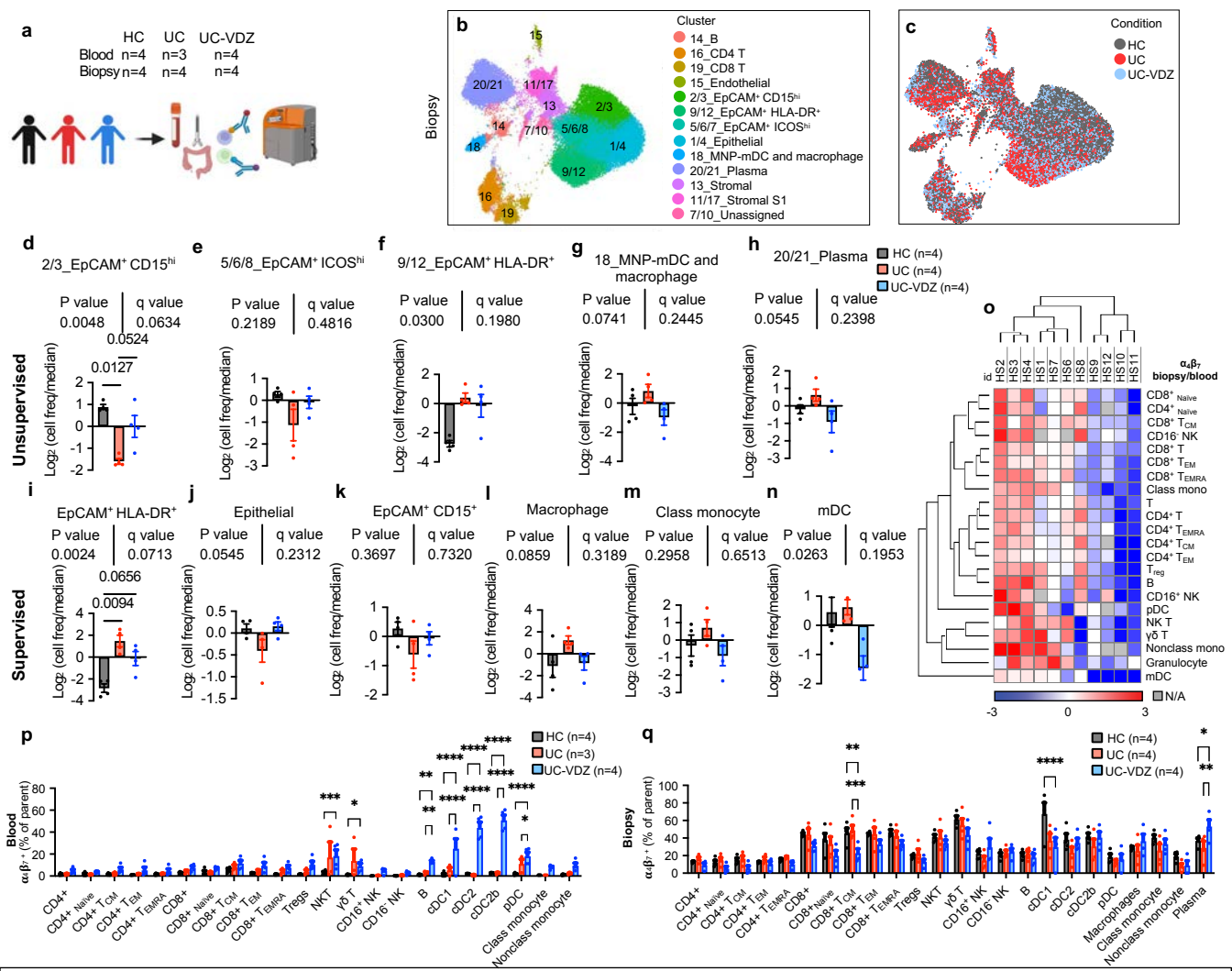

Fig. 4| Unsupervised and supervised CyTOF analysis identifies significant increase in circulating $\alpha_4\beta_7^+$ DCs in UC-VDZ patients. a, Schematic of CyTOF on blood and biopsy samples. **b-c,** UMAP visualization of the indicated samples (60,000 out of 684,249 live cell events displayed for biopsies) highlighting (**b**) annotated clusters, and (**c**) disease and treatment status. **d-n,** Cell frequency of the indicated (**d-h**) unsupervised cluster analysis and (**i-n**) supervised subset analysis among conditions expressed as Log_2 (cell freq/median) (mean ± SEM; n=number of patients; each dot represents one patient sample; multiple one-way ANOVA Kruskal-Wallis test with FDR correction; q<0.1 threshold for discovery; individual inter-column q-values are displayed only for cell subsets with overall FDR corrected q<0.1). **o**, Heatmap of biopsy/blood ratio of $\alpha_4\beta_7^+$ cells for each cell subset by patient (hierarchically clustered by Euclidian distance, average linkage). **p,q,** Percentage of $\alpha_4\beta_7^+$ cells in each defined cell subset per condition for blood and biopsy samples, respectively (mean ± SEM; n=number of patients; each dot represents one patient sample; two-way ANOVA comparing HC vs UC-VDZ and UC vs UC-VDZ with FDR correction; q<0.1 threshold for discovery; *q<0.05; **q<0.01; ***q<0.001; and ****q<0.0001; only significant differences are indicated). Class mono-classical monocyte; Nonclass mono-nonclassical monocyte; mDC-cDC1,cDC2,cDC2b; N/A-Not Applicable.

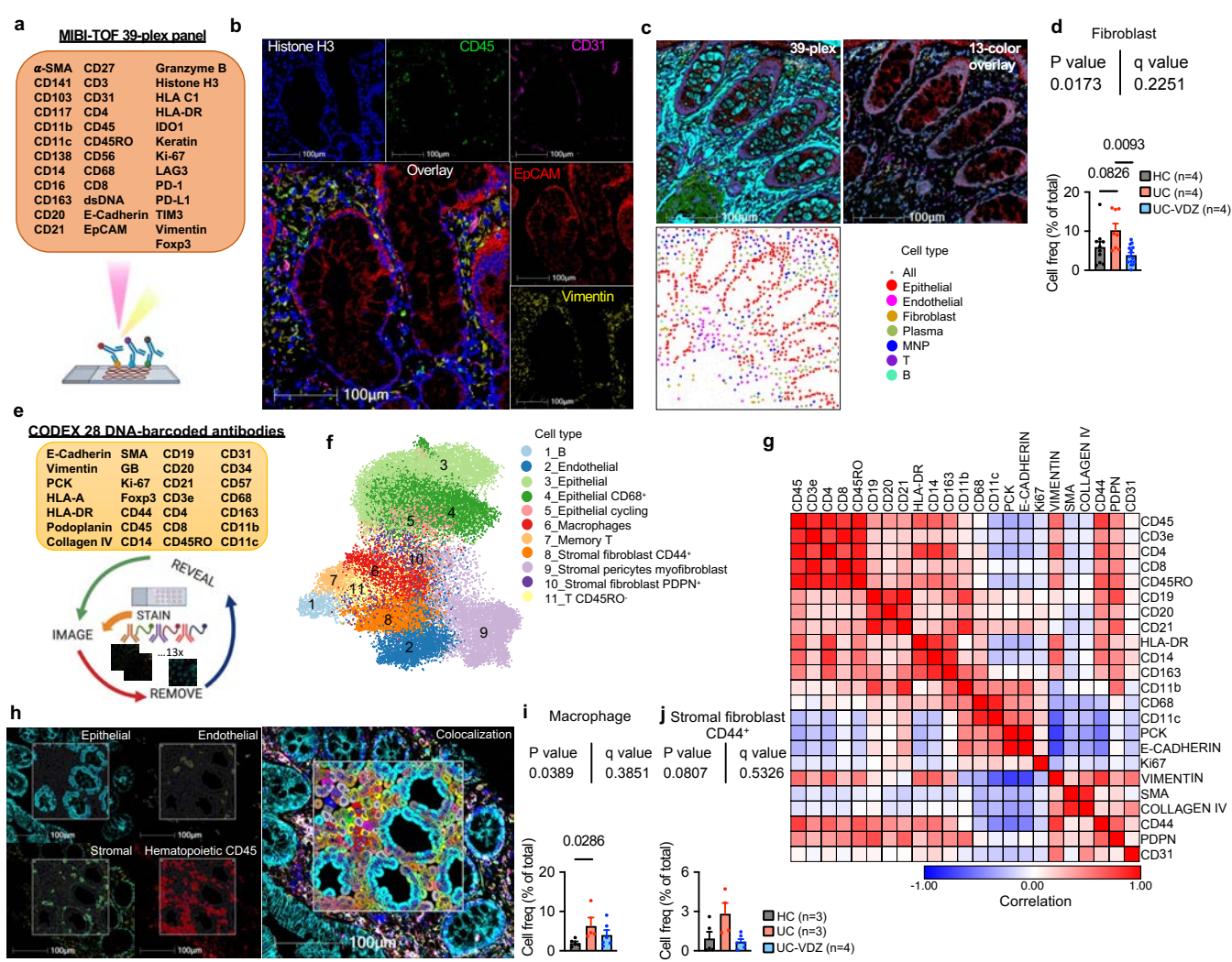

Fig. 5| MIBI and CODEX spatial proteomics using FFPE tissue identifies distinct phenotypes and supports a trend toward fewer activated fibroblasts and MNPs in the colon of UC-VDZ patients. a, Schematic of MIBI workflow and customized antibody panel. **b,** Representative MIBI FOVs for nuclear DNA, indicated major cell lineage markers, and 5 colors overlay. **c**, Representative 39-plex overlay, selected channels and related spatial scatter plots for representative cell subsets coarsely annotated. **d,** Cell frequency as a percent of total cells detected by MIBI for the indicated cell subset. **e,** Schematic of CODEX workflow and antibody panel. **f,** UMAP visualization of 68,804 captured cells (50,000 cells displayed) highlighting annotated clusters. **g,** Pairwise Pearson correlation matrix visualizing the strength of the relationship among 23 selected markers. **h,** Representative CODEX phenotype identification highlighting indicated markers and major phenotype colocalization. **i,j,** Cell frequency as a percent of total cells detected by CODEX for the indicated cell subsets. For panels **d,i,j,** mean ± SEM; n=number of patients; each dot represents one FOV for MIBI or one core for CODEX; multiple one-way ANOVA Kruskal-Wallis test with FDR correction; q<0.1 threshold for discovery; select subsets are shown with exact p-value and q-value; individual inter-column q-values are displayed only for cell subsets with overall q<0.1.

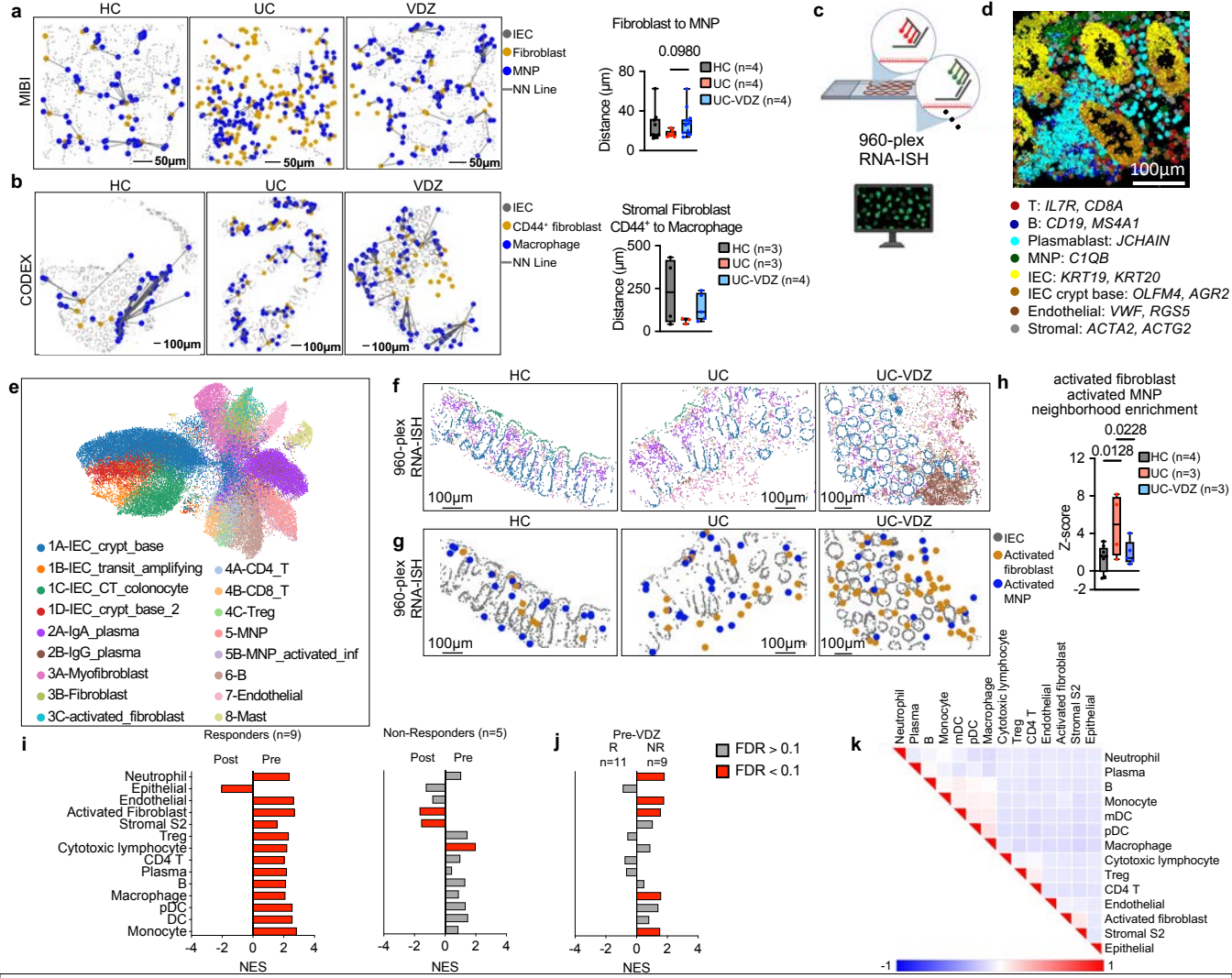

Fig. 6| MNP and fibroblast subsets are in spatial proximity in UC but not UC-VDZ patients, and VDZ non-responders exhibit increased myeloid, stromal, and endothelial signatures pre-treatment. a,b, Representative spatial scatter plots of the indicated cell subsets and nearest-neighbor (NN) analysis for (**a**) MIBI and (**b**) CODEX (box-and-whisker min to max plots; n=number of patients; each dot represents one FOV for MIBI or one core for CODEX; one-way ANOVA Kruskal-Wallis tests with FDR correction; q<0.1 threshold for discovery)**. c,** Schematic of 960-plex RNA-ISH of FFPE TMA. **d,** Representative cell segmentation and probe signal for the indicated cells and genes. **e,** UMAP visualization of 960-plex RNA-ISH for 48,783 cells from HC (n=4), UC (n=3), and UC-VDZ (n=3) patients highlighting the indicated cell subsets. **f,g** representative spatial scatter plots highlighting the indicated cell subsets; the legend for (**f**) is shown in (**e**). **h,** Z-score of activated fibroblast and activated MNP neighborhood enrichment (box-and-whisker min to max plots; n=number of patients; each dot represents one patient sample; one-way ANOVA with FDR correction, q<0.1). **i, j** Normalized Enrichment Scores (NES) in bulk tissue transcriptomic data comparing (**i**) pre- and post-treatment samples for VDZ responders (R) and non-responders (NR), (**j**) pre-VDZ R vs NR. Red bars FDR < 0.1, gray bars FDR > 0.1. **k,** Representative leading edge analysis of significantly enriched gene sets. CT-crypt top.

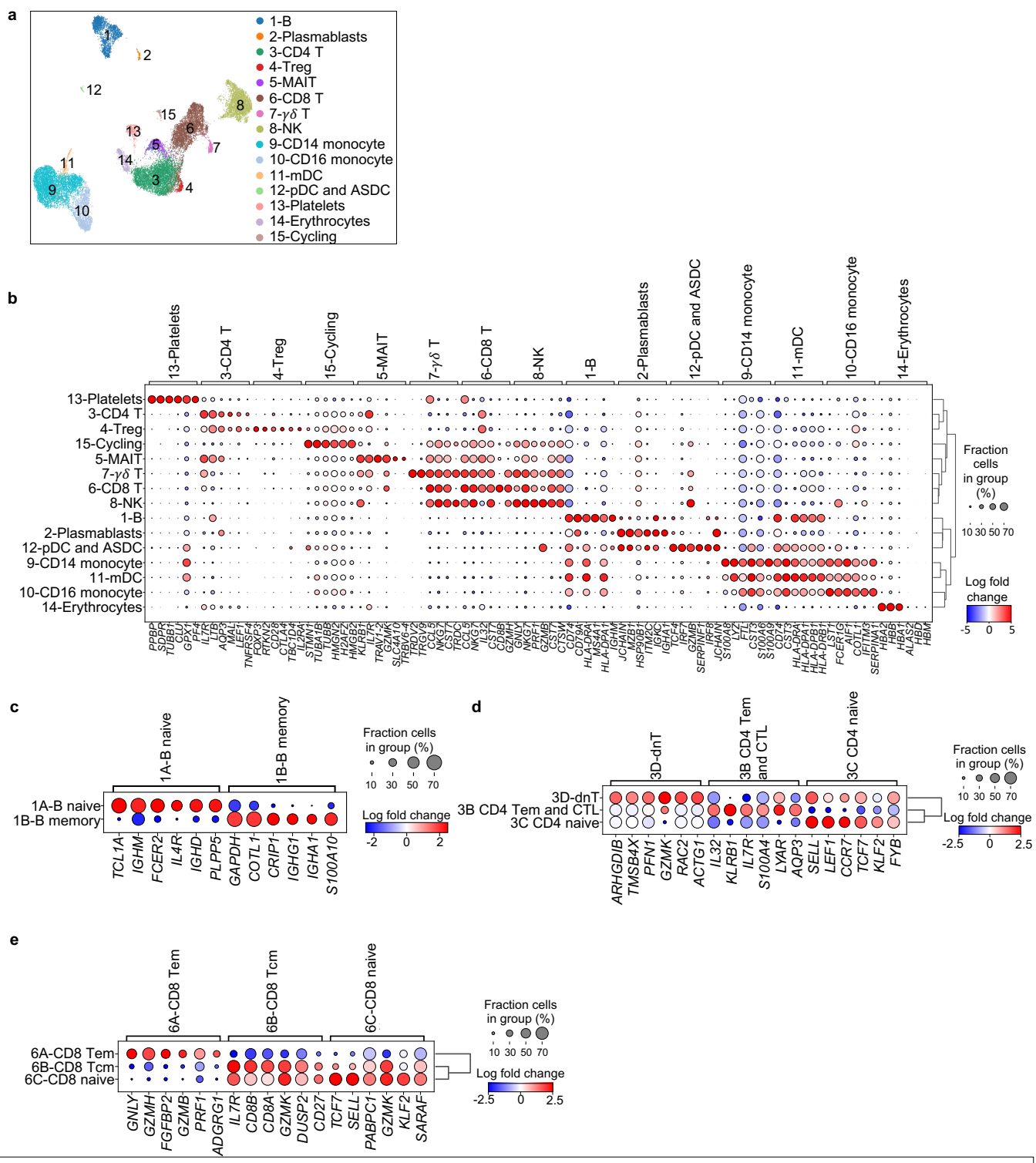

Extended Data Fig.1| Peripheral blood leukocyte (PBL) scRNA-seq coarse cell subset annotations and both coarse and fine cell subset landmark genes. a, UMAP visualization of pooled multiplex peripheral leukocyte scRNA-seq for 20,130 cells from HC (n=4), UC (n=3), and UC-VDZ (n=4) patients highlighting coarse cell subset annotations. **b-e,** Dot plot representation of landmark genes expressed by (**b**) coarse cell subsets and (**c-e**) fine PBL cell subsets. Genes ranked by Wilcoxon rank-sum. Cell subsets without landmark genes above selected minimum log fold change are not displayed.

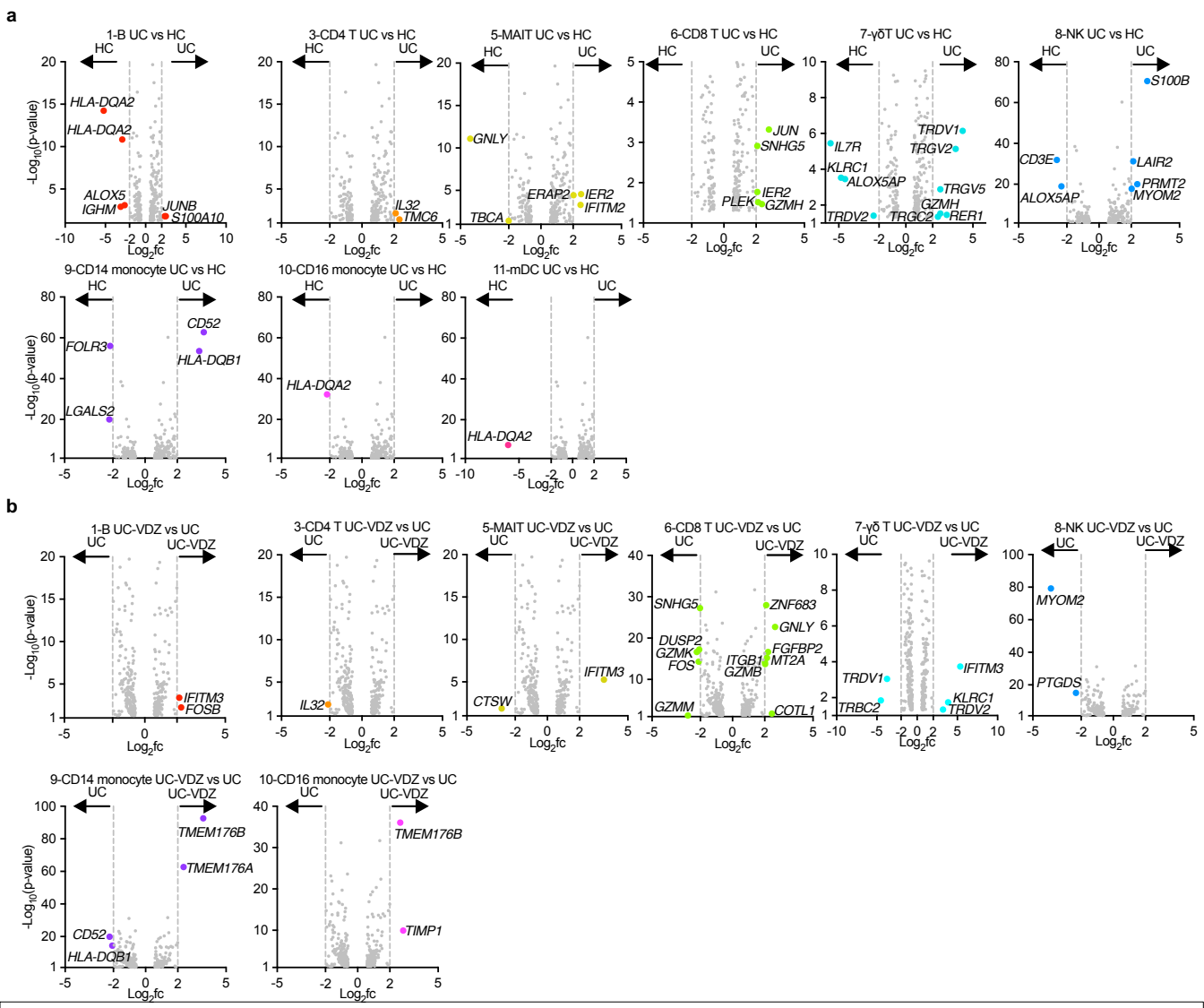

Extended Data Fig.2| Peripheral leukocyte scRNA-seq DE gene expression in cell subsets comparing HC vs UC and UC-VDZ vs UC. a,b, Peripheral leukocyte scRNA-seq DE genes in coarse cell annotation subsets identified by MAST with $\log_2$fc >2 or <-2 in (**a**) UC versus HC and (**b**) UC-VDZ versus UC. All displayed p-values are Bonferroni corrected; ribosomal and mitochondrial genes are not displayed; cell subsets without DE genes are not displayed.

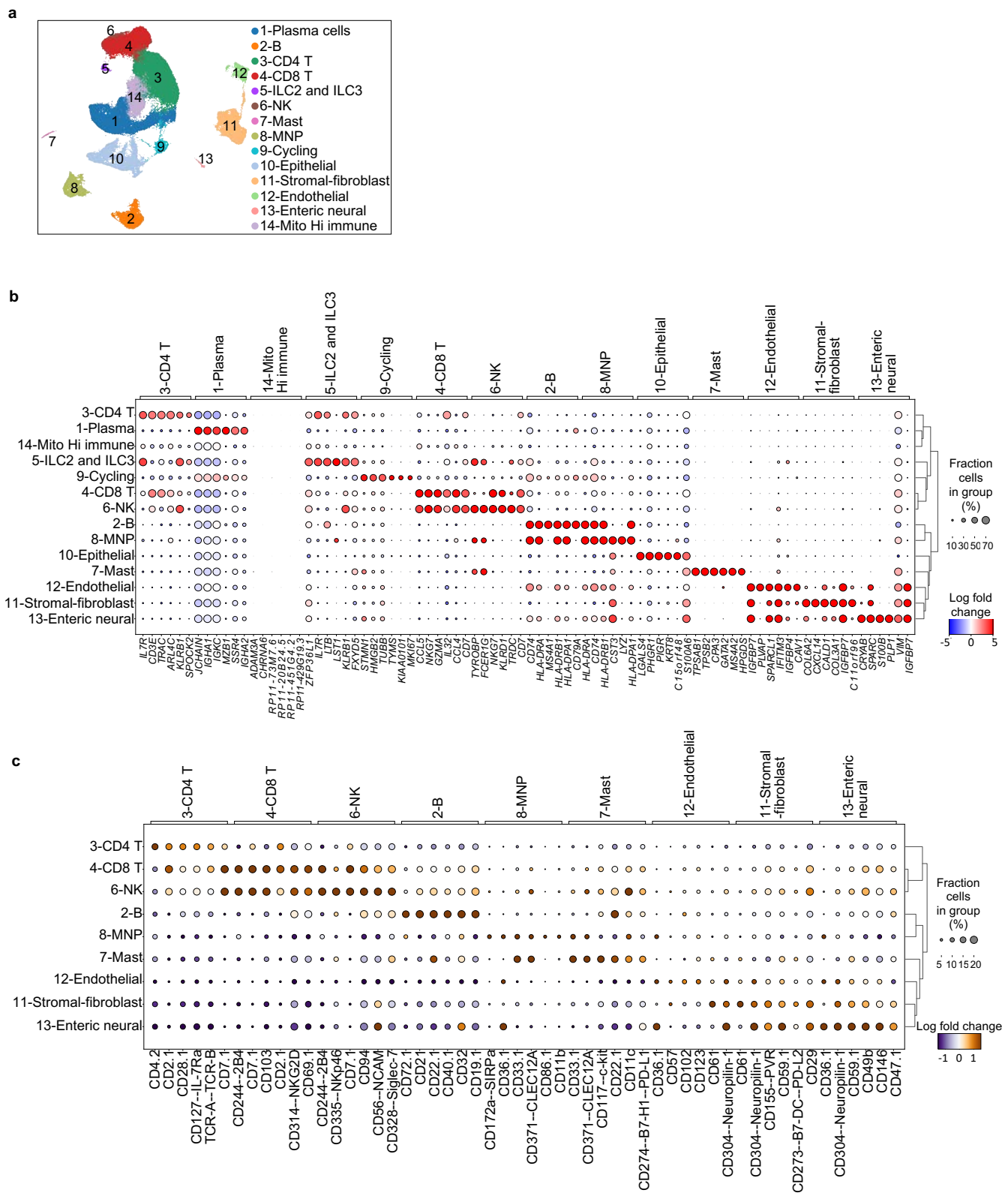

Extended Data Fig.3| Biopsy CITE-seq coarse cell subset annotations and landmark genes and proteins. a, UMAP visualization of CITE-seq for 93,900 cells from HC (n=4), UC (n=4), and UC-VDZ (n=4) patients highlighting coarse cell subset annotations. **b-d,** Dot plot representation of landmark (**b**) genes and (**c**) proteins expressed by indicated coarse biopsy cell subsets. Gene and proteins were ranked by Wilcoxon rank-sum. Cell subsets without landmark genes or proteins above selected minimum log fold change are not displayed.

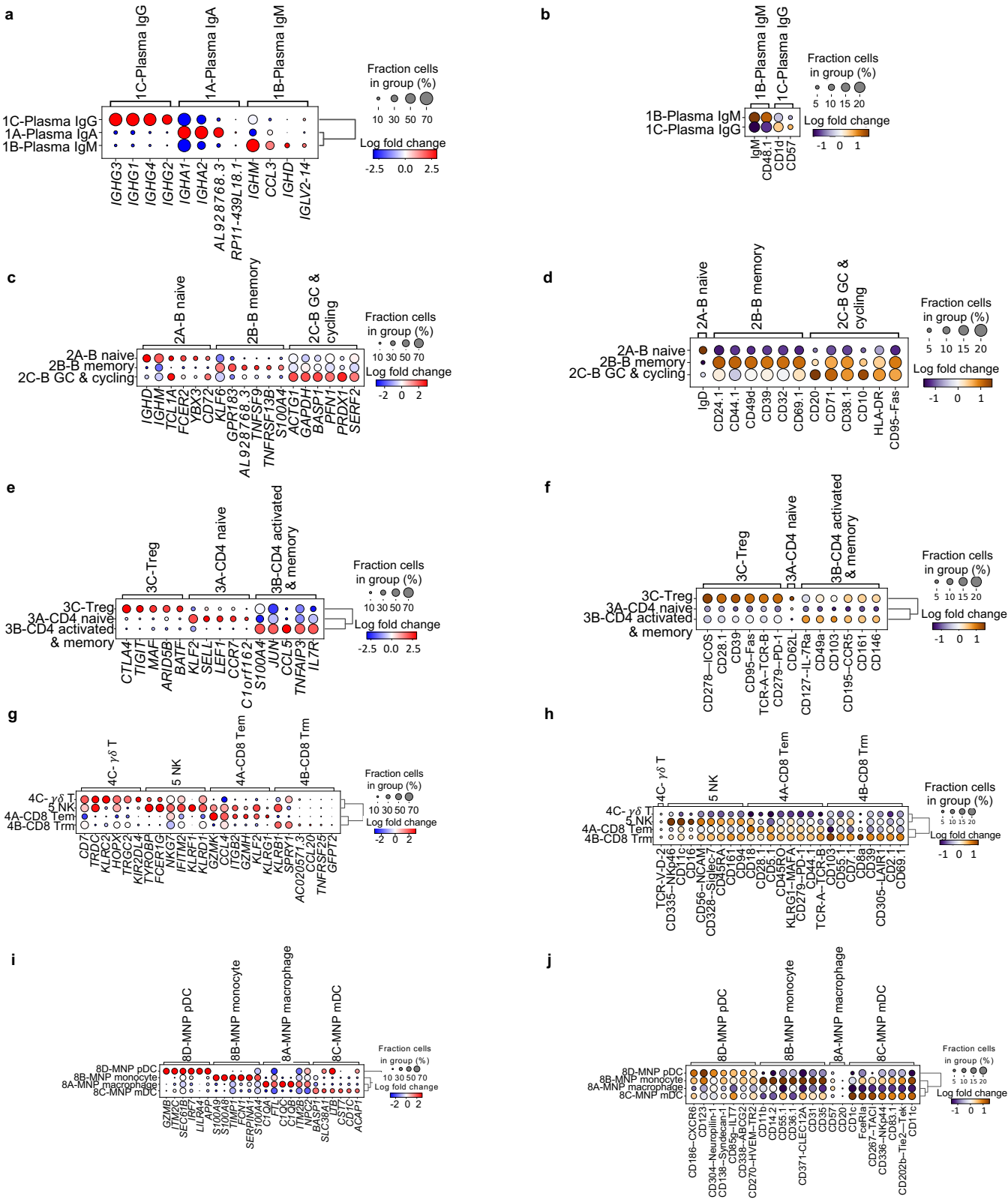

Extended Data Fig.4| Landmark genes and proteins associated fine immune cell subsets in biopsy CITE-seq data. a-j, Dot plot representation of landmark (**a,c,e,g,i**) genes and (**b,d,f,h,j**) proteins expressed by indicated fine biopsy cell subsets. Genes and proteins were ranked by Wilcoxon rank-sum. Cell subsets without landmark genes or proteins above selected minimum log fold change are not displayed.

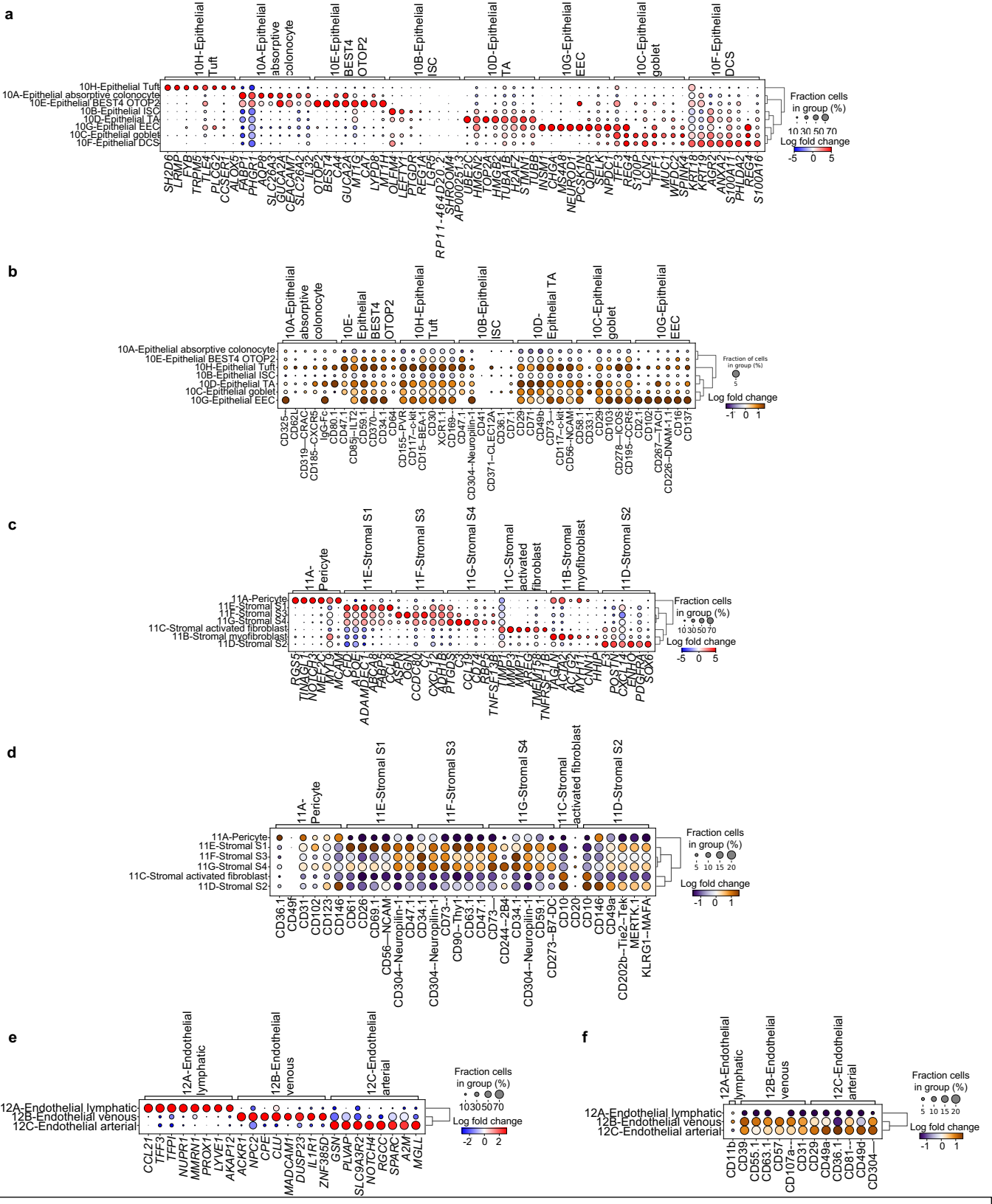

Extended Data Fig. 5| Landmark genes and proteins associated fine non-immune cell subsets in biopsy CITE-seq data. a-j, Dot plot representation of landmark (**a,c,e**) genes and (**b,d,f**) proteins expressed by indicated biopsy fine cell subsets. Genes and proteins were ranked by Wilcoxon rank-sum. Cell subsets without landmark genes or proteins above selected minimum log fold change are not displayed.

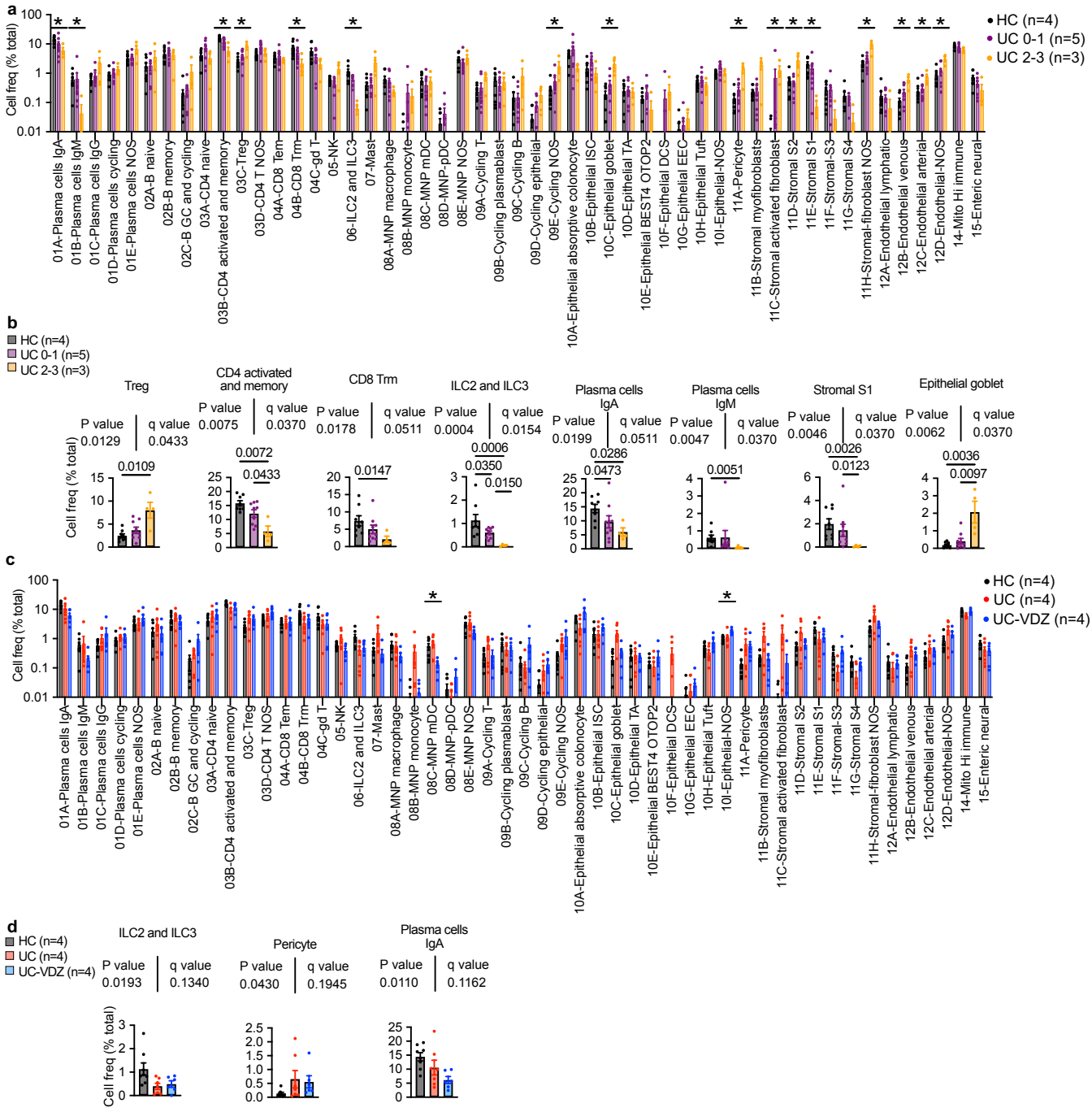

Extended Data Fig. 6| Biopsy CITE-seq cell subsets that correlate with inflammatory severity, disease status, and VDZ treatment. a-d, Cell frequency as a percent of total cells per study subject and fine cell annotation stratified by (**a,b**) endoscopic severity and (**c,d**) disease and treatment status (mean ± SEM; n=number of patients; each dot represents one patient sample). One-way ANOVA Kruskal-Wallis test was performed for each cell subset individually in (**a**, **c**), followed by global FDR correction of all p-values for all cell subsets, with q<0.1 threshold for discovery (*=q<0.1, only significant differences are indicated). Select subsets are shown in (**b, d**) with exact p-value and q-value; individual inter-column q-values are displayed only for cell subsets with overall FDR corrected q<0.1. NOS- "not otherwise specified".

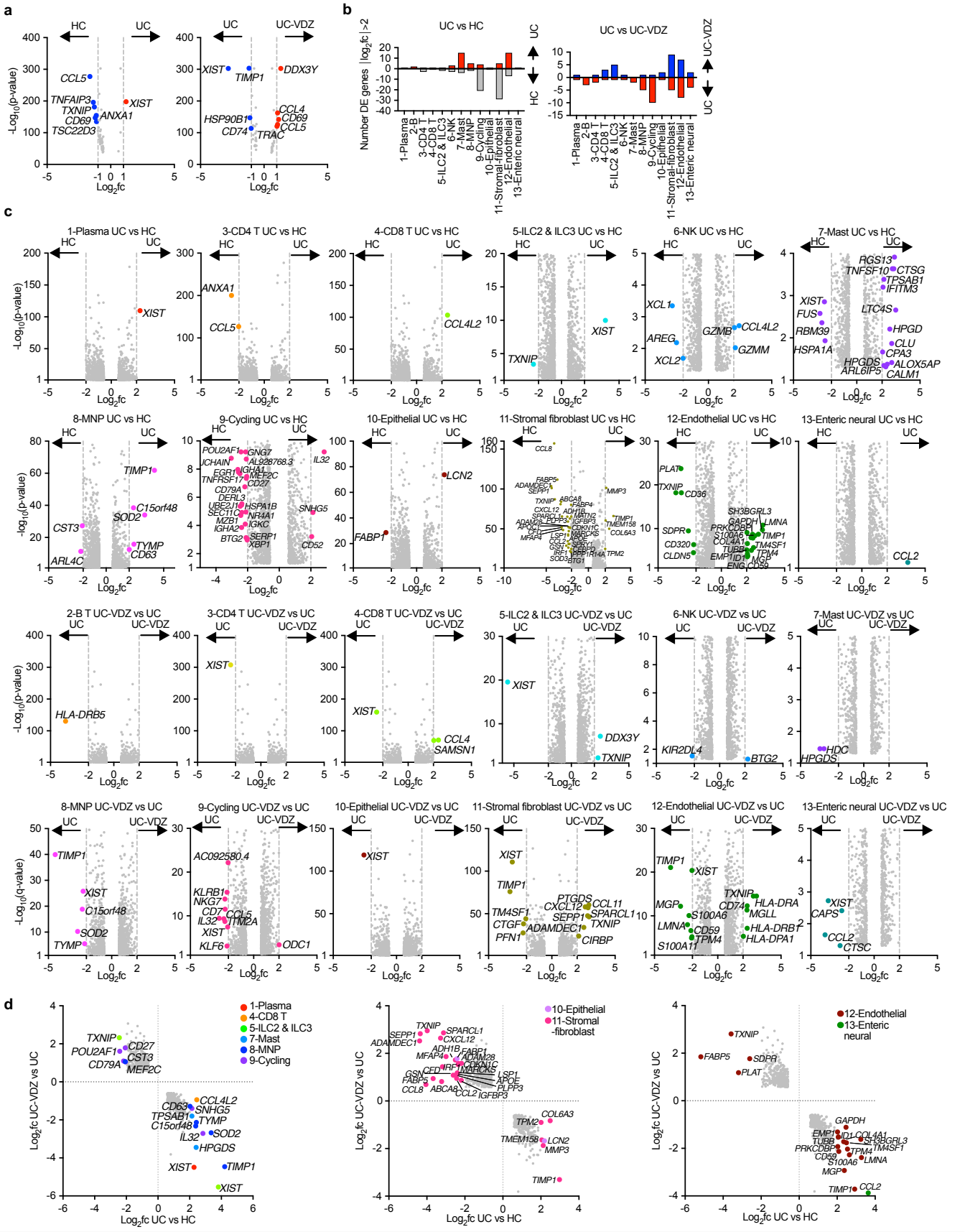

Extended Data Fig.7| Biopsy scRNA-seq DE gene expression in coarse cell subsets comparing HC vs UC and UC-VDZ vs UC. a, scRNA-seq pseudobulk DE genes in biopsies with $\log_2$fc >1 or <-1 in UC versus HC and UC-VDZ versus UC. **b,** Number of scRNA-seq DE genes in biopsy coarse cell annotation subsets identified by MAST with $\log_2$fc >2 or <-2 in UC versus HC and UC-VDZ versus UC. **c,** Biopsy scRNA-seq DE genes in coarse cell annotation subsets identified by MAST with $\log_2$fc >2 or <-2 in UC versus HC and UC-VDZ versus UC. **d,** scRNA-seq DE genes in biopsy coarse cell annotation subsets identified by MAST with $\log_2$fc >2 or <-2 in UC versus HC and opposing direction $\log_2$fc for UC-VDZ versus UC with $\log_2$fc <-0.5 or >0.5, respectively. For panels **a, c, d,** all displayed p-values are Bonferroni corrected; ribosomal and mitochondrial genes are not displayed.

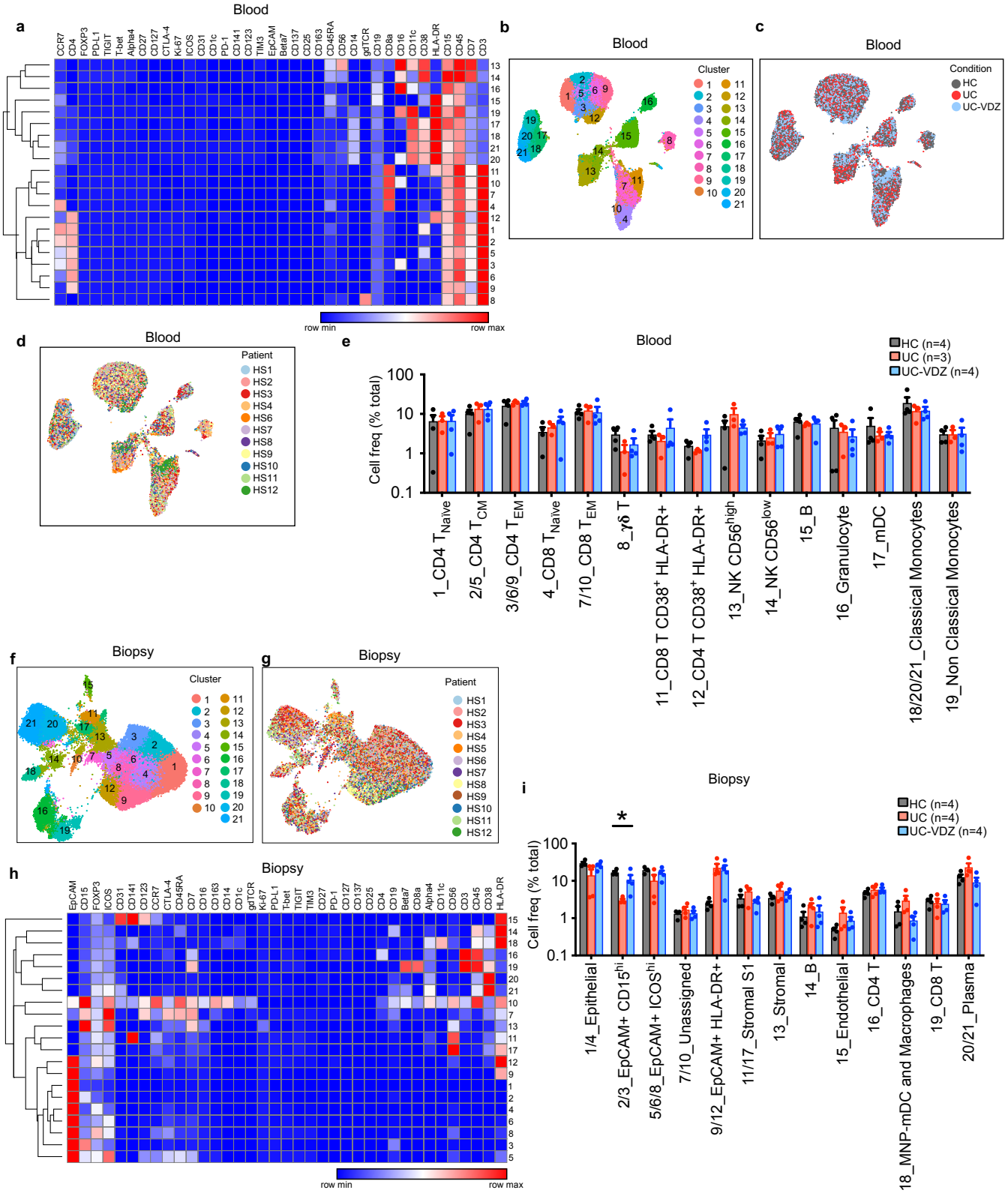

Extended Data Fig. 8| Heatmaps and total frequencies obtained from unsupervised analysis of CyTOF data from blood and biopsies. a,h, Heatmap visualization of mean intensity of each marker for the 21 identified clusters in blood and biopsies, respectively. **b-d,** UMAP visualization of the indicated samples (100,000 out of 1,390,156 live cell events displayed for blood) highlighting (**b**) FlowSOM identified clusters, (**c**) disease and treatment status, and (**d**) patient sample. **e,i,** Cell frequencies for each annotated cell subset per condition (mean ± SEM; n=number of patients; each dot represents one patient sample). **f,g,** UMAP visualization of the indicated samples (60,000 out of 684,249 live cell events displayed for biopsies) highlighting (**f**) FlowSOM identified clusters, and (**g**) patient sample. One-way ANOVA Kruskal-Wallis test was performed for each cell subset individually in panels (**e**) and (**i**), followed by global FDR correction of all p-values for all cell subsets, with q<0.1 threshold for discovery (*q<0.1, only significant differences are indicated).

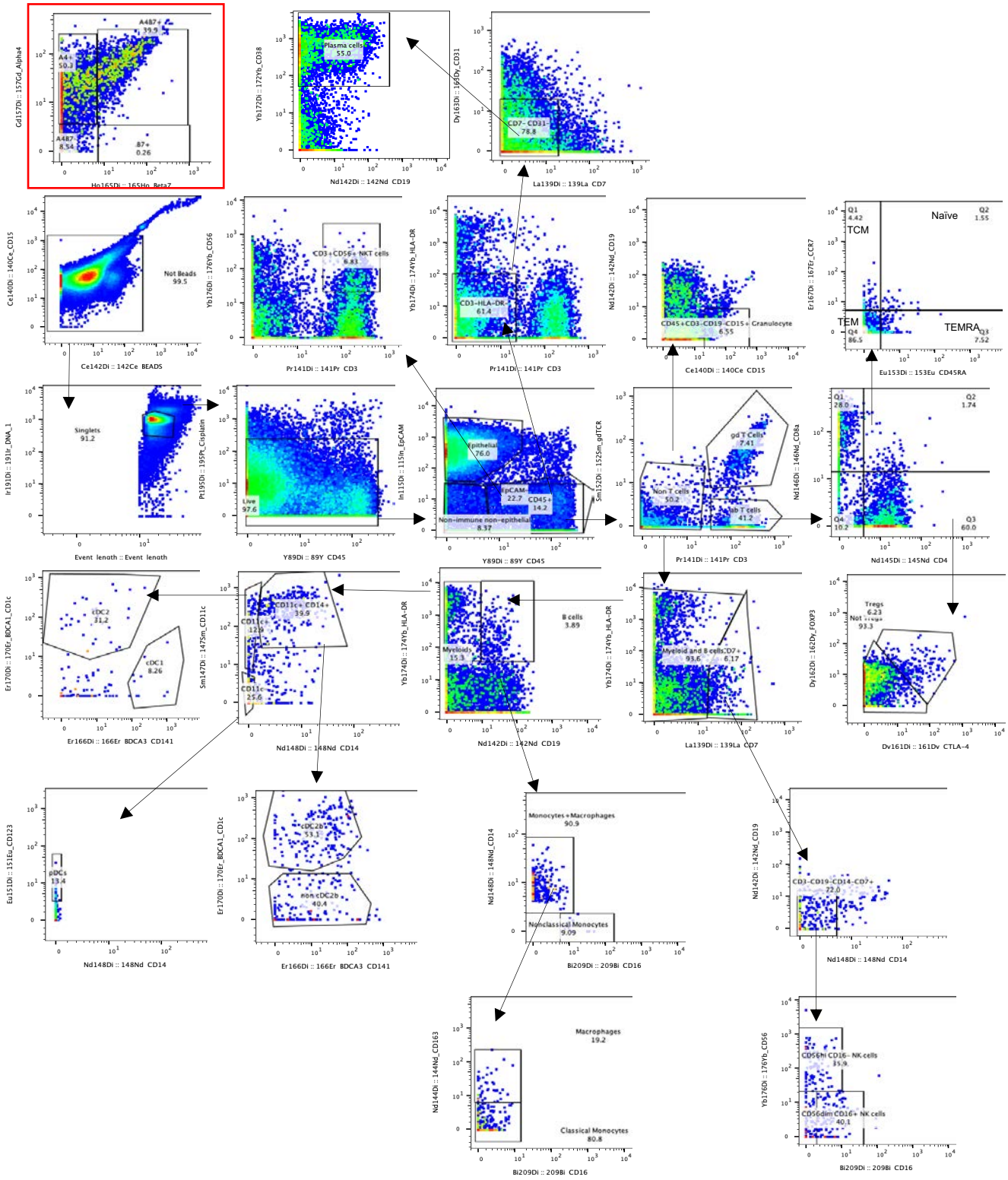

Extended Data Fig. 9| Representative supervised CyTOF gating scheme.

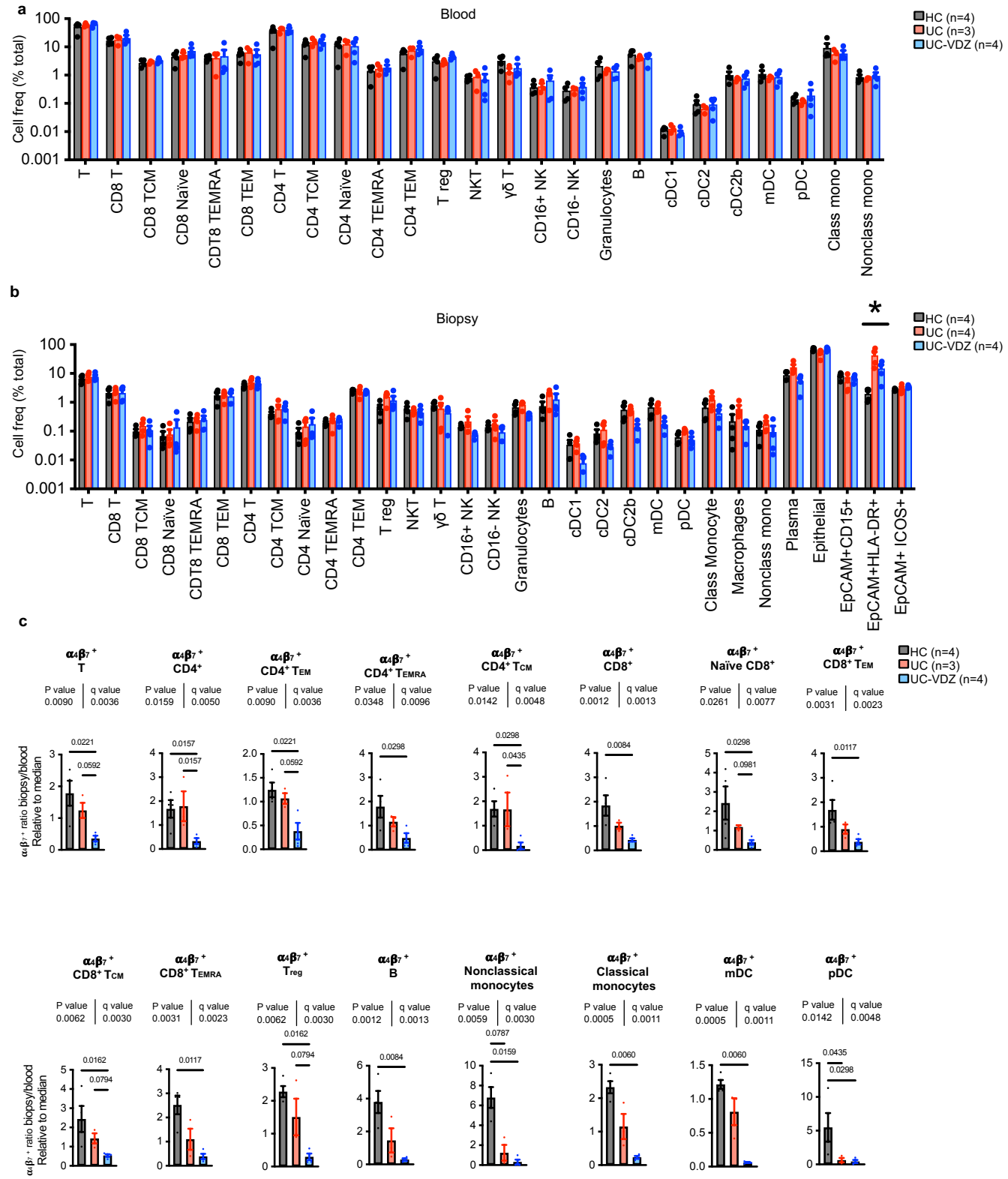

Extended Data Fig. 10| Total frequencies obtained from supervised analysis of CyTOF data from blood and biopsies and significant $\alpha_4\beta_7^+$ cell subsets. a,b, Cell frequencies for each annotated cell subset per condition in blood and biopsy, respectively. **c,** $\alpha_4\beta_7^+$ cell frequency in the biopsy versus blood for the indicated cell subsets relative to the median for each cell subset. For panels **a-c**, mean ± SEM; n=number of patients; each dot represents one patient sample; multiple one-way ANOVA Kruskal-Wallis test with FDR correction; q<0.1 threshold for discovery; *=q<0.1; only significant differences are indicated; individual subsets are shown in (**c**) with exact p-value and q-value; individual inter-column q-values are displayed only for cell subsets with overall FDR corrected q<0.01. Class monocyte-classical monocyte; Nonclass monocyte-nonclassical monocyte; mDC-cDC1,cDC2,cDC2b.

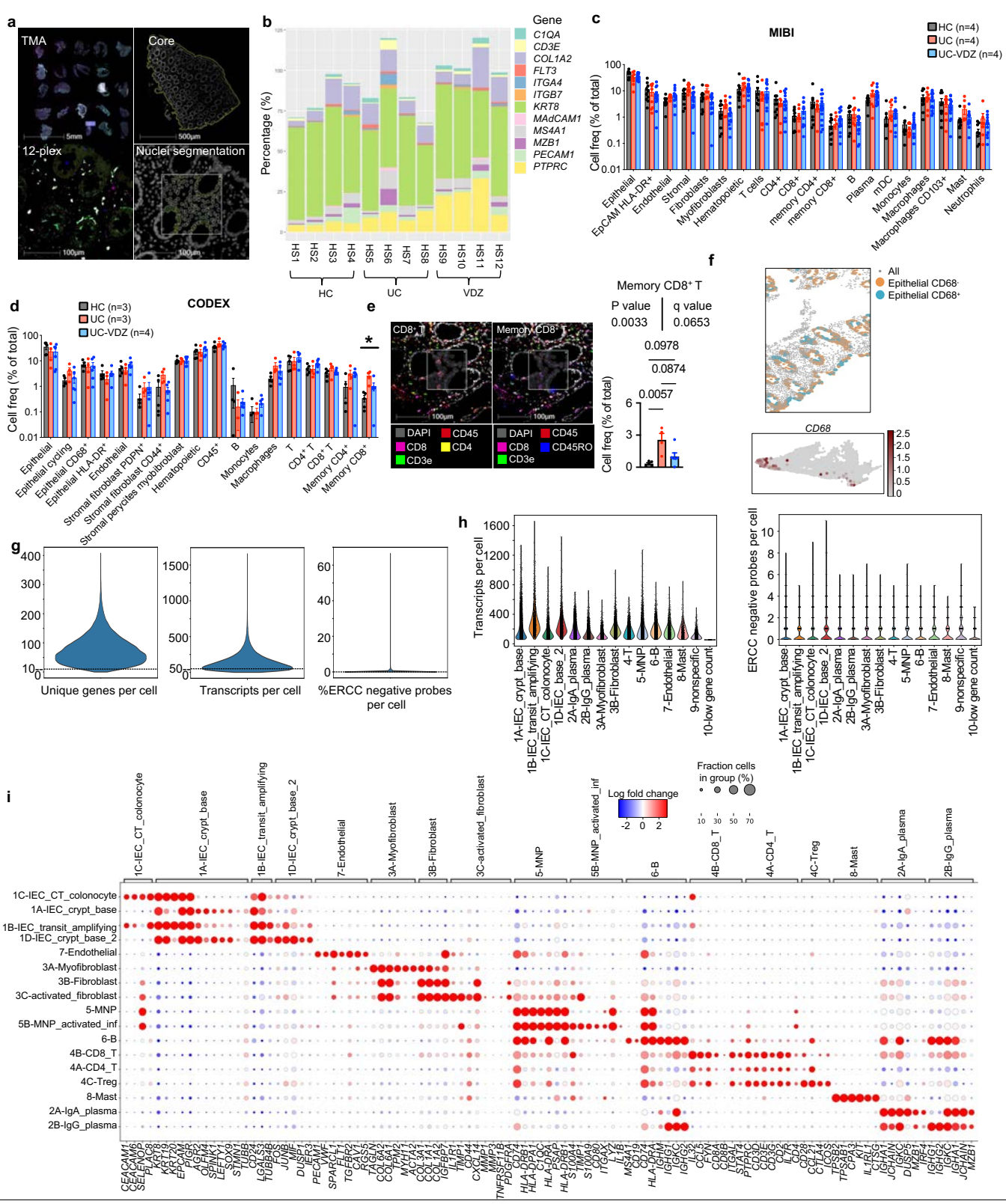

Extended Data Fig.11| Spatial transcriptomics and proteomics on FFPE tissue microarray (TMA). a, Image analysis workflow for 12-plex RNA-ISH assay using HALO, scan of the entire TMA (0.5X), representative core (4X), representative overlay of the 12 markers (20X), nuclei segmentation and localization of the 12 different markers (20X). **b,** Stacked bar plots for each patient expressing the indicated gene; values are greater than 100% due to cell co-expressing genes of interest. **c,d,** Cell frequencies as a percent of total for the indicated cell subsets identified by (**c**) MIBI and (**d**) CODEX, and **e,** representative identification of memory CD8⁺CD45RO⁺ T cells and quantitation (CODEX) from (**d**) (mean ± SEM; n=number of patients; each dot represents one FOV for MIBI or one core for CODEX; multiple one-way ANOVA Kruskal-Wallis test with FDR correction; q<0.1 threshold for discovery; *=q<0.1; only significant differences are indicated select subset is shown with exact p-value and q-value; individual inter-column q-values are displayed only for cell subsets with overall q<0.1). **f,** Representative region of interest (ROI) showing subset of CD68⁺ colonocytes by CODEX (top panel) and CITE-seq (bottom panel). **g,** Violin plots showing unique genes, transcripts, and %ERCC negative probes per cell. Cells with <10 unique genes or <50 transcripts per cell were excluded (dashed line). **h**, Transcripts and ERCC negative probes per cell, stratified by coarse annotation. **i,** Dot plot representation of curated landmark genes for annotated subsets. Genes ranked by Wilcoxon rank-sum. ERCC, External RNA Controls Consortium.

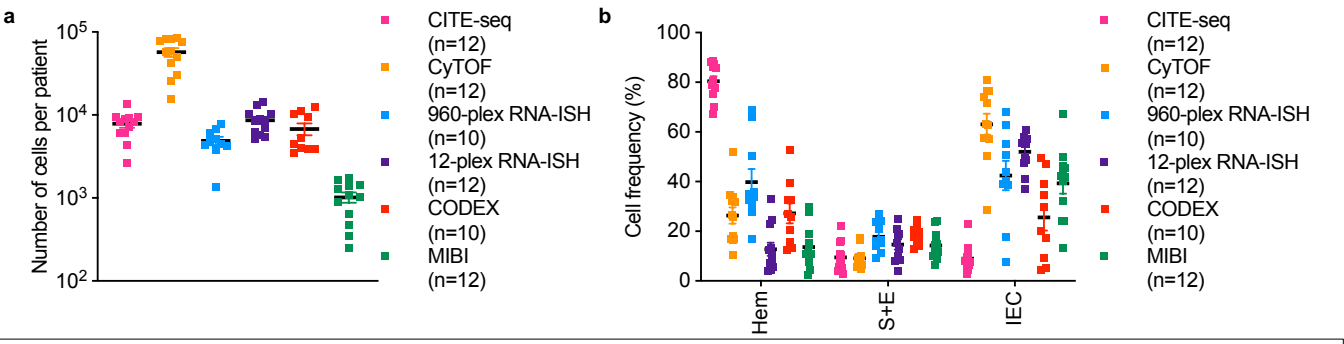

Extended Data Fig.12| Comparison of total cells analyzed per patient and cell frequency per tissue compartment among study subjects. a, Total number of cell analyzed per patient using different multi-omic methods. **b,** Cell frequency per patient expressed as percent of total for the indicated cellular compartment among different multi-omic methods. For (**a**,**b**), mean ± SEM, n=number of patients, each dot represents one patient sample. Hem-hematopoietic; S+E-Stromal + Endothelial; IEC-Intestinal epithelial cell.

Patient ID	Age	Sex	Race	Ethnicity	Disease status	UC Medication	Disease duration (y)	Duration VDZ (mo)	Prior anti-TNF exposure	Montreal classification	Mayo Endoscopic subscore
HS1	55	M	White	Non-hispanic	HC	None	n/a	n/a	No	n/a	0
HS2	49	M	White	Non-hispanic	HC	None	n/a	n/a	No	n/a	0
HS3	28	F	White	Non-hispanic	HC	None	n/a	n/a	No	n/a	0
HS4	51	F	White	Non-hispanic	HC	None	n/a	n/a	No	n/a	0
Median (IQ1-IQ3)	50 (33-54)										
HS5	25	F	White	Non-hispanic	UC	5-ASA	15	n/a	No	E2	2
HS6	40	M	White	Non-hispanic	UC	5-ASA	25	n/a	Yes	E3	2
HS7	69	F	Black	Non-hispanic	UC	5-ASA	7	n/a	No	E2	1
HS8	51	F	White	Non-hispanic	UC	5-ASA	5	n/a	No	E1	1
Median (IQ1-IQ3)	46 (29-65)					Median	11 (7-18)				
HS9	54	M	White	Non-hispanic	UC	VDZ	25	8mo	Yes	E2	1
HS10	32	M	White	Non-hispanic	UC	VDZ	8	7mo	No	E2	1
HS11	24	F	White	Non-hispanic	UC	VDZ	8	64mo	Yes	E2	3
HS12	55	M	White	Non-hispanic	UC	VDZ	10	2mo	Yes	E3	1
Median (IQ1-IQ3)	43 (26-55)						9 (8-14)				
p-value	ns	ns	ns	n/a	p=0.0025	p<0.0001	ns	n/a	ns	ns	p=0.01

Supplementary Table 1. Baseline demographic and clinical data for study participants. Categorical variables were analyzed by Chi-square test and continuous variables were compared using one-way ANOVA with FDR correction or Mann-Whitney test where appropriate. ns, not significant; n/a, not applicable.

Patient ID	Disease status	Medication	Biopsy location-severity	Mayo Endoscopic subscore	Geboes grade	Biopsy sample ID	Blood scRNA-seq	Biopsy scRNA-seq CITE-seq	Blood CyTOF	Biopsy CyTOF	12-plex RNA-ISH	CODEX	MIBI	960-plex RNA-ISH
HS1	HC	N/A	R-0	0	0.0	HS1-CLR1	Y	Y	Y	Y	Y (1-core)	N/A	N/A	Y (1-FOV)
			L-0		1.1	HS1-CLL1		Y			Y (1-core)	N/A	Y (2-FOV)	Y (2-FOV)
HS2	HC	N/A	R-0	0	1.1	HS2-CLR1	Y	Y	Y	Y	Y (1-core)	Y (1-core)	Y (3-FOV)	Y (1-FOV)
			L-0		1.1	HS2-CLL1		Y			Y (1-core)	Y (1-core)	Y (3-FOV)	Y (1-FOV)
HS3	HC	N/A	R-0	0	0.0	HS3-CLR1	Y	Y	Y	Y	N/A	Y (1-core)	N/A	Y (1-FOV)
			L-0		0.0	HS3-CLL1		Y			Y (1-core)	Y (1-core)	Y (1-FOV)	N/A
HS4	HC	N/A	R-0	0	0.0	HS4-CLR1	Y	Y	Y	Y	Y (1-core)	N/A	N/A	Y (1-FOV)
			L-0		0.0	HS4-CLL1		Y			Y (1-core)	Y (1-core)	Y (1-FOV)	Y (1-FOV)
HS5	UC	5-ASA	R-0	2	0.0	HS5-CLR1	N/A	Y	N/A	Y	Y (1-core)	Y (1-core)	Y (2-FOV)	Y (1-FOV)
			L-2		0.2	HS5-CLL1		Y			Y (1-core)	N/A	Y (1-FOV)	N/A
HS6	UC	5-ASA	R-2	2	2A.2	HS6-CLR1	Y	Y	Y	Y	Y (1-core)	N/A	Y (2-FOV)	N/A
			L-2		3.1	HS6-CLL1		Y			N/A	N/A	N/A	N/A
HS7	UC	5-ASA	R-1	1	1.1	HS7-CLR1	Y	Y	Y	Y	Y (1-core)	Y (1-core)	N/A	Y (1-FOV)
			L-0		0.0	HS7-CLL1		Y			Y (1-core)	Y (1-core)	Y (2-FOV)	Y (1-FOV)
HS8	UC	5-ASA	L-1	1	3.2	HS8-CLL1	Y	Y	Y	Y	Y (1-core)	Y (1-core)	Y (1-FOV)	Y (1-FOV)
HS9	UC	VDZ	R-0	1	0.0	HS9-CLR1	Y	Y	Y	Y	Y (1-core)	Y (1-core)	Y (3-FOV)	N/A
			L-1		0.0	HS9-CLL1		Y			Y (1-core)	Y (1-core)	Y (3-FOV)	N/A
HS10	UC	VDZ	R-0	1	1.1	HS10-CLR1	Y	Y	Y	Y	Y (1-core)	Y (1-core)	Y (1-FOV)	Y (1-FOV)
			L-1		0.1	HS10-CLL1		N/A			N/A	N/A	N/A	Y (1-FOV)
HS11	UC	VDZ	R-0	3	0.1	HS11-CLR1	Y	Y	Y	Y	N/A	N/A	N/A	Y (1-FOV)
			L-3		3.2	HS11-CLL1		Y			Y (1-core)	Y (1-core)	Y (1-FOV)	Y (1-FOV)
HS12	UC	VDZ	R-1	1	1.2	HS12-CLR1	Y	Y	Y	Y	Y (1-core)	Y (1-core)	Y (3-FOV)	N/A
			L-1		1.3	HS12-CLL1		N/A			Y (1-core)	Y (1-core)	Y (3-FOV)	Y (1-FOV)

Supplementary Table 2. Biospecimens analyzed by each multi-omics method. R, right colon; L, left colon; 5-ASA, 5-aminosalicylate; CLR1, right colon biopsy 1; CLL1, left colon biopsy; Y, yes; N/A not applicable. FOV-field of view

Assay type	Target	Ion channel / DNA barcode	Metal / DNA barcode ID	Clone/Probe	h5ad file symbol	Vendor
CITE-seq (TotalSeq)	CD103 (Integrin αE)	GACCTCATTGTGAAT	A0145	Ber-ACT8	CD103	BioLegend
	CD35	ACTTCCGTCGATCTT	A0167	E11	CD35	BioLegend
	CD25	TTTGTCCTGTACGCC	A0085	BC96	CD25	BioLegend
	CD62L	GTCCCTGCAACTTGA	A0147	DREG-56	CD62L	BioLegend
	CD3	CTCATTGTAACTCCT	A0034	UCHT1	CD3	BioLegend
	CD33	TAACTCAGGGCCTAT	A0052	P67.6	CD33.1	BioLegend
	CD4	TGTTCCCGCTCAACT	A0072	RPA-T4	CD4.2	BioLegend
	CD58 (LFA-3)	GTTCCTATGGACGAC	A0174	TS2/9	CD58.1	BioLegend
	CD8a	GCTGCGCTTTCCATT	A0080	RPA-T8	CD8a	BioLegend
	CD56	TCCTTTCCTGATAGG	A0047	5.1H11	CD56--NCAM	BioLegend
	CD11b	GACAAGTGATCTGCA	A0161	ICRF44	CD11b	BioLegend
	CD183 (CXCR3)	GCGATGGTAGATTAT	A0140	G025H7	CD183--CXCR3	BioLegend
	CD30	TCAGGGTGTGCTGTA	A0028	BY88	CD30	BioLegend
	CD336 (NKp44)	GGGCAATTAGCGAGT	A0802	P44-8	CD336--NKp44	BioLegend
	CD69	GTCTCTTGGCTTAAA	A0146	FN50	CD69.1	BioLegend
	CD335 (NKp46)	ACAATTTGAACAGCG	A0101	900	CD335--NKp46	BioLegend
	CD49f	TTCCGAGGATGATCT	A0070	GoH3	CD49f	BioLegend
	CD161	GTACGCAGTCCTTCT	A0149	HP-3G10	CD161	BioLegend
	CD45RO	CTCCGAATCATGTTG	A0087	UCHL1	CD45RO	BioLegend
	CD20	TTCTGGGTCCCTAGA	A0100	2H7	CD20	BioLegend
	KLRG1 (MAFA)	CTTATTTCCTGCCCT	A0153	SA231A2	KLRG1--MAFA	BioLegend
	CD19	CTGGGCAATTACTCG	A0050	HIB19	CD19.1	BioLegend
	CD32	GCTTCCGAATTACCG	A0142	FUN-2	CD32	BioLegend
	CD276 (B7-H3)	GACTGGGAGGGTATT	A0010	DCN.70	CD276--B7-H3	BioLegend
	CD279 (PD-1)	ACAGCGCCGTATTTA	A0088	EH12.2H7	CD279--PD-1	BioLegend
	CD197 (CCR7)	AGTTCAGTCAACCGA	A0148	G043H7	CD197--CCR7	BioLegend
	CD252 (OX40L)	TTTAGTGATCCGACT	A0021	11C3.1	N/A	BioLegend
	CD223 (LAG-3)	CATTTGTCTGCCGGT	A0152	11C3C65	CD223--LAG-3	BioLegend
	HLA-DR	AATAGCGAGCAAGTA	A0159	L243	HLA-DR	BioLegend
	CD45RA	TCAATCCTTCCGCTT	A0063	HI100	CD45RA	BioLegend
	CD196 (CCR6)	GATCCCTTTGTCACT	A0143	G034E3	CD196--CCR6	BioLegend
	CD2	TACGATTTGTCAGGG	A0367	TS1/8	CD2.1	BioLegend
	CD326 (Ep-CAM)	TTCCGAGCAAGTATC	A0123	9C4	CD326--EpCAM	BioLegend
	CD169 (Sialoadhesin, Siglec-1)	TACTCAGCGTGTTTG	A0206	7-239	CD169--Sialoadhesin--Siglec-1	BioLegend
	CD41	ACGTTGTGGCCTTGT	A0353	HIP8	CD41	BioLegend
	CD49b	GCTTTCTTCAGTATG	A0371	P1E6-C5	CD49b	BioLegend
	CD303 (BDCA-2)	GAGATGTCCGAATTT	A0370	201A	CD303--BDCA-2	BioLegend
	CD29	GTATTCCCTCAGTCA	A0369	TS2/16	CD29	BioLegend
	CD184 (CXCR4)	TCAGGTCCTTTCAAC	A0366	12G5	CD184--CXCR4	BioLegend
	CD98	GCACCAACAGCCATT	A0374	MEM-108	CD98	BioLegend
	CD124 (IL-4Rα)	CCGTCCTGATAGATG	A0363	G077F6	N/A	BioLegend
	CD135 (Flt-3/Flk-2)	CAGTAGATGGAGCAT	A0351	BV10A4H2	CD135	BioLegend
	CD370 (CLEC9A/DNGR1)	CTGCATTTCAGTAAG	A0207	8F9	CD370--CLEC9A--DNGR1	BioLegend
	CD21	AACCTAGTAGTTCGG	A0181	Bu32	CD21	BioLegend
	CD39	TTACCTGGTATCCGT	A0176	A1	CD39	BioLegend
	CD141 (Thrombomodulin)	GGATAACCGCGCTTT	A0163	M80	CD141--Thrombomodulin	BioLegend
	CD64	AAGTATGCCCTACGA	A0162	10.1	CD64	BioLegend
	CD152 (CTLA-4)	ATGGTTCACGTAATC	A0151	BNI3	CD152	BioLegend
	CD61	AGGTTGGAGTAGACT	A0372	VI-PL2	CD61	BioLegend
	CD163	GCTTCTCCTTCCTTA	A0358	GHI/61	CD163.1	BioLegend
	CD357 (GITR)	ACCTTTCGACACTCG	A0360	108-17	CD357--GITR	BioLegend
	CD137 (4-1BB)	CAGTAAGTTCGGGAC	A0355	4B4-1	CD137	BioLegend
	CD81 (TAPA-1)	GTATCCTTCCTTGGC	A0373	5A6	CD81--TAPA-1	BioLegend
	CD366 (Tim-3)	TGTCCTACCCAACTT	A0169	F38-2E2	CD366--Tim-3	BioLegend
	CD57 Recombinant	AACTCCCTATGGAGG	A0168	QA17A04	CD57	BioLegend
	CD278 (ICOS)	CGCGCACCCATTAAA	A0171	C398.4A	CD278--ICOS	BioLegend
	CD95 (Fas)	CCAGCTCATTAGAGC	A0156	DX2	CD95--Fas	BioLegend
	CD80	ACGAATCAATCTGTG	A0005	2D10	CD80.1	BioLegend
	CD138 (Syndecan-1)	ACTCTTTCGTTTACG	A0055	MI15	CD138--Syndecan-1	BioLegend
	CD70	CGCGAACATAAGAAG	A0027	113-16	CD70.1	BioLegend
	CD269 (BCMA)	CAGATGATCCACCAT	A0056	19F2	CD269--BCMA	BioLegend
	IgM	TAGCGAGCCCGTATA	A0136	MHM-88	IgM	BioLegend
	CD59	AATTAGCCGTCGAGA	A0361	p282 (H19)	CD59.1	BioLegend
	CD194 (CCR4)	AGCTTACCTGCACGA	A0071	L291H4	CD194--CCR4	BioLegend
	CD275 (B7-H2, ICOSL)	GTGCATTCAACAGTA	A0009	2D3	CD275--B7-H2--ICOSL	BioLegend
	CD314 (NKG2D)	CGTGTTTGTTCCTCA	A0165	1D11	CD314--NKG2D	BioLegend

CD86	GTCTTTGTCAGTGCA	A0006	IT2.2	CD86.1	BioLegend
Galectin-9	ACTCACTGGAGTCTC	A0016	9M1-3	N/A	BioLegend
CD195 (CCR5)	CCAAAGTAAGAGCCA	A0141	J418F1	CD195--CCR5	BioLegend
CD1c	GAGCTACTTCACTCG	A0160	L161	CD1c	BioLegend
CD28	TGAGAACGACCCTAA	A0386	CD28.2	CD28.1	BioLegend
TSLPR (TSLP-R)	CAGTCCTCTCTGTCA	A0387	1D3	TSLPR	BioLegend
CD38	TGTACCCGCTTGTGA	A0389	HIT2	CD38.1	BioLegend
CD155 (PVR)	ATCACATCGTTGCCA	A0023	SKII.4	CD155--PVR	BioLegend
CD270 (HVEM, TR2)	TGATAGAAACAGACC	A0020	122	CD270--HVEM--TR2	BioLegend
CD178 (Fas-L)	CCGGTCCTCTGTATT	A0177	NOK-1	CD178--FasL	BioLegend
CD127 (IL-7Rα)	GTGTGTTGTCCTATG	A0390	A019D5	CD127--IL-7Ra	BioLegend
CD7	TGGATTCCCGGACTT	A0066	CD7-6B7	CD7.1	BioLegend
CD117 (c-kit)	AGACTAATAGCTGAC	A0061	104D2	CD117--c-kit	BioLegend
CD10	CAGCCATTCATTAGG	A0062	HI10a	CD10	BioLegend
CD40	CTCAGATGGAGTATG	A0031	5C3	CD40.1	BioLegend
CD48	CTACGACGTAGAAGA	A0029	BJ40	CD48.1	BioLegend
CD154	GCTAGATAGATGCAA	A0032	24-31	CD154	BioLegend
CD47	GCATTCTGTCACCTA	A0026	CC2C6	CD47.1	BioLegend
CD112 (Nectin-2)	AACCTTCCGTCTAAG	A0024	TX31	CD112--Nectin-2	BioLegend
CD52	CTTTGTACGAGCAAA	A0033	HI186	CD52.1	BioLegend
CD71	CCGTGTTCCTCATTA	A0394	CY1G4	CD71	BioLegend
CD22	GGGTTGTTGTCTTTG	A0393	S-HCL-1	CD22.1	BioLegend
CD15 (SSEA-1)	TCACCAGTACCTAGT	A0392	W6D3	CD15--BEA-1	BioLegend
XCR1	AAGACGCATGTCAAC	A0208	S15046E	XCR1.1	BioLegend
CD26	GGTGGCTAGATAATG	A0396	BA5b	CD26	BioLegend
B7-H4	TGTATGTCTGCCTTG	A0395	MIH43	B7-H4	BioLegend
CD31	ACCTTTATGCCACGG	A0124	WM59	CD31	BioLegend
CD14	TCTCAGACCTCCGTA	A0081	M5E2	CD14.2	BioLegend
TIGIT (VSTM3)	TTGCTTACCGCCAGA	A0089	A15153G	TIGIT--VSTM3	BioLegend
CD294 (CRTH2)	TGTTTACGAGAGCCC	A0102	BM16	CD294--CRTH2	BioLegend
CD45	TCCCTTGCGATTTAC	A0048	2D1	CD45	BioLegend
CD34	GCAGAAATCTCCCTT	A0054	581	CD34.1	BioLegend
CD244 (2B4)	TCGCTTGGATGGTAG	A0189	C1.7	CD244--2B4	BioLegend
CD185 (CXCR5)	AATTCAACCGTCGCC	A0144	J252D4	CD185--CXCR5	BioLegend
CD18	TATTGGGACACTTCT	A0385	TS1/18	CD18	BioLegend
CD119 (IFN-? R ? chain)	TGTGTATTCCCTTGT	A0219	GIR-208	CD119--IFN-G-R-A-chain	BioLegend
CD134 (OX40)	AACCCACCGTTGTTA	A0158	Ber-ACT35 (ACT35)	CD134--OX40	BioLegend
CD24	AGATTCCTTCGTGTT	A0180	ML5	CD24.1	BioLegend
TCR γ/δ	CTTCCGATTCATTCA	A0139	B1	TCR-G--TCR-D	BioLegend
CD115 (CSF-1R)	AATCACGGTCCTTGT	A0398	9-4D2-1E4	CD115--CSF-1R	BioLegend
CD1d	TCGAGTCGCTTATCA	A0164	51.1	CD1d	BioLegend
CD192 (CCR2)	GAGTTCCCTTACCTG	A0242	K036C2	CD192--CCR2	BioLegend
CD105	ATCGTCGAGAGCTAG	A0068	43A3	CD105	BioLegend
CD144 (VE-Cadherin)	TCCACTCATTCTGTA	A0400	BV9	CD144--VE-cadherin	BioLegend
CD193 (CCR3)	ACCAATCCTTTCGTC	A0397	5E8	CD193--CCR3	BioLegend
CD55	GCTCATTACCCATTA	A0383	JS11	CD55.1	BioLegend
CD79b (Igβ)	ATTCTTCAACCGAAG	A0187	CB3-1	CD79b--Ig-B	BioLegend
CD123	CTTCACTCTGTCAGG	A0064	6H6	CD123	BioLegend
CD11c	TACGCCTATAACTTG	A0053	S-HCL-3	CD11c	BioLegend
CD54	CTGATAGACTTGAGT	A0217	HA58	CD54	BioLegend
CD268 (BAFF-R)	CGAAGTCGATCCGTA	A0215	11C1	CD268--BAFF-R	BioLegend
TIM-4	CGTCATATAGTATGG	A0428	9F4	Tim-4	BioLegend
CD1a	GATCGTGTTGTGTTA	A0402	HI149	CD1a	BioLegend
CD301 (CLEC10A)	ACCTAGAAATCAGCA	A0401	H037G3	CD301--CLEC10A	BioLegend
CD63	GAGATGTCTGCAACT	A0404	H5C6	CD63.1	BioLegend
CD44	AATCCTTCCGAATGT	A0125	BJ18	CD44.1	BioLegend
IgD	CAGTCTCCGTAGAGT	A0384	IA6-2	IgD	BioLegend
CD72	CAGTCGTGGTAGATA	A0419	3F3	CD72.1	BioLegend
CD93	GCGCTACTTCCTTGA	A0446	VIMD2	CD93.1	BioLegend
CD85g (ILT7)	TGTCAGTTCCTATGA	A0409	17G10.2	CD85g--ILT7	BioLegend
CD172a (SIRPα)	CGTGTTTAACTTGAG	A0408	15-414	CD172a--SIRPa	BioLegend
CD284 (TLR4)	GCTTAGCTGTATCCG	A0405	HTA125	CD284--TLR4	BioLegend
CD304 (Neuropilin-1)	GGACTAAGTTTCGTT	A0406	12C2	CD304--Neuropilin-1	BioLegend
CD36	TTCTTTGCCTTGCCA	A0407	5-271	CD36.1	BioLegend
CD102 (ICAM-2)	TGACCTTCCTCTCCT	A0244	CBR-IC2/2	CD102	BioLegend
TCR α/β	CGTAACGTAGAGCGA	A0224	IP26	TCR-A--TCR-B	BioLegend
CD122 (IL-2R?)	TCATTTCCTCCGATT	A0246	TU27	N/A	BioLegend
CD83	CCACTCATTTCCGGT	A0359	HB15e	CD83.1	BioLegend

CD267 (TACI)	AGTGATGGAGCGAAC	A0247	1A1	CD267--TACI	BioLegend
anti-human IgA	AAGATGTCCGAGCAA	A0186	#N/A	N/A	BioLegend
CD107a (LAMP-1)	CAGCCCACTGCAATA	A0155	H4A3	CD107a--LAMP-1	BioLegend
CD146	CCTTGGATAACATCA	A0134	P1H12	CD146	BioLegend
CD140b (PDGFR?)	CAATGGTTCACTGCC	A0129	18A2	CD140b	BioLegend
CD49a	ACTGATGGACTCAGA	A0575	TS2/7	CD49a	BioLegend
α	AACTTCTGTGGTAGC	A0584	6B11	TCR-V-A-24-J-A-18--iNKT cell	BioLegend
CD9	GAGTCACCAATCTGC	A0579	HI9a	CD9.1	BioLegend
TCR Vα7.2	TACGAGCAGTATTCA	A0581	3C10	TCR-V-A-7.2	BioLegend
TCR Vγ9	AAGTGATGGTATCTG	A0583	B3	TCR-V-G-9	BioLegend
CD49d	CCATTCAACTTCCGG	A0576	9F10	CD49d	BioLegend
C5L2	ACAATTTGTCTGCGA	A0572	1D9-M12	C5L2	BioLegend
CD338 (ABCG2)	TAAGACTTGGCCGTC	A0569	5D3	CD338--ABCG2	BioLegend
CD73 (Ecto-5'-nucleotidase)	CAGTTCCTCAGTTCG	A0577	AD2	CD73--Ecto-5-nucleotidase	BioLegend
anti-human CD79a (Ig?)	CTTATCACCCGCTTT	A0578	#N/A	N/A	BioLegend
CD158b (KIR2DL2/L3, NKAT2)	GACCCGTAGTTTGAT	A0592	DX27	CD158b--KIR2DL2--KIR2DL3--NKAT2	BioLegend
CD226 (DNAM-1)	AGACCAACTCATTCA	A0805	TX25	CD226--DNAM-1.1	BioLegend
CD186 (CXCR6)	GACAGTCGATGCAAC	A0804	K041E5	CD186--CXCR6	BioLegend
CD158f (KIR2DL5)	AAAGTGATGCCACTG	A0600	UP-R1	CD158f--KIR2DL5	BioLegend
CD158e1 (KIR3DL1, NKB1)	GGACGCTTTCCTTGA	A0599	DX9	CD158e1--KIR3DL1--NKB1	BioLegend
CD140a (PDGFR?)	ATGCGCCGAGAATTA	A0128	16A1	CD140a	BioLegend
CD354 (TREM-1)	TAGCCGTTTCCTTTG	A0586	TREM-26	N/A	BioLegend
TCR Vδ2	TCAGTCAGATGGTAT	A0582	B6	TCR-V-D-2	BioLegend
CD202b (Tie2/Tek)	CGATCCCTTACCTAT	A0588	33.1 (Ab33)	CD202b--Tie2--Tek	BioLegend
CD96 (TACTILE)	TGGCCTATAAATGGT	A0175	NK92.39	CD96--TACTILE	BioLegend
CD158 (KIR2DL1/S1/S3/S5)	TATCAACCAACGCTT	A0420	HP-MA4	CD158--KIR2DL1--KIR2DS1--KIR2DS3--KIR2DS5	BioLegend
CD337 (NKp30)	AAAGTCACTCTGCCG	A0801	P30-15	CD337--NKp30	BioLegend
CD253 (Trail)	GCCATTCCTGCCTAA	A0803	RIK-2	CD253--TRAIL	BioLegend
CD319 (CRACC)	AGTATGCCATGTCTT	A0830	162.1	CD319--CRACC	BioLegend
CD305 (LAIR1)	ATTTCCATTCCCTGT	A0590	NKTA255	CD305--LAIR1	BioLegend
CD325 (N-Cadherin)	CCTTCCCTTTCCTCT	A0433	8C11	CD325--N-Cadherin	BioLegend
mast cell tryptase	ACTGATAGACCCGCT	A0580	AA1	N/A	BioLegend
CLEC12A	CATTAGAGTCTGCCA	A0853	50C1	CD371--CLEC12A	BioLegend
CD90 (Thy1)	GCATTGTACGATTCA	A0060	5E10	CD90--Thy1	BioLegend
CD273 (B7-DC, PD-L2)	TCAACGCTTGGCTAG	A0008	24F.10C12	CD273--B7-DC--PD-L2	BioLegend
CD272 (BTLA)	GTTATTGGACTAAGG	A0170	MIH26	CD272--BTLA	BioLegend
CD5	CATTAACGGGATGCC	A0138	UCHT2	CD5.1	BioLegend
CD23	TCTGTATAACCGTCT	A0897	EBVCS-5	CD23	BioLegend
CD85j (ILT2)	CCTTGTGAGGCTATG	A0896	GHI/75	CD85j--ILT2	BioLegend
CD94	CTTTCCGGTCCTACA	A0867	DX22	CD94	BioLegend
CD27	GCACTCCTGCATGTA	A0154	O323	CD27.1	BioLegend
CD328 (Siglec-7)	CTTAGCATTTCACTG	A0902	6-434	CD328--Siglec-7	BioLegend
CD82	TCCCACTTCCGCTTT	A0920	ASL-24	N/A	BioLegend
CD16	AAGTTCACTCTTTGC	A0083	3G8	CD16	BioLegend
MERTK	TCCTGCATGTACCCA	A0423	590H11G1E3	MERTK.1	BioLegend
IgG Fc	CTGGAGCGATTAGAA	A0375	M1310G05	IgG-Fc	BioLegend
FcεRIα	CTCGTTTCCGTATCG	A0352	AER-37 (CRA-1)	FceRIa	BioLegend
CD274 (B7-H1, PD-L1)	GTTGTCCGACAATAC	A0007	29E.2A3	CD274--B7-H1--PD-L1	BioLegend
CD254 (TRANCE, RANKL)	TCCGTGTTAGTTTGT	A0356	MIH24	CD254--TRANCE--RANKL	BioLegend
CX3CR1	AGTATCGTCTCTGGG	A0179	K0124E1	CX3CR1.1	BioLegend
CD137L (4-1BB Ligand)	ATTCGCCTTACGCAA	A0022	5F4	CD137L--4-1BB-Ligand	BioLegend
Siglec-8	CTTCTCCTCAGCAAT	A0199	7C9	N/A	BioLegend
CD45	89	Y	HI30		BioLegend
EpCAM	115	In	9C4		BioLegend
CD7	139	La	M-T701		BD Bioscience
CD15	140	Ce	W6D3		BioLegend
CD3	141	Pr	UCHT1		BioLegend
CD19	142	Nd	HIB19		BioLegend
CD163	144	Nd	GHI61		BioLegend
CD4	145	Nd	RPA-T4		Thermo
CD8a	146	Nd	RPA-T8		BioLegend
CD11c	147	Sm	BU15		Thermo
CD14	148	Nd	M5E2		BioLegend
CD127	149	Sm	A019D5		BioLegend
CD123	151	Eu	6H6		Thermo
gdTCR	152	Sm	5A6.E9		ATCC

CyTOF	CD45RA	153	Eu	HI100	BioLegend
	TIM3	154	Sm	F38-2E2	BioLegend
	TIGIT	155	Gd	A15153G	BioLegend
	PD-L1	156	Gd	29E.2A3	BioLegend
	Integrin a4	157	Gd	9F10	BioLegend
	CD27	158	Gd	O323	BioLegend
	Cd137_4-1BB	159	Tb	4B4-1	Thermo
	Tbet	160	Gd	4B10	Thermo
	CTLA-4	161	Dy	14D3	Thermo
	FOXP3	162	Dy	PCH101	Thermo
	CD31	163	Dy	WM59	BioLegend
	Integrin b7	165	Ho	FIB504	BioLegend
	CD141_BDCA3	166	Er	M80	BioLegend
	CCR7	167	Er	GO43H7	BioLegend
	Ki-67	168	Er	Ki-67	BioLegend
	CD25	169	Tm	M-A251	BioLegend
	CD1c_BDCA1	170	Er	L161	BioLegend
	CD38	172	Yb	HIT2	BioLegend
	ICOS	173	Yb	C398.4A	BioLegend
	HLA-DR	174	Yb	L243	BioLegend
	PD-1	175	Lu	EH12.2H7	BioLegend
	CD56	176	Yb	NCAM16.2	BD Bioscence
	CD16	209	Bi	3G8	BioLegend
RNA-ISH	*COL1A2*	488		432721-T1	ACD bio-techne
	MS4A1	550		426771-T2	ACD bio-techne
	FLT3	650		419491-T3	ACD bio-techne
	ITGα4	488		408591-T4	ACD bio-techne
	MZB1	550		579241-T5	ACD bio-techne
	C1QA	650		485451-T6	ACD bio-techne
	ITGβ7	488		605941-T7	ACD bio-techne
	MAdCAM-1	550		404711-T8	ACD bio-techne
	KRT8	650		310261-T9	ACD bio-techne
	PECAM-1	488		487381-T10	ACD bio-techne
	CD3E	550		553971-T11	ACD bio-techne
	PTPRC	650		601991-T12	ACD bio-techne
CODEX	HLA-A	AF750	BX004	EP1395Y	Akoya Biosciences
	CD34	ATTO550	BX020	QBEND/10	Akoya Biosciences
	CD4	Cy5	BX003	EPR6855	Akoya Biosciences
	CD20	AF750	BX007	L26	Akoya Biosciences
	CD14	ATTO550	BX037	EPR3653	Akoya Biosciences
	CD68	Cy5	BX015	KP1	Akoya Biosciences
	Vimentin	AF750	BX022	091D3	Akoya Biosciences
	CD8	ATTO550	BX026	C8/144B	Akoya Biosciences
	CD11c	Cy5	BX024	118/A5	Akoya Biosciences
	CD31	AF750	BX001	EP3095	Akoya Biosciences
	E-Cadherin	ATTO550	BX014	4A2C7	Akoya Biosciences
	CD45	Cy5	BX021	D9M81	Akoya Biosciences
	SMA	AF750	BX013	1A4	Akoya Biosciences
	CD45RO	ATTO550	BX017	UCHL1	Akoya Biosciences
	CD3e	Cy5	BX045	EP449E	Akoya Biosciences
	Pan-cytokeratin	AF750	BX019	AE1/AE3	Akoya Biosciences
	CD44	ATTO550	BX005	156-3C11	Akoya Biosciences
	HLA-DR	Cy5	BX033	EPR3692	Akoya Biosciences
	Granzyme B	ATTO550	BX041	D6E9W	Akoya Biosciences
	Collagen IV	Cy5	BX042	EPR209660	Akoya Biosciences
	Podoplanin	ATTO550	BX023	NC-08	Akoya Biosciences
	FOXP3	AF647	BX031	259D/C7	Akoya Biosciences
	KI67	ATTO550	BX047	B56	Akoya Biosciences
	CD163	AF647	BX016	D6U1J	Akoya Biosciences
	CD19	ATTO550	BX028	RM332	Akoya Biosciences
	CD11b	Cy5	BX030	EP1345Y	Akoya Biosciences
	CD21	ATTO550	BX032	EP3093	Akoya Biosciences
	CD57	AF647	BX049	HNK-1	Akoya Biosciences
	dsDNA	89	Y	3519 DNA	Abcam
	E-Cadherin	113	In	36	Abcam
	Histone H3	115	In	D1H2	CST
	FoxP3-AF488	141	Pr	236A/E7	BD Pharmigen
	anti-488	141	Pr	polyclonal	Thermofisher

	CD163	142	Nd	EPR14643-36	Abcam
	CD4	143	Nd	EPR6855	Ionpath
	CD11c	144	Nd	EP1347Y	Ionpath
	CD14	145	Nd	D7A2T	CST
	CD16	146	Nd	D1N9L	CST
	LAG3	147	Sm	17B4	Ionpath
	PD-1	148	Nd	D4W2J	Ionpath
	PD-L1	149	Sm	E1L3N	Ionpath
	Granzyme B	150	Nd	D6E9W	Ionpath
	CD56	151	Eu	MRQ-42	Ionpath
	CD31	152	Sm	EP3095	Ionpath
	Ki67	153	Eu	D2H10	CST
	CD138	154	Sm	EPR6454	Abcam
	CD117	155	Gd	YR145	Ionpath
MIBI	CD68	156	Gd	D4B9C	Ionpath
	CD103	157	Gd	EPR4166(2)	Abcam
	CD8	158	Gd	C8/144B	Ionpath
	CD3	159	Tb	D7A6E	Ionpath
	Tbet	160	Gd	D6N8B	Abcam
	CD45RO	161	Dy	UCHL1	ionpath
	TIM3	162	Dy	EPR22241	Ionpath
	Vimentin	163	Dy	D21H3	Ionpath
	CD27	164	Dy	EPR8569	Abcam
	Pan-Keratin	165	Ho	AE1/AE3	Ionpath
	aSMA	166	Er	SP171	Abcam
	CD20	167	Er	L26	Abcam
	CD11b	168	Er	D6X1N	Abcam
	BDCA3 (CD141)	169	Tm	E7Y9P	CST
	CD21	170	Er	EP3093	Ionpath
	IDO1	171	Yb	EPR20374	Ionpath
	HLA-DR	172	Yb	EPR3692	Ionpath
	EpCAM	173	Yb	D9S3P	CST
	CD45	175	Yb	2B11/PD7/26	Ionpath
	HLA Class 1, ABC	176	Yb	EMR8-5	Ionpath

Supplementary Table 3. Antibodies and reagents.

Assay type	Cell subsets	Gating Strategy
CyTOF supervised	Epithelial	EpCAM^{+} CD45^{-}
	EpCAM^{+} CD15^{+}	EpCAM^{+} CD15^{+}
	EpCAM^{+} ICOS^{+}	EpCAM^{+} ICOS^{+}
	T	CD45^{+} EpCAM^{-} CD3^{+} gdTCR^{-}
	gd T	CD45^{+} EpCAM^{-} CD3^{+} gdTCR^{+}
	CD8^{+} T	CD45^{+} EpCAM^{-} CD3^{+} gdTCR^{-} CD4^{-} CD8a^{+}
	Naïve CD8^{+}	CD45^{+} CD3^{+} CD4^{-} CD8a^{+} CD45RA^{+} CCR7^{+}
	CD8$^{+}_{TCM}$	CD45^{+} CD3^{+} CD4^{-} CD8a^{+} CD45RA^{-} CCR7^{+}
	CD8$^{+}_{TEM}$	CD45^{+} CD3^{+} CD4^{-} CD8a^{+} CD45RA^{-} CCR7^{-}
	CD8$^{+}_{TEMRA}$	CD45^{+} CD3^{+} CD4^{-} CD8a^{+} CD45RA^{+} CCR7^{-}
	CD4^{+} T	CD45^{+} EpCAM^{-} CD3^{+} gdTCR^{-} CD4^{+} CD8a^{-}
	Naïve CD4^{+}	CD45^{+} CD3^{+} CD4^{+} CD8a^{-}CD45RA^{+} CCR7^{+}
	CD4$^{+}_{TCM}$	CD45^{+} CD3^{+} CD4^{+} CD8a^{-}CD45RA^{-} CCR7^{+}
	CD4$^{+}_{TEM}$	CD45^{+} CD3^{+} CD4^{+} CD8a^{-} CD45RA^{-} CCR7^{-}
	CD4$^{+}_{TEMRA}$	CD45^{+} CD3^{+} CD4^{+} CD8a^{-}CD45RA^{+} CCR7^{-}
	T_{reg}	CD45^{+} CD3^{+} CD4^{+} CD8a^{-} FOXP3^{+} CTLA-4^{+} CD127^{-}
	NKT	CD45^{+} EpCAM^{-} CD3^{+} CD16^{+} CD56^{+}
	CD16^{-} NK	CD45^{+} EpCAM^{-} CD3^{-} gdTCR^{-} HLA-DR^{+} CD19^{-} CD14^{-} CD7^{+} CD56^{hi} CD16^{-}
	CD16^{+} NK	CD45^{+} EpCAM^{-} CD3^{-} gdTCR^{-} HLA-DR^{+} CD19^{-} CD14^{-} CD7^{+} CD56^{dim} CD16^{+}
	Granulocytes	CD45^{+} CD3^{-} CD19^{-} CD15^{+}
	B	CD45^{+} EpCAM^{-} CD3^{-} gdTCR^{-} HLA-DR^{+} CD7^{-} CD19^{+}
	Plasma	CD45^{+} EpCAM^{-} CD3^{-} HLA-DR^{-} CD7^{-} CD31^{-} CD19^{-} CD38^{+}
	mDC	CD45^{+} CD3^{-} CD7^{-} HLA-DR^{+} CD19^{-} CD11c^{+}
	cDC1	CD45^{+} CD3^{-} CD7^{-} HLA-DR^{+} CD19^{-} CD14^{-} CD11c^{+} CD1c^{-} CD141^{+}
	cDC2	CD45^{+} CD3^{-} CD7^{-} HLA-DR^{+} CD19^{-} CD14^{-} CD11c^{+} CD1c^{+} CD141^{-}
	cDC2b	CD45^{+} CD3^{-} CD7^{-} HLA-DR^{+} CD19^{-} CD14^{+} CD11c^{+} CD1c^{+}
	pDC	CD45^{+} CD3^{-} CD7^{-} HLA-DR^{+} CD19^{-} CD14^{-} CD123^{+} CD11c^{-} CD1c^{+}
	Classical Monocytes	CD45^{+} CD3^{-} CD7^{-} HLA-DR^{+} CD19^{-} CD14^{+} CD16^{-} CD163^{-}
	Non-Classical Monocytes	CD45^{+} CD3^{-} CD7^{-} HLA-DR^{+}CD19^{-} CD14^{-} CD16^{+}
	Macrophages	CD45^{+} CD3^{-} CD7^{-} HLA-DR^{+}CD19^{-} CD14^{+} CD16^{-} CD163^{+}
CyTOF unsupervised blood	1_ CD4^{naïve}	CD45^{+} CD3^{+} CD4^{+} CD8a^{-} CD45RA^{+} CCR7^{+}
	2,5_ CD4^{TCM}	CD45^{+} CD3^{+} CD4^{+} CD8a^{-} CD45RA^{-} CCR7^{+}
	3,6,9,_ CD4^{TEM}	CD45^{+} CD3^{+} CD4^{+} CD8a^{-} CD45RA^{-} CCR7^{-}
	4_ CD8^{naïve}	CD45^{+} CD3^{+} CD8a^{+} CD4^{-} CD45RA^{+} CCR7^{+}
	7,10_ CD8^{TEM}	CD45^{+} CD3^{+} CD8a^{+} CD4^{-} CD45RA^{-} CCR7^{-}
	8_gd T	CD45^{+} CD3^{+} gdTCR^{+}
	11_CD8 T CD38^{+} HLA-DR^{+}	CD45^{+} CD8a^{+} HLA-DR^{+} CD38^{+}
	12_CD4 T CD38^{+} HLA-DR^{+}	CD45^{+} CD4^{+} HLA-DR^{+} CD38^{+}
	13_NK CD56^{high}	CD45^{+} CD7^{+} CD56^{hi} CD16^{hi}
	14_NK CD56^{low}	CD45^{+} CD7^{+} CD56^{low} CD16^{low}
	15_B	CD45^{+} HLA-DR^{+} CD7^{-} CD19^{+}
	16_Granulocyte	CD45^{+} CD16^{+} CD15^{+}
	17_mDC	CD45^{+} CD7^{-} HLA-DR^{+} CD14^{low} CD123^{-} CD11c^{+}
	18,20,21_Classical Monocytes	CD45^{+} CD7^{-} HLA-DR^{+} CD14^{+} CD16^{-} CD163^{-}
	19_Non classical Monocytes	CD45^{+} CD7^{-} HLA-DR^{+} CD14^{-} CD16^{+}
CyTOF unsupervised biopsy	1,4_Epithelial	EpCAM^{+}
	2,3_EpCAM^{+} CD15^{high}	EpCAM^{+} CD15^{hi}
	5,6,8_EpCAM^{+} ICOS^{high}	EpCAM^{+} ICOS^{hi}
	9,12_EpCAM^{+} HLA-DR^{+}	EpCAM^{+} HLA-DR^{+}
	11,17_Stromal S1	CD45^{-} CD31^{-} EpCAM^{-} CD56^{+}
	13_Stromal	CD45^{-} CD31^{-} EpCAM^{-}
	14_B	CD45^{+} HLA-DR^{+} CD19^{+}
	15_Endothelial	CD45^{-} HLA-DR^{+} EpCAM^{-} CD31^{+}
	16_CD4 T	CD45^{+} CD3^{+} CD4^{+} CD8a^{-}
	18_MNP-mDC and Macrophages	CD45^{+} CD7^{-} HLA-DR^{+} CD14^{low} CD16^{-} CD11c^{+} CD19^{-} CD163^{+}
	19_CD8 T	CD45^{+} CD3^{+} CD8a^{+} CD4^{-}
	20,21_Plasma	CD45^{+} EpCAM^{-} CD3^{-} HLA-DR^{-} CD7^{-} CD19^{-} CD38^{+}
	Epithelial	E-cadherin^{+} CD45^{-} CD31^{-}
	Epithelial CD68+	E-cadherin^{+} CD68^{+} CD3^{-} CD163^{-}

CODEX supervised	Epithelial HLA-DR+	E-cadherin^{+} HLA-DR^{+} CD3^{-} CD163^{-}
	Epithelial cycling	E-cadherin^{+} Ki67^{+}
	Endothelial	CD31^{+} E-cadherin^{-} CD45^{-}
	Stromal fibroblast CD44^{+}	Vimentin^{+} CD44^{+} CD45^{-} CD31^{-} CD20^{-} CD14^{-} CD3^{-} E-cadherin^{-} PDPN^{-}
	Stromal pericytes myofibroblats	Vimentin^{+} SMA^{+} Collagen IV^{+}
	Stromal fibroblast PDPN^{+}	Vimentin^{+} PDPN^{+} CD45^{-} CD31^{-} CD20^{-} CD14^{-} CD3^{-} E-cadherin^{-} CD44^{-}
	Hematopoietic	CD45^{+} E-cadherin^{-} CD31^{-}
	CD45^{+}	CD45+
	Monocyte	CD45^{+} HLA-DR^{+} CD3^{-} CD163^{-} CD20^{-} CD14^{+} CD68^{+}
	Macrophages	CD45^{+} HLA-DR^{+} CD3^{-} CD163^{+}
	B	CD45^{+} HLA-DR^{+} CD20^{+} CD3^{-} E-cadherin^{-} CD163^{-}
	T	CD45^{+} CD3^{+} E-cadherin^{-}
	CD4^{+} T	CD45^{+} CD3^{+} CD4^{+} CD8^{-}
	CD8^{+} T	CD45^{+} CD3^{+} CD4^{-} CD8^{+}
	Memory CD4^{+} T	CD45^{+} CD8^{-} CD3^{+} CD4^{+} CD45RO^{+}
	Memory CD8^{+} T	CD45^{+} CD4^{-} CD3^{+} CD8^{+} CD45RO^{+}
CODEX unsupervised	1_B	CD45^{+} HLA-DR^{+} CD19^{+} CD20^{+}
	2_Endothelial	E-cadherin- CD45^{-} CD31+
	3_Epithelial	E-cadherin^{+} PCK^{+} CD45^{-} CD31^{-}
	4_Epithelial CD68^{+}	E-cadherin^{+} PCK^{+} CD68^{+}
	5_Epithelial cycling	E-cadherin+ PCK+ Ki67+
	6_Macrophages	CD45^{+} HLA-DR^{+} CD163^{+}
	7_Memory T	CD45^{+} CD3^{+} CD45RO^{+}
	8_Stromal fibroblast CD44^{+}	Vimentin^{+} CD44^{+} CD45^{-} CD3^{-} E-cadherin^{-}
	9_Stromal pericytes myofibroblast	Vimentin^{+} SMA^{+} Collagen IV^{+}
	10_Stromal fibroblast PDPN^{+}	Vimentin^{+} PDPN^{+} CD45^{-} CD3^{-} E-cadherin^{-}
	11_T CD45RO^{-}	CD45^{+} CD3^{+} CD45RO^{-}
MIBI supervised	Hematopoietic	CD45^{+} EpCAM^{-} CD31^{-}
	Epithelial	EpCAM^{+} CD45^{-} CD31^{-}
	Epithelial HLA-DR+	EpCAM^{+} HLA-DR^{+}
	Endothelial	CD31^{+} EpCAM^{-} CD45^{-}
	Stromal	Vimentin^{+} EpCAM^{-} CD45^{-} CD31^{-}
	T	CD45^{+} CD3^{+}
	CD4^{+} T	CD45^{+} CD3^{+} CD4^{+} CD8a^{-}
	CD8^{+} T	CD45^{+} CD3^{+} CD4^{-} CD8a^{+}
	Memory CD4^{+} T	CD45^{+} CD8^{-} CD3^{+} CD4^{+} CD45RO^{+}
	Memory CD8^{+} T	CD45^{+} CD4^{-} CD3^{+} CD8^{+} CD45RO^{+}
	Neutrophils	CD45^{+} EpCAM^{-} CD3^{-} CD20^{-} CD16^{+} CD56^{-} HLA-DR^{-}
	B	CD45^{+} CD3^{-} HLA-DR^{+} CD20^{+}
	Plasma	CD45^{+} CD3^{-} CD20^{-} CD138^{+}
	mDC	EpCAM^{-} CD45^{+} CD3^{-} CD20^{-} CD11c^{+}
	Mast	EpCAM^{-} CD45^{+} CD3^{-} CD20^{-} CD117^{+}
	Monocytes	HLA-DR^{+} CD163^{-} CD3^{-} CD20^{-} CD14^{+} CD68^{+}
	Macrophages	CD163^{+} CD68^{+} CD3^{-}
	Macrophages CD103^{+}	CD163^{+} CD3^{-} CD68^{+} CD103^{+}
	Fibroblasts	CD45^{-} EpCAM^{-} CD31^{-} Vimentin^{+} CD56^{-}
	Myofibroblasts	CD45^{-} EpCAM^{-} CD31^{-} Vimentin^{+} SMA^{+} CD56^{-}

Supplementary Table 4. Cell subset phenotypes for supervised and unsupervised analyses for each multi-omics method.

Cell type	Gene list	Numeric ID
MNP-pDC	*HLA-DRA*	8118548
	CD74	8115147
	HLA-DRB1	8125445
	CST3	8065403
	LYZ	7957023
	HLA-DPA1	8125556
	GZMB	7978366
	ITM2C	8048995
	SEC61B	8156838
	IRF1	8114010
	LILRA4	8039246
	APP	8069644
	C12orf75	7958253
	PPP1R14B	7949060
	JCHAIN	8100827
	TCF4	8023415
	UGCG	8157216
	ALOX5AP	7968344
	SERPINF1	8003667
	CCDC50	8084818
MNP-Monocytes	*HLA-DRA*	8118548
	CD74	8115147
	HLA-DRB1	8125445
	CST3	8065403
	LYZ	7957023
	HLA-DPA1	8125556
	S100A9	7905571
	S100A8	7920244
	TIMP1	8167185
	FCN1	8165011
	SERPINA1	7981068
	S100A4	7920271
	LILRA5	8039236
	S100A6	7920258
	TYMP	8077103
	VCAN	8106743
	SOD2	8130556
	CD44	7939341
	CD14	8114612
	EREG	8095728
	TSPO	8073612
MNP-Macrophage	*HLA-DRA*	8118548
	CD74	8115147
	HLA-DRB1	8125445
	CST3	8065403
	LYZ	7957023
	HLA-DPA1	8125556
	C1QA	7898793
	FTL	8030171
	C1QC	7898799
	C1QB	7898805
	ITM2B	7969003
	NPC2	7980146
	SLC40A1	8057677
	CCL3	8014369
	MS4A7	7940259
	CTSS	7919800
	FCGRT	8030374
	CCL4	8006602
MNP-mDC	*HLA-DRA*	8118548
	CD74	8115147
	HLA-DRB1	8125445
	CST3	8065403
	LYZ	7957023
	HLA-DPA1	8125556
	BASP1	8104601
	SLC38A1	7962516
	LTB	8124950
	CST7	8061416
	CD1C	7906348
	ACAP1	8004331
	DAPP1	8096602
	STK17A	8132503
	ADAM8	7937150
	FCER1A	7906443
	RHOF	7967202
	FSCN1	8131339
	ICAM3	8033987
	CD86	7896700
	CXCR4	8055465

Stromal-Activated Fibroblast	*COL6A2*	8069301
	CXCL14	8114249
	CALD1	8136347
	COL3A1	8046922
	IGFBP7	8100541
	C11orf96	7939492
	TIMP1	8167185
	MMP3	7951284
	MMP1	7951271
	AREG	8095736
	TMEM158	8086530
	TNFRSF11B	8152512
	ACSL4	8174474
	PLAU	7928429
	HGF	8140556
	STC1	8149825
	GJA1	8121749
	CD82	7939546
	ISG20	7985777
	NRG1	8145766
Stromal S2	*COL6A2*	8069301
	CXCL14	8114249
	CALD1	8136347
	COL3A1	8046922
	IGFBP7	8100541
	C11orf96	7939492
	F3	7917875
	POSTN	7971077
	ENHO	8160816
	PDGFRA	8095080
	SOX6	7946757
	PLAT	8150509
	NSG1	8093839
	HSD17B2	7997491
	DDHD1	7979223
	PDGFD	7951351
	AGT	7924987
	WNT5B	7953012
Endothelial	*IGFBP7*	8100541
	PLVAP	8035297
	SPARCL1	8101659
	IFITM3	7945371
	IGFBP4	8007100
	CAV1	8135594
	CCL21	8160889
	TFF3	8070567
	TFP1	8057599
	NUPR1	8000574
	MMRN1	8096415
	PROX1	7909681
	LYVE1	7946579
	AKAP12	8122807
	TBX1	8071276
	FABP4	8151532
	PPFIBP1	7954559
	RBP1	8091078
	EFEMP1	8052355
	NR2F1	8106923
	ACKR1	7906435
	NPC2	7980146
	CPE	8098204
	CLU	8149927
	MADCAM1	8023941
	DUSP23	7906469
	IL1R1	8043995
	ZNF385D	8085774
	KCTD12	7972055
	IL33	8154295
	ADGRG6	8122365
	LPCAT4	7987230
	SELP	7922200
	CTNNAL1	8163063
	TLL1	8098214
	GSN	8157582
	SLC9A3R2	7992463
	NOTCH4	8125383
	RGCC	7968789
	A2M	7960947
	MGLL	8090433
	VAMP5	8043203
	FLT1	7970763

	TSC22D1	7971350
	RBP7	7897522
	ADGRF5	8126798
	ADGRL4	7917182
	SRGN	7927964
CD4 T	*IL7R*	8104901
	CD3E	7944179
	ARL4C	8059854
	KLRB1	7961059
	SPOCK2	7934215
	KLF2	8026564
	SELL	7896687
	LEF1	8102232
	CCR7	8015031
	C1orf162	7903980
	LYPD3	8037301
	ACTN1	7979824
	TRABD2A	8053379
	GCNT4	8112668
	SLC40A1	8057677
	FHIT	8088458
	FAM117B	8047565
	S100A4	7920271
	JUN	7916609
	CCL5	8014316
	TNFAIP3	8122265
	ANXA1	8155849
	ANKRD28	8085628
	ID2	8040103
	EGR1	8108370
	GPR65	7976080
	LGALS3	7974461
	HOPX	8100507
T reg	*IL7R*	8104901
	CD3E	7944179
	ARL4C	8059854
	KLRB1	7961059
	SPOCK2	7934215
	CTLA4	8047692
	TIGIT	8081799
	MAF	8002969
	ARID5B	7927732
	BATF	7975793
	TBC1D4	7972021
	PHACTR2	8122426
	RNF19A	8152041
	TNFRSF4	7911413
	UCP2	7950307
	ICA1	8138202
	TNFRSF1B	7896721
	TNFRSF18	7911403
	DUSP4	8150076
	TOX2	8062782
Cytotoxic lymphocyte	*CCL5*	8014316
	NKG7	8038809
	GZMA	8105340
	IL32	7992828
	CCL4	8006602
	CD7	8019478
	GZMK	8105331
	ITGB2	8070826
	GZMH	7978360
	KLF2	8026564
	KLRG1	7953835
	KLRB1	7961059
	SPRY1	8097282
	CMC1	8078312
	SH2D1A	8169792
	HCST	8028104
	SH3BGRL3	7899153
	KLRD1	7953949
	CD3E	7944179
	CD3D	7952056
	CD69	7896693
	CD3G	7944185
	CD8A	8053584
	CD74	8115147
	HLA-DRA	8118548
	MS4A1	7940287
	HLA-DRB1	8125445
	HLA-DPA1	8125556

B	*CD79A*	8029136
	IGHM	7896697
	TCL1A	7981183
	FCER2	8033420
	YBX3	7961230
	KLF4	8163002
	KLF6	7931810
	GPR183	7972557
	TNFSF9	8025053
	CD27	7953333
	LDLRAD4	8020308
	ACTG1	8019183
	GAPDH	7953385
	BASP1	8104601
	PFN1	8011759
	HMGN1	8070389
	YBX1	7900585
	LCP1	7971461
	SLC25A5	8169640
	ARPC1B	8134552
	ANP32B	8156750
	ACTR3	8044686
	MARCKSL1	7914525
Plasma	*JCHAIN*	8100827
	MZB1	8114511
	SSR4	8170775
	CD79A	8029136
	IGHM	7896697
	CD44	7939341
	CD9	7953291
	CD48	7921667
	THY1	7952268
	LAG3	7953418
Epithelial	*LGALS4*	8036591
	PIGR	7923929
	KRT8	7963567
	C15orf48	7983478
	SH2D6	8043157
	TRPM5	7945742
	TLE4	8156060
	FABP1	8053654
	AQP8	7994252
	SLC26A3	8142171
	GUCA2A	7915404
	CEACAM7	8037053
	SLC26A2	8109194
	OTOP2	8009705
	BEST4	7915598
	CA4	8008900
	OLFM4	7969288
	LEFTY1	7924663
	PTGDR	7974363
	UBE2C	8063043
	HMGN2	7899187
	TOP2A	8014974
	HMGB2	8103728
	TUBA1B	7963046
Neutrophil	*S100A8*	7920244
	S100A9	7905571
	FCGR3A	7921868
	FCGR3B	7921873
	IL1R2	8043981
	GCA	8046003
	CSF3R	7914950
	S100P	8093950
	BASP1	8104601
	FPR1	8038899
	IFITM2	7937330
	ELANE	8024956

Supplementary Table 5. Cell subset-specific gene signatures used for Gene Set Enrichment Analysis (GSEA). Numeric ID, Affymetrix numeric probe identifier corresponding to each gene.

Assay type	Patient ID	Specimen/imaged	Number of cells	% of hematopoietic	% of Stromal and Endothelial	% IEC	Multi-omic method
CITE-seq	HS1	Blood	899				single cell transcriptomic and proteomic
	HS2	Blood	3120				
	HS3	Blood	1699				
	HS4	Blood	1761				
	HS5	N/A	N/A				
	HS6	Blood	3474				
	HS7	Blood	2356				
	HS8	Blood	1111				
	HS9	Blood	1473				
	HS10	Blood	1669				
	HS11	Blood	1003				
	HS12	Blood	1565				
	HS1	Biopsy	9572	87.4	3.9	7.7	
	HS2	Biopsy	2648	85.7	5.4	8.3	
	HS3	Biopsy	8256	88.6	7.4	2.8	
	HS4	Biopsy	13662	77.8	10.5	10.7	
	HS5	Biopsy	6103	75.2	15.9	7.8	
	HS6	Biopsy	9036	70.2	22.2	6.3	
	HS7	Biopsy	9548	88.2	3.0	7.9	
	HS8	Biopsy	6076	79.1	15.8	4.3	
	HS9	Biopsy	4393	67.4	8.7	23.0	
	HS10	Biopsy	9192	80.6	5.7	13.3	
	HS11	Biopsy	7072	86.1	5.2	6.1	
	HS12	Biopsy	8342	78.9	10.8	9.6	
CyTOF	HS1	Blood	57374				single cell proteomic
	HS2	Blood	136673				
	HS3	Blood	167045				
	HS4	Blood	151381				
	HS5	N/A	N/A				
	HS6	Blood	75079				
	HS7	Blood	162640				
	HS8	Blood	121482				
	HS9	Blood	139270				
	HS10	Blood	85768				
	HS11	Blood	176299				
	HS12	Blood	117145				
	HS1	Biopsy	82382	16.6	6.1	76.4	
	HS2	Biopsy	83878	17.1	4.7	76.7	
	HS3	Biopsy	82480	32.0	8.9	57.7	
	HS4	Biopsy	57637	25.7	9.7	63.2	
	HS5	Biopsy	50659	26.7	9.4	62.9	
	HS6	Biopsy	30428	52.1	17.3	28.7	
	HS7	Biopsy	59387	34.6	5.6	57.2	
	HS8	Biopsy	41843	31.9	16.4	50.3	
	HS9	Biopsy	78302	18.0	7.0	74.1	
	HS10	Biopsy	25923	10.6	6.6	80.9	
	HS11	Biopsy	75650	33.8	7.4	57.7	
	HS12	Biopsy	15680	16.8	10.0	71.8	
Multiplexed RNA-ISH	HS1	Core	8816	4.2	3.8	57.0	FFPE spatial transcriptomic
	HS2	Core	10198	4.3	8.1	58.2	
	HS3	Core	6314	6.5	19.0	61.0	
	HS4	Core	5091	5.5	24.9	47.5	
	HS5	Core	8490	8.8	15.4	49.4	
	HS6	Core	8868	12.4	18.0	48.9	
	HS7	Core	5779	7.2	10.3	55.4	
	HS8	Core	5365	13.1	13.0	37.1	
	HS9	Core	10212	22.9	8.7	57.9	
	HS10	Core	6975	24.5	8.4	55.3	
	HS11	Core	13223	33.2	25.1	41.0	
	HS12	Core	14161	10.6	20.8	55.0	
CosMx	HS1	FOV	5131	30.6	14.3	55.2	FFPE spatial transcriptomic
	HS2	FOV	6021	27.7	9.4	62.9	
	HS3	FOV	1353	50.2	11.2	38.6	
	HS4	FOV	4262	16.9	15.1	68.0	
	HS5	FOV	3774	32.8	16.4	50.8	
	HS6	FOV	N/A				
	HS7	FOV	4451	35.1	20.8	44.1	
	HS8	FOV	4888	68.7	23.6	7.7	
	HS9	FOV	N/A				
	HS10	FOV	7765	35.7	24.0	40.3	
	HS11	FOV	6819	66.2	16.1	17.8	
	HS12	FOV	4319	33.9	27.0	39.1	
CODEX	HS1	Core	N/A				FFPE spatial proteomic
	HS2	Core	10302	12.6	15.5	49.6	
	HS3	Core	3987	32.5	17.4	29.6	
	HS4	Core	3868	25.9	17.6	17.4	
	HS5	Core	3451	20.5	13.0	47.0	
	HS6	Core	N/A				
	HS7	Core	4487	13.2	19.8	20.1	
	HS8	Core	5214	39.5	20.7	5.2	
	HS9	Core	3937	15.6	14.3	38.9	
	HS10	Core	11201	26.8	24.6	34.7	
	HS11	Core	12286	52.9	16.4	4.5	
	HS12	Core	9351	32.5	21.7	9.2	
MIBI	HS1	FOV	893	10.7	23.6	41.9	FFPE spatial proteomic
	HS2	FOV	1455	14.4	10.3	45.4	
	HS3	FOV	1295	7.6	6.4	50.1	
	HS4	FOV	250	2.4	8.8	67.2	
	HS5	FOV	636	10.2	18.4	43.4	
	HS6	FOV	1630	29.9	16.0	13.4	
	HS7	FOV	349	11.0	24.2	42.5	
	HS8	FOV	473	18.8	14.8	23.9	
	HS9	FOV	1090	11.4	12.1	40.2	
	HS10	FOV	1041	4.3	10.2	46.5	
	HS11	FOV	1732	27.7	11.8	24.2	
	HS12	FOV	1401	15.3	14.6	32.4	

Supplementary Table 6. Cell counts and percentages of hematopoietic, stromal and endothelial, and intestinal epithelial cell (IEC) subsets for each patient biospecimen and multi-omic method.